Chapter 3

New oxidovanadium(IV/V) complexes with tridentate Schiff base ligands: Synthesis, molecular structure and *in vitro* antidiabetic activity

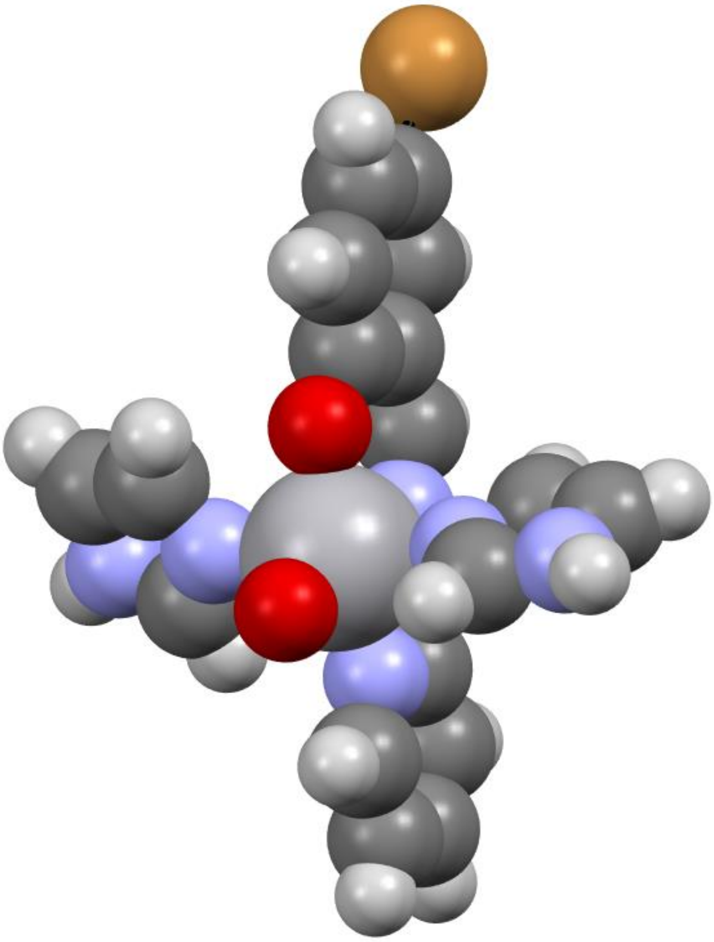

1 Introduction

Vanadium is a biologically relevant transition metal and found at the active centre of some enzymes e.g., nitrogenases and halo peroxidises [1]. The coordination chemistry of vanadium has attracted too much focus in the last few years [2-5]. The proposed therapeutic applications of vanadium compounds, particularly in the treatment of diabetes, have shown to maintain insulin-mimetic and enhancing effect both *in vivo* and *in vitro* [6, 7].

A vital interest lies inthe medicinal aspects of vanadium complexes [8, 9]. This has been prompted enormously by the observation of insulin mimicking effects of vanadium(IV/V) complexes [10, 11]. The glucose-lowering effect of vanadium complexes has been the subject of medicinal research and a large number of vanadium complexes have been tested as a suitor as antidiabetic treatments [12]. The antidiabetic properties of these complexes make them promising agents as inhibitors of insulin [13]. Insulin is a gesticulate hormone that is essential for the metabolism of carbohydrates and fats. It is secreted by the pancreas to kick back the elevated level of glucose in the bloodstream. The enhanced insulin level then encourages glucose uptake by the liver, gut and peripheral tissues, which harvests energy production and storage in the organism [14].

It is proved that vanadium complexes are less toxic and more potent than vanadium salt in lowering the glucose level [9]. Such insulin-mimetic properties of vanadium complexes make them promising antidiabetic candidate [10]. Vanadium compounds also produce resistance oxygen species (ROS) and hence causing oxidative stress with issues recently not much evaluated. So far the most effective antidiabetic drug is the bismaltatooxidovanadium(IV) complexes [11]. This finding limelight the importance of oxygen donor ligands.

Schiff base ligands as privileged ligands have fascinated much attention due to their effortless synthesis and their transition metal complexes are studied due to their functional applications in various fields [1-7]. Besides, vanadium complexes with Schiff bases have received much attention due to their broad range of significance and application of vanadium in biological as well as industrial processes [14-18].

The synthesis of oxidovanadium complexes using manipulated tridentates and tetradentates Schiff base is a topic of recent interest [19-33]. Therefore, in continuation of our work [34-36] synthesis, characterization and biological application of complexes and to explore the new mimics that enhanced the properties of insulin. We report here new oxidovanadium complexes with azo functionalized Schiff base ligands and to explore their mimetic properties.

This part describes the synthesis and structural characterization of vanadium(IV/V) complexes using the Schiff bases and imidazole as co-ligand viz., $[VO(L^1)(H_2O)]NO_3$ **1**, $[VO(L^2)(H_2O)]NO_3$ **2**, $[VO(L^2)(ImH)_2]SO_4.H_2O$ **3,** $[VO(L^1)ImH]NO_3$ **4,** $[VO_2(L^3)]$ **5,** $[VO_2(L^4)]$ **6** and $[VO_2(L^1)]ImH$ **7** (where, ImH = Imidazole, HL^1 = (Z)-N'-(2-hydroxy-3-methoxybenzylidene)acetohydrazide, HL^2 = (E)-4-bromo-2-((2-(pyridin-2-yl)hydrazono)methyl)phenol, HL^3 = (E)-2-((2-(pyridin-2-yl)hydrazono)methyl)phenol and HL^4 = (Z)-N'-((2-hydroxynaphthalen-1-yl)methylene)acetohydrazide).

2 Experimental

2.1 Material

Vanadyl sulphate monohydrate was purchased from Across Organics and rat intestinal acetone powder from Sigma-Aldrich. All other chemicals and solvents were reagent grade.

2.2 Physical Measurements

Microanalyses were carried out using a Euro Vector EA3000 elemental analysis. FTIR spectra were recorded as KBr pellets on a Bruker alpha FTIR-Spectrophotometer. ^{1}H and ^{13}C NMR spectra of ligands were recorded on a Bruker Advance III 400MHz spectrometer. UV-visible spectra analysis was performed on a Perkin Elmer Lambda 35 Spectrophotometer. Cyclic voltammetry (CV) experiments were carried out on a BAS-100 electrochemical analyser. A three-electrode setup consisting of a glassy carbon working electrode, a platinum auxiliary electrode and Ag/AgCl saturated KCl electrode. Tetra butyl ammonium perchlorate (TBAP) was used as supporting electrolyte. All measurements were done at ambient temperature under a nitrogen atmosphere. X-ray diffraction data of complexes were collected at room temperature on X'calibur CCD area-detector diffractometer equipped with graphite monochromatic MoKα radiation ($\lambda = 0.71073$ Ǻ). The crystal used for data collection was of suitable dimensions. The unit cell parameters were determined by least-square refinements of all reflections in both cases. All the structures were solved by direct method and refined by full-matrix least-squares on F2. Data were corrected for Lorentz, polarization and multi-scan absorption correction [37]. The structures were solved by direct methods using SHELXS97 [38]. All non-hydrogen atoms of the molecule were located in the best E-map. Full-matrix least-squares refinement was carried out using SHELXL97 [38]. The geometry of the molecule has been calculated using the software PLATON [39] and PARST [40].Electron paramagnetic resonance (EPR) spectra were measured using a Varian E-line Century Series EPR spectrometer equipped with a dual cavity and operating at the X-band of the 100 kHz modulation frequency. Tetracyanoethylene (TCNE) was used as a field marker (g = 2.00277). Room temperature magnetic susceptibilities were collected with a Gouybalance method. Molar conductivities of the freshly prepared 1.0×10^{-3} M DMSO solutions were measured on a Systronics Conductivity 308 TDS meter.

2.3 Synthesis

2.3.1 Synthesis of ligand HL^1

The Schiff base (HL^1) was synthesised following the method described in the literature [41]. To a solution of acetyl hydrazide (0.7g, 10 mmol) in ethanol (20 mL) was added with stirring to a solution of vanillin (1.521 g, 10 mmol) in ethanol (50 mL) and heated under reflux for 2 hrs at 80 °C (Scheme 1). The solvent was removed under reduced pressure and a light-yellow solid resulted. Finally obtained Schiff base was washed with ethanol and recrystallized from ethanol.

M.P.: 175 °C. Yield: 87%. Anal. Calc. for $C_{10}H_{12}N_2O_3$ (208.23 g mol^{-1}): Calc. C, 57.68; H, 5.81; N, 13.45%. Found: C, 57.71; H, 5.83; N, 13.42%. FTIR bands (KBr, cm^{-1}): ν(C=N) 1679 m, ν(-OH) 3433 b, ν(N-H) 3015 m. ^{1}H NMR ($CDCl_3$, 400 MHz) δ: 10.4 (s, 1H, Ar-OH), 10.2 (s, 1H, –NH), 8.01 (s, 1H, –CH=N), 6.8-7.2 (m, 3H, Ar-H), 3.9 (s, 3H, $-OCH_3$), 2.3 (s, 3H $-COCH_3$) ppm. ^{13}C NMR (DMSO-d_6, 400 MHz) δ: 165 (C=O), 147 (CH=N), 113-148 (Ar-C), 56 ($-OCH_3$), 21.8 ($-COCH_3$) ppm.

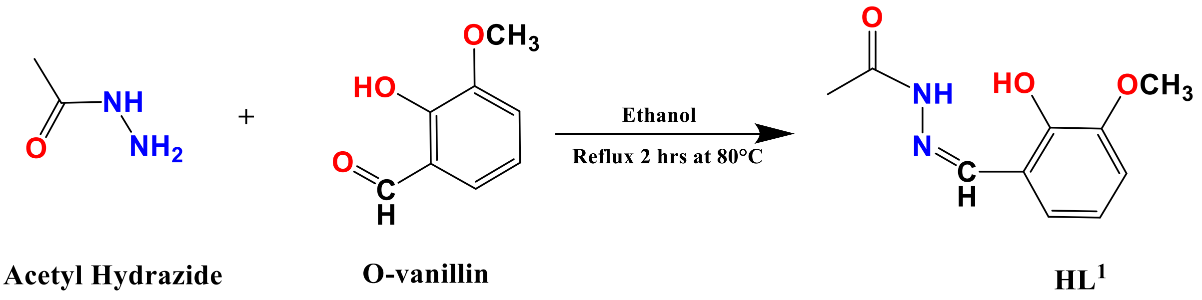

Scheme 1 Synthetic route of ligand $\mathbf{HL^1}$ = (Z)-N'-(2-hydroxy-3-methoxybenzylidene)acetohydrazide.

2.3.2 Synthesis of ligand HL^2

This Schiff base (HL^2) was prepared following the procedure described in the literature [42, 43]. Equimolar ethanolic solutions of 2-hydrazinopyridine (1.091 g, 10 mmol) and 5-bromosalicylaldehyde (2.010 g, 10 mmol) was taken in ethanol (50 mL) and heated under reflux for 3 hrs at 80 °C (Scheme 2). The solvent was removed under reduced pressure and a light yellow solid resulted. Finally obtained Schiff base was washed with ethanol and recrystallized from ethanol.

M.P.: 180 °C. Yield: 79%. Anal. Calc. for $C_{12}H_{10}BrN_3O$ (292.15 g mol^{-1}): Calc. C, 49.34; H, 3.45; N, 14.38%. Found: C, 49.38; H, 3.42; N, 14.36%. FTIR bands (KBr, cm^{-1}): ν(C=N) 1667 m, ν(-OH) 3411 b, ν(N-H) 3017 m. ^{1}H-NMR ($CDCl_3$, 400 MHz) δ: 10.7 (s, ^{1}H, Ar-OH), 8.75 (s, ^{1}H, –NH), 8.74 (s, ^{1}H, –CH=N), 6.8-8.2 (m, 7H, Ar-H ppm. ^{13}C-NMR (DMSO-d_6, 400 MHz) δ: 156 (C-OH), 155 (CH=N), 148 (C-NH), 111 (CH-Br), 106-136 (Ar-C) ppm.

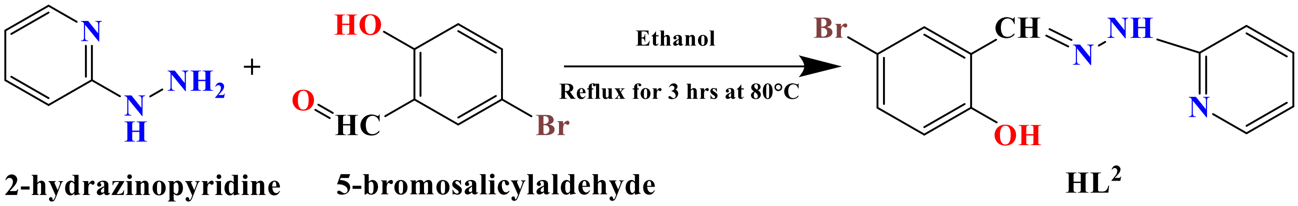

Scheme 2 Synthetic route of $\mathbf{HL^2}$ = (E)-4-bromo-2-((2-(pyridin-2-yl)hydrazono)methyl)phenol.

2.3.3 Synthesis of ligand HL^3

Ethanolic solution of Salicylaldehyde (1.22 g, 10 mmol) and 2-hydrazinopyridine (1.091 g, 10 mmol) was taken in ethanol (50 mL) and heated under reflux for 3 hrs at 80 °C (Scheme 3). The solvent was removed under reduced pressure and a light yellow solid resulted. Finally obtained Schiff base was washed with ethanol and recrystallized from ethanol.

M.P.: 182 °C. Yield: 78%. Anal. Calc. for $C_{12}H_{11}N_3O$ (213.15 g mol^{-1}): Calc. C, 67.59; H, 5.20; N, 19.71%. Found: C, 67.56; H, 5.22; N, 19.68%. FTIR (KBr, cm^{-1}): ν(C=N) 1633 m, ν(-OH) 3385 b, ν(N-H) 3127 m. ^{1}H NMR ($CDCl_3$, 400 MHz) δ: 10.7 (s, 1H, Ar-OH), 8.7 (s, 1H, –NH), 8.2 (s, 1H, –CH=N), 6.8-7.9 (m, 8H, Ar-H) ppm. ^{13}C NMR (DMSO-d_6, 400 MHz) δ: 165 (C-OH) , 157 (CH=N), 136 (C-C), 106 -155 (Ar-C), ppm.

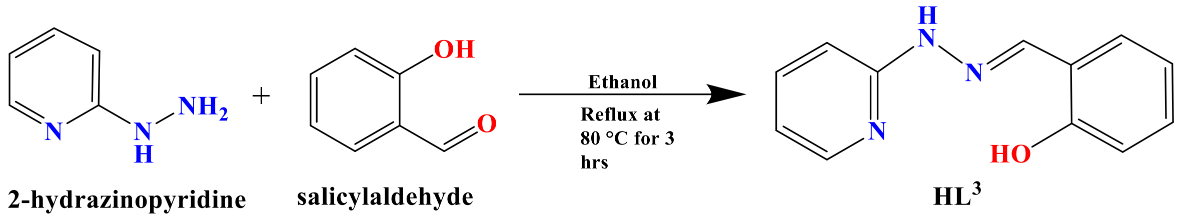

Scheme 3 Synthetic route of **HL**^{3} = (E)-2-((2-(pyridin-2-yl)hydrazono)methyl)phenol.

2.3.4 Synthesis of ligand HL^4

Ethanolic solution of 2-hydroxy-1-napthaldehyde (1.5 g, 10 mmol) and acetylhydrazide (0.65 g, 10 mmol) in ethanol (50 mL) was refluxed for 3 hr at 80°C. The synthetic route of ligand is shown in Scheme 4. The ligand was isolated from the resulting yellow solution as yellow solid. The solid product was washed with hot water and stored in $CaCl_2$ desiccator. The ligand was characterized by microanalysis, FTIR and ^{1}H and ^{13}C NMR study.

M.P.: 182°C. Yield: 81%. Anal. Calc. $C_{13}H_{12}N_2O_2$ (228.25 g mol^{-1}): Calc. C 68.4, H 5.3, N 12.3%. Found: C 68.2, H 5.5, N 12.1%. FTIR (KBr, cm^{-1}): ν(C=N) 1672 m, ν(-OH) 3441 b, ν(N-H) 3041 m. . ^{1}H-NMR ($CDCl_3$, 400 MHz) δ: 11.4 (s, 1H, Ar-OH), 9.2 (s, 1H, –NH), 9.04 (s, 1H, –CH=N), 7.2-8.8 (m, 6H, Ar-H), 2.4 (s, 3H -$COCH_3$) ppm. ^{13}C NMR (DMSO-d_6, 400 MHz) δ: 171 (C-OH), 165 (C=O), 158 (CH=N), 108-157 (Ar-C), 21.8 (-CH_3) ppm.

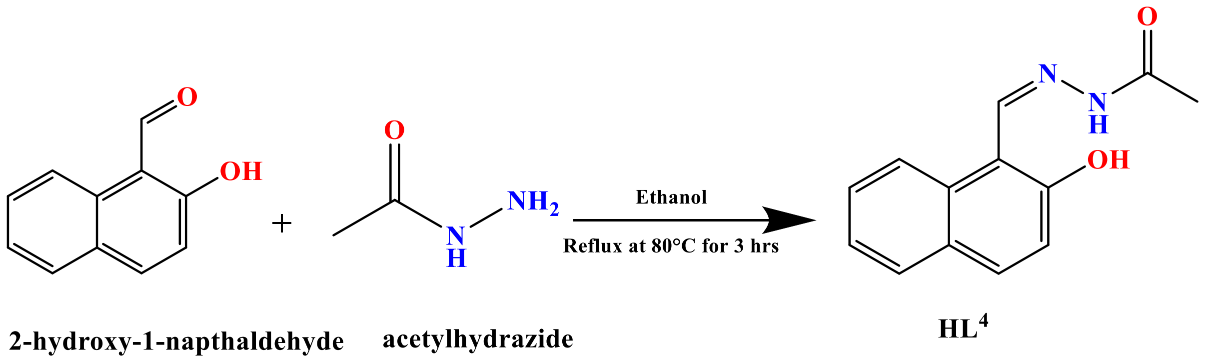

Scheme 4 Synthetic route of **HL**^{4} = (Z)-N'-((2-hydroxynaphthalen-1-yl)methylene)acetohydrazide.

2.3.5 Synthesis of [VO(L^1)(H_2O)]NO_3 1

Vanadyl sulphate monohydrate (0.163 g, 1 mmol) in 10 ml water and Schiff base HL^1 (0.208 g, 1 mmol) in 10 mL methanol were mixed and stirred for 1hrs at ambient temperature. Then 1 mmol sodium nitrate in 5 mL water was added and reflux for 3 hrs 80 ºC. After 2 to 3 hrs burgundy colour solid was separated and filtered off, washed with methanol. Finally, complex dried in a $CaCl_2$ desiccator.

Yield: 87%. Anal. Calc. for $C_{10}H_{13}N_3O_8V$ (354.17 g mol^{-1}): Calc. C, 33.91; H, 3.70; N, 11.86%. Found: C, 33.92; H, 3.72; N, 11.84%. FTIR (KBr, cm^{-1}): ν(C=N) 1633 vs, ν(V=O) 964 vs, ν(V-O) 581 m, ν(V-N) 540 vs.

2.3.6 Synthesis of $[VO(L^2)(H_2O)]NO_3$ 2

Vanadyl sulphate monohydrate (0.163 g, 1 mmol) in 10 ml water and Schiff base HL^2 (0.292 g, 1 mmol) in 10 mL methanol were mixed and stirred for 1hrs at ambient temperature. Then 1 mmol sodium nitrate in 5 mL water was added and refluxed for 3 hrs 80 ºC. After 2 to 3 hrs, the burgundy colour solid was separated and filtered off, washed with methanol. Finally, the complex dried in a $CaCl_2$ desiccator.

Yield: 78%. Anal. Calc. for $C_{12}H_1BrN_4O_6V$ (436.07 g mol^{-1}): Calc. C, 33.05; H, 2.08; N, 12.85%. Found: C, 33.01; H, 2.06; N, 12.83%. FTIR bands (KBr, cm^{-1}): ν(C=N) 1631 vs, ν(V=O) 950 vs, ν(V-O) 453 m, ν(V-N) 446 vs.

2.3.7 Synthesis of $[VO(L^1)(ImH)_2]SO_4.H_2O$ 3

Vanadyl sulphate monohydrate (0.163 g, 1 mmol) in 5 mL water and HL^2 (0.292 g, 1mmol) in 10 mL methanol were mixed and reflux for 1 hrs followed by the addition of an aqueous solution of imidazole (1 mmol). The reaction mixture was refluxed for 3 hrs at 80 ºC. The colour of the solution changedfrom blue to dark burgundy colour. The resulting solution was filtered off and left overnight. A dark burgundy solid was separated, filtered off and washed with methanol and air-dried. Complex was stored in $CaCl_2$ desiccator.

Yield: 82%. Anal. Calc. for $C_{18}H_{17}BrN_7O_7SV$ (605.27 g mol^{-1}): Calc. C, 35.72; H, 2.66; N, 16.20%. Found; C, 35.69; H, 2.63; N, 16.17%. FTIR bands (KBr, cm^{-1}): ν(C=N) 1631 vs, ν(V=O) 949 vs, ν(V-O) 455 m, ν(V-N) 426 vs.

2.3.8 Synthesis of $[VO(L^2)(ImH)]NO_3$ 4

Vanadyl sulphate monohydrate (0.163 g, 1 mmol) in 5 mL water and HL^1 (0.208 g, 1mmol) in 10 mL methanol were mixed and reflux for 1hrs followed by the addition of an aqueous solution of imidazole (1 mmol). The reaction mixture was refluxed for 3 hrs at 80

°C. The colour of the solution changed from blue to dark burgundy colour. The resulting solution was filtered off and left for overnight. A dark burgundy solid was separated, filtered off and washed with methanol and air-dried. Complex was stored in $CaCl_2$ desiccator.

Yield: 76%. Anal. Calc. for $C_{13}H_{15}N_5O_7V$ (404.23 g mol^{-1}): Calc. C, 38.82; H, 3.74; N, 17.64%. Found; C, 38.80; H, 3.71; N, 17.62%. FTIR bands (KBr, cm^{-1}): ν(C=N) 1603 vs, ν(V=O) 972 vs, ν(V-O) 474 m, ν(V-N) 446 vs.

2.3.9 Synthesis of $[V(O)_2L^1]$ 5

A mixture of HL^1 (0.213 gm, 1 mmol) in 10 mL methanol was mixed with $[VO(acac)_2]$ (0.265 g, 1 mmol) and then refluxed for 3 hrs at 80°C. The reaction mixture was cooled to room temperature and allowed to evaporate slowly in the open air. After 3-4 days, brown colour crystals were obtained, which were collected upon filtration, washed with methanol and dried in $CaCl_2$ desiccator.

Yield: 65%. Anal. Calc. for $C_{12}H_{10}N_3O_3V$ (295.17 g mol^{-1}): Calc. C 48.83, H 3.41, N 14.24%. Found: C 48.85, H 3.44, N 14.21%. FTIR bands (KBr, cm^{-1}): ν(C=N) 1601 vs, ν(V=O) 988 vs, ν(V-O) 510 m, ν(V-N) 471 vs.

2.3.10 Synthesis of $[V(O)_2L^2]$ 6

A mixture of HL^2 (0.227 g, 1 mmol) in 20 mL methanol was mixed with $[VO(acac)_2]$ (0.265 g, 1 mmol) and the resulting reaction mixture was refluxed for 3 hrs 80 °C. The reaction mixture was cooled to room temperature and allowed to evaporate slowly in the open air. After 3-4 days, brown colour crystals were obtained, which were collected upon filtration, washed with methanol and dried in $CaCl_2$ desiccator.

Yield: 65%. Anal. Calc. for $C_{13}H_{11}N_2O_4V$ (310.18 g mol^{-1}): Calc. C 50.34, H 3.57, N 9.03%. Found: C 50.37, H 3.54, N 9.01%. FTIR bands (KBr, cm^{-1}): ν(C=N) 1601 vs, ν(V=O) 964 vs, ν(V-O) 443 m, ν(V-N) 421 vs.

2.3.11 Synthetic of $[VO_2(L^1)]ImH$ 7

Vanadium pentoxide (0.181 g, 1 mmol) and HL^1 (0.208 g, 1 mmol) in 10 mL methanol were mixed and stirred for 1 hrs followed by the addition of an aqueous solution of imidazole (1 mmol). The reaction mixture was refluxed for 3 hrs at 80 °C. The colour of the solution changed from white to yellow colour. The resulting solution was filtered and washed with methanol. After one-week yellow colour crystals which were suitable for X-ray analysis separated.

Yield: 82%. Anal. Calc. for $C_{13}H_{15}N_4O_5V$ (358.23 g mol^{-1}): Calc. C, 43.59; H, 4.22; N, 15.64%. Found: C, 43.58; H, 4.25; N, 15.62%. FTIR bands (KBr, cm^{-1}): ν(C=N) 1657 vs, ν(V=O) 966 vs, ν(V-O) 432 m, ν(V-N) 410 vs.

2.4 Computational Studies

All DFT calculations were carried out using the GAUSSIAN 09 program package [44, 45] by the DFT/B3LYP method [46-48].The input files of the vanadium(V) complexes were prepared with Gauss View 5.0.9 [49]. During optimization, the anion was ignored and only the cationic complexes were taken into account. The electronic excitations of the vanadium(V) complexes were made by using the time-dependent density functional theory (TD-DFT)/B3LYP method with a LANL2DZ basis set in the gas phase [50]. Vertical electronic excitations based on B3LYP optimized geometries were computed using the time-dependent density functional theory (TD-DFT) [51] in DMSO with a conductor-like polarizable continuum model (PCM) [52].

2.5 Hirshfeld Surface Analysis(HAS)

Molecular Hirshfeld surfaces [53] in the crystal structure were constructed based on the electron distribution calculated as the sum of spherical atom electron densities [54, 55]. For a given crystal structure and a set of spherical atomic densities, the Hirshfeld surface is unique [56]. The normalized contact distance (d_{norm}) based on both d_{e} and d_{i} (where d_{e} is the distance from a point on the surface to the nearest nucleus outside the surface and d_{i} is the distance from a point on the surface to the nearest nucleus inside the surface) and the vdW radii of the atom, as given by equation 1 enables identification of the regions of particular importance to intermolecular interactions [53]. The combination of d_{e} and d_{i} in the form of a two-dimensional (2D) fingerprint plot [57, 58] provides a summary of intermolecular contacts in the crystal [53]. The Hirshfeld surfaces mapped with d_{norm} and 2D fingerprint plots were generated using the Crystal-Explorer 2.1 [59]. Graphical plots of the molecular Hirshfeld surfaces mapped with d_{norm} used a red-white-blue colour scheme, where red highlight shorter contacts, white represents the contact around vdW separation, and blue is for longer contact. Additionally, two further coloured plots representing shape index and curvedness based on local curvatures are also presented in this paper[60].

$$d_{\mathrm{norm}} = \frac{d_i - r_i^{\mathrm{vdW}}}{r_i^{\mathrm{vdW}}} + \frac{d_e - r_e^{\mathrm{vdW}}}{r_e^{\mathrm{vdW}}} \qquad \text{....(1)}$$

2.6 Docking Studies

Docking experiments were performed to study the molecular binding behaviour of four vanadium complexes with alpha-glucosidase enzyme. X-ray crystallographic structure of alpha-glucosidase enzyme was retrieved from protein databank having PDBid-3WY1 [61, 62] and the 3D structure of the vanadium complexes which were used as ligands were modelled in Marvin Sketch [63]. Auto dock 4 was used with the genetic algorithm method for the docking studies [64]. The docking methodologies previously described in the literature were used for studies [65-67]. The shape and properties of the receptor were EPR presented by computing a grid box of (126× 126 × 126 Å) using the Receptor Grid Generation Panel. The docking protocol was validated by re-docking the co-crystallized ligand into the active site of the protein. Consequently, it is followed by docking of the vanadium derivatives into the defined grid box. To soften the potential for nonpolar part of protein wonder Waals scaling factor was kept at 1.0, partial atomic charge cut-off at 0.25 with a Coulomb-vdW cut-off 50 kcal/mol. Further, the docking study was executed against the protein prepared, thereby exploring the different binding interaction of the hits with long evaluations generating 500 poses for each run. The scoring function estimates the poses of the ligand with the receptor. Finally, the docking poses of top-scored hits were visualized by the Discovery Studio-4.5 visualizer.

2.7 Antidiabetic activity

2.7.1 α-Glucosidase inhibition activity

The α-glucosidase inhibitory activity assay was performed by following the method of Tripathi et al. [68] and Gomathi et al. [69]. In brief, Rat-intestinal acetone powder was dissolved in 100 mL of saline water and sonicated properly at 4°C. After sonication, the suspension was centrifuged (3,000 rpm, 4°C, 30 minutes) and the resulting supernatant was used for the assay. A reaction mixture containing 50 µL of phosphate buffer (50 mM; pH 6.8), 50 µL of rat α-glucosidase and 50 µL sample of varying concentrations (100-800 µg/mL) was pre-incubated for 5 min at 37°C, and then 50 µL of 3 mM PNPG was added to the mixture as a substrate. After incubation at 37°C for 30 min, enzymatic activity was quantified by measuring the absorbance at 405 nm in a microtitre plate reader (Bio-TEK, USA). Acarbose was used as standard and experiments were done in triplicates.

The percentage of enzyme inhibition by the sample was calculated by the following formula:

$$\% \text{ Inhibition} = \{[(AC - AS)/AC] \times 100\}$$

where AC is the absorbance of the control and AS is the absorbance of the tested sample. The concentration of inhibitor required to inhibit fifty percent of enzyme activity under the mentioned assay conditions is defined as the IC_{50} value.

2.7.2 α–Amylase inhibition activity

Pancreatic α-amylase assay was adopted from Apostolidiset al. [70]. 50 µL of different dilutions of test compounds and 50 µL of 0.02 M sodium phosphate buffer (pH 6.9 with 0.006 M sodium chloride) containing α-amylase solution (0.5 mg/ mL) were incubated at 25°C for 10 min. After pre-incubation, 50 µL of 1% starch solution in 0.02 M sodium phosphate buffer (pH 6.9 with 0.006 M sodium chloride) was added to each tube. The reaction was incubated at 25°C for 10 min. The reaction was stopped with 100 µL of DNS colour reagent. Microplates were incubated (85-90°C) for 10 min to develop colour and left to cool at room temperature. The reaction mixture was diluted with 105 µL of distilled water. Enzymatic activity was quantified by measuring the absorbance at 540 nm in a microtitre plate reader (Bio-TEK, USA). Acarbose was used as standard and experiments were done in triplicates.

3 Results and discussion

3.1 Synthetic Strategy

All seven complexes **1-7** of the composition $[VO(L^1)(H_2O)]NO_3$ **1**, $[VO(L^2)(H_2O)]NO_3$ **2**, $[VO(L^2)(ImH)_2]SO_4.H_2O$ **3** $[VO(L^1)ImH]NO_3$ **4**, $[VO_2(L^3)]$ **5**, $[VO_2(L^4)]$ **6** and $[VO_2(L^1)]ImH$ **7** were synthesized. The ligands HL^1, HL^2, HL^3 and HL^4 were synthesized from the condensation of respective aldehydes and hydrazines in ethanol. The synthetic route of complexes is given in Scheme 5 and 6. These Schiff bases were isolated with sufficient purity and used for complex formation without further purification. Upon reaction of HL^1 and HL^2 with vanadyl solution in methanol resulted in **1** and **2**. Mixed ligand complexes **3** and **4** were synthesized by the following method adopted for **1** and **2** with the addition of aqueous imidazole solution. Similarly, complexes **5-7** were synthesized using HL^3, HL^4 and HL^1 respectively. All seven complexes are stable in air and soluble in DMF, DMSO, but insoluble in H_2O, benzene and $CHCl_3$. These complexes were characterized based on microanalysis, IR, UV-Vis, CV and EPR spectroscopy techniques. Complex **3, 5-7** was also characterized by single-crystal analysis. The room temperature magnetic measurements of complex **1**, **2** and **4** are in the range of 1.79 to 1.83 B.M. This range of magnetic moment values of complexes **1**, **2** and **4** is consistent with one unpaired electron (S = 1/2) in $d_{x^2-y^2}$ ascribed to the paramagnetic behaviour of these complexes. The room temperature magnetic susceptibilities values of complexes **3**, **5-7** indicate the diamagnetic character of these complexes. Thus, these complexes are in +5 oxidation state. The molar conductance of all complexes was measured in 100 × 10^{-3} M DMSO solution. The molar conductance value of complexes **1-4** and **7** are 112, 120, 92, 100 and 97 (Ω^{-1} cm^2 mol^{-1}) respectively. Complex **5** and **6** showing less value of molar conductance which proves that they are non-electrolytic.

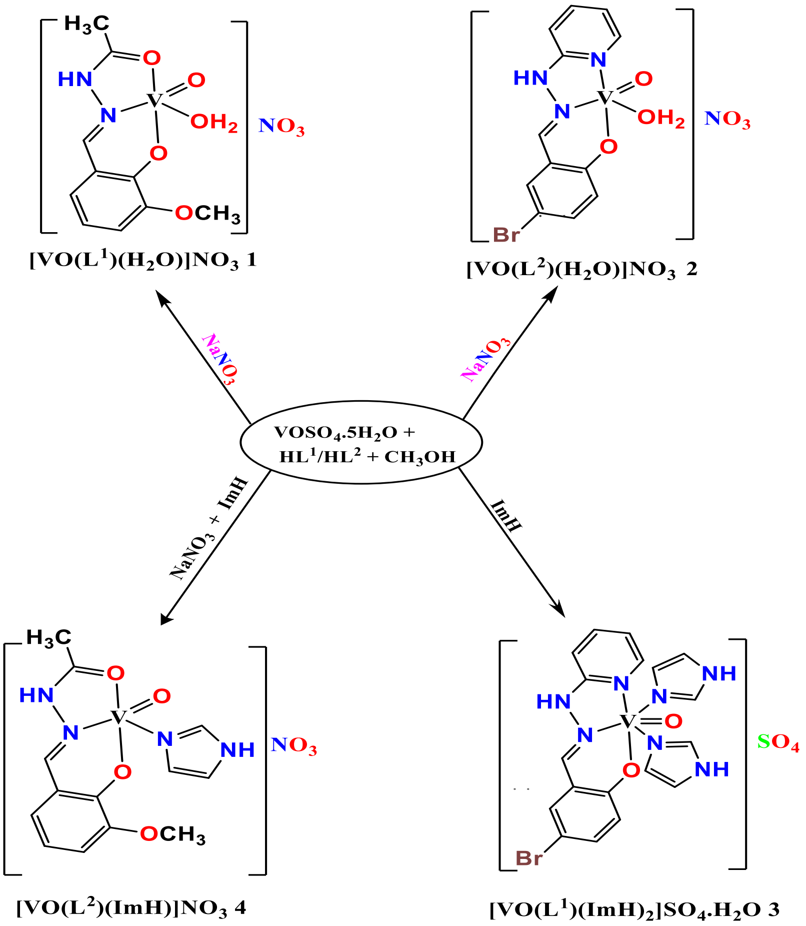

Scheme 5 Synthetic route of complexes **1-4**.

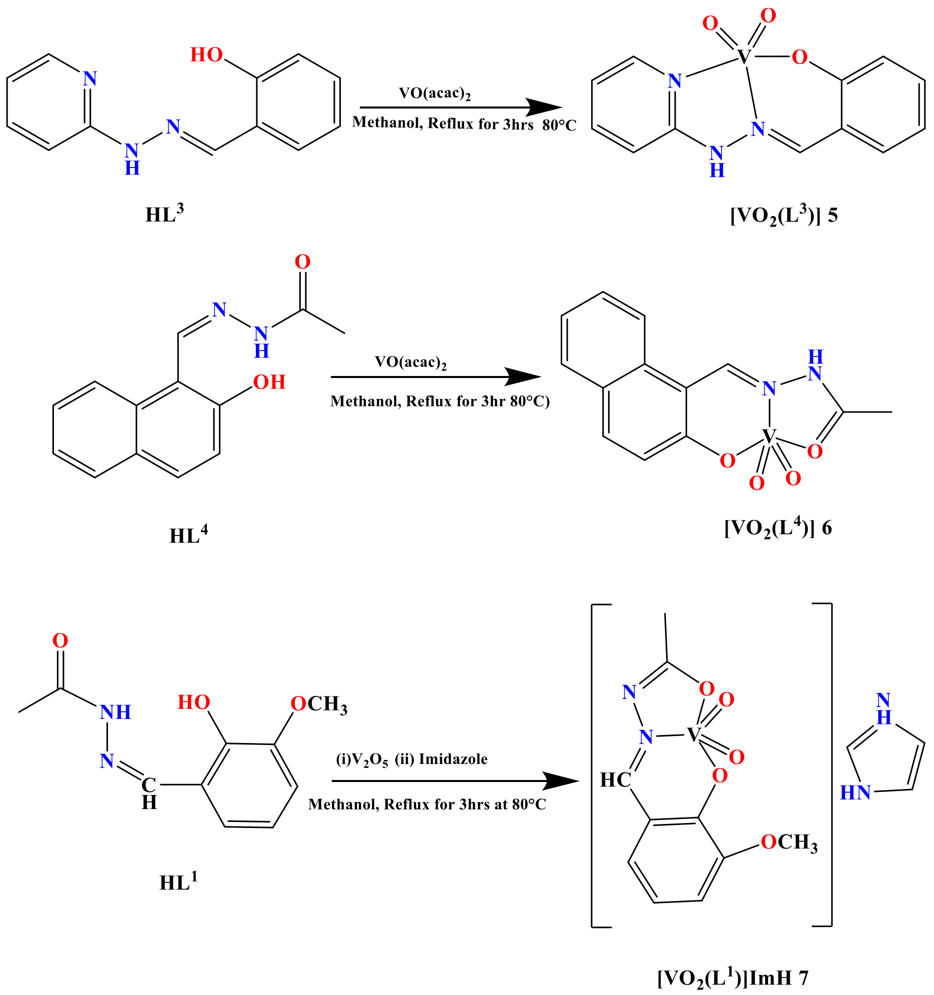

Scheme 6 Synthetic route of complexes **5-7**.

3.2 NMR spectra of Ligands

The proton NMR of ligands HL^1, HL^2, HL^3 and HL^4 were recorded in CDCL$_3$ solvent at room temperature. Proton NMR spectra of the ligands showed a sharp signal (singlet) in the range between 8.8-8 ppm, which can be assigned to the azomethine proton. Similarly, hydroxyl proton (OH) is obtained in the range of ~ 10.8-10.4 ppm. Hydrazide N-H proton appear in the range of 10.2-8.7 ppm. In ligands, the aromatic proton peaks are observed in the range of 6-8 ppm. In ligand HL^1 and HL^4 methyl (-COCH$_3$) proton appears at 2.3 and 2.4 ppm respectively. The ^{1}H NMR spectra of ligands are given in Fig. 1-4. The ^{13}C NMR spectra of the ligands were recorded in DMSO-d$_6$. Similarly, carbonyl (C=O) carbon peaks and azomethine carbon (CH=N-)are obtained in the range of ~ 165 and 146 ppm. Similarly, aromatic carbon peaks are obtained in the range of 157-106 ppm. In ^{13}C NMR of ligand HL^1 and HL^4 methyl, (-CH$_3$) carbon peaks appear at ~ 21.82 ppm. The ^{13}C NMR of the ligand is shown in Fig. 5-8.

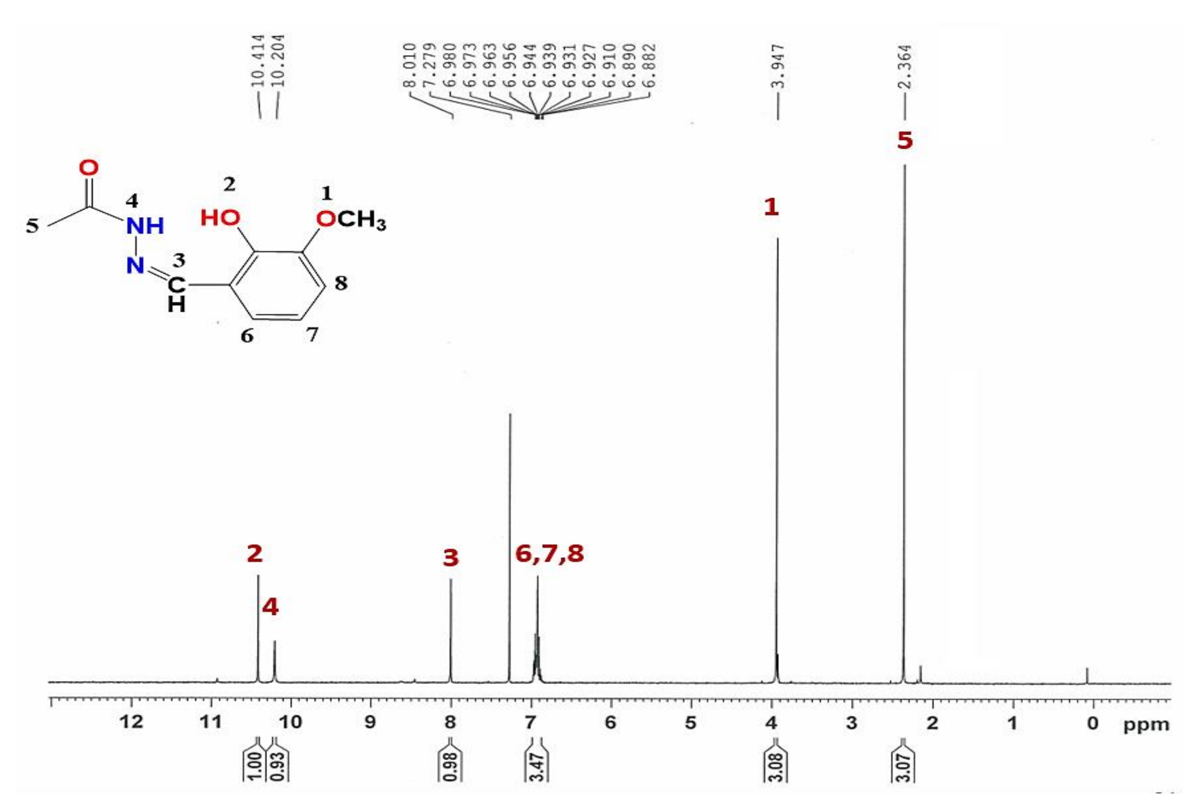

Fig. 1. ^{1}H NMR of ligand **HL^1** in CDCl$_3$.

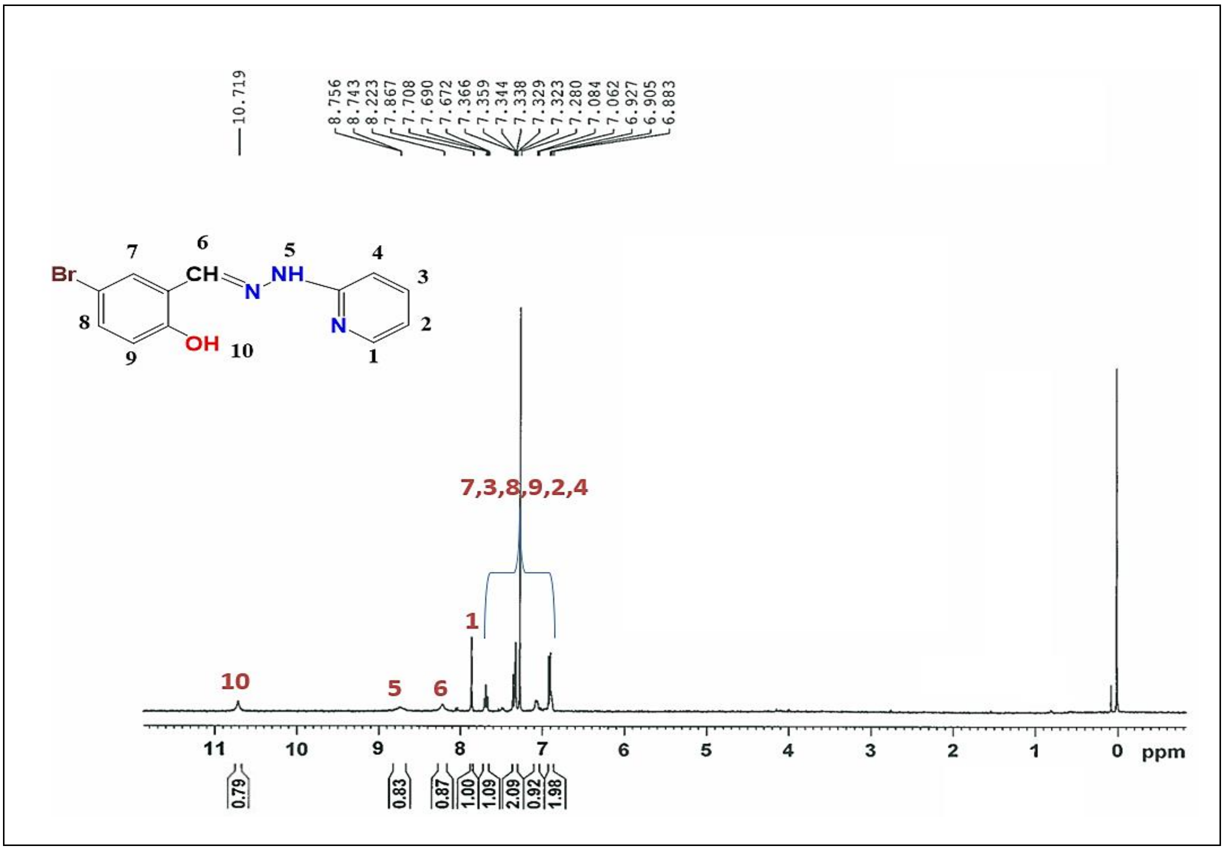

Fig. 2. ^{1}H NMR of ligand **HL^2** in CDCl$_3$.

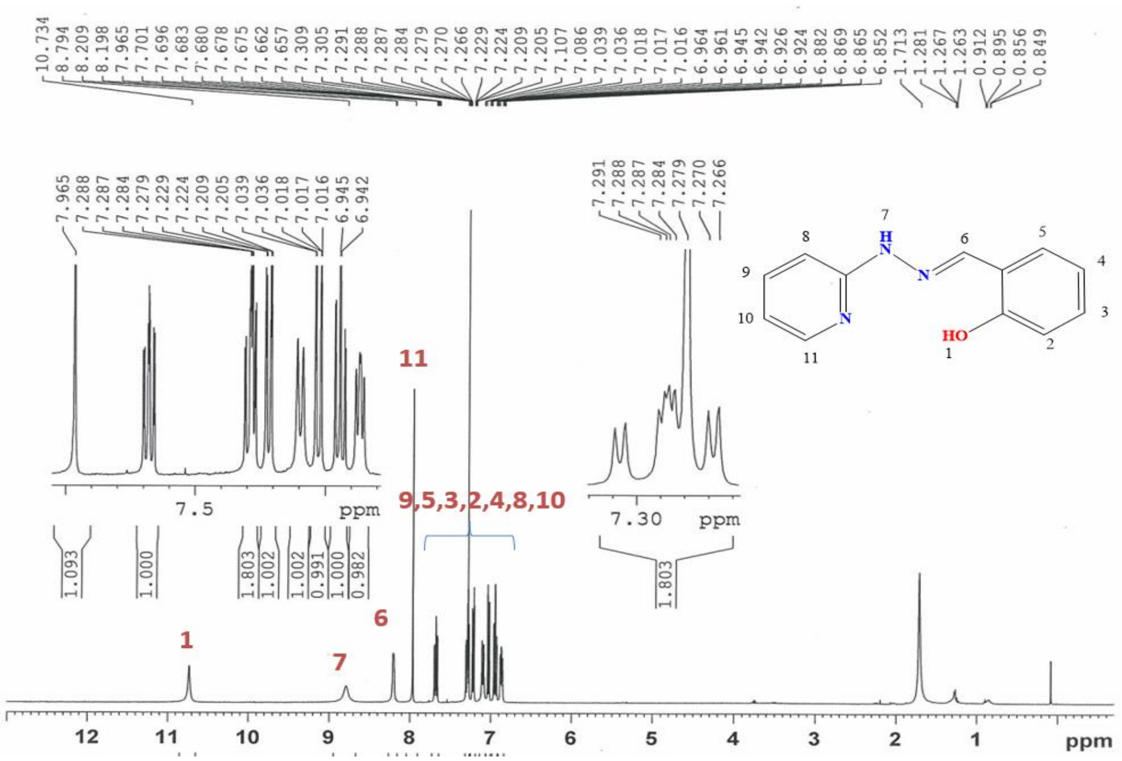

Fig. 3. ^{1}H NMR of ligand **HL^3** in CDCl$_3$.

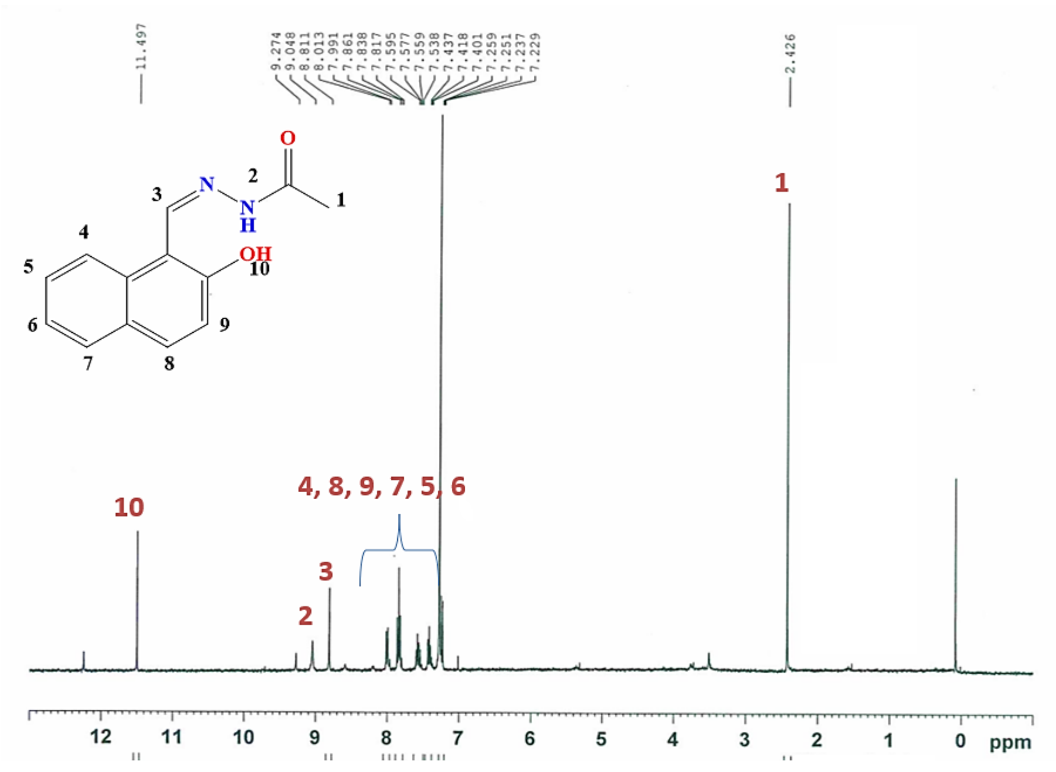

Fig. 4. ^{1}H NMR of ligand **HL^4** in CDCl$_3$.

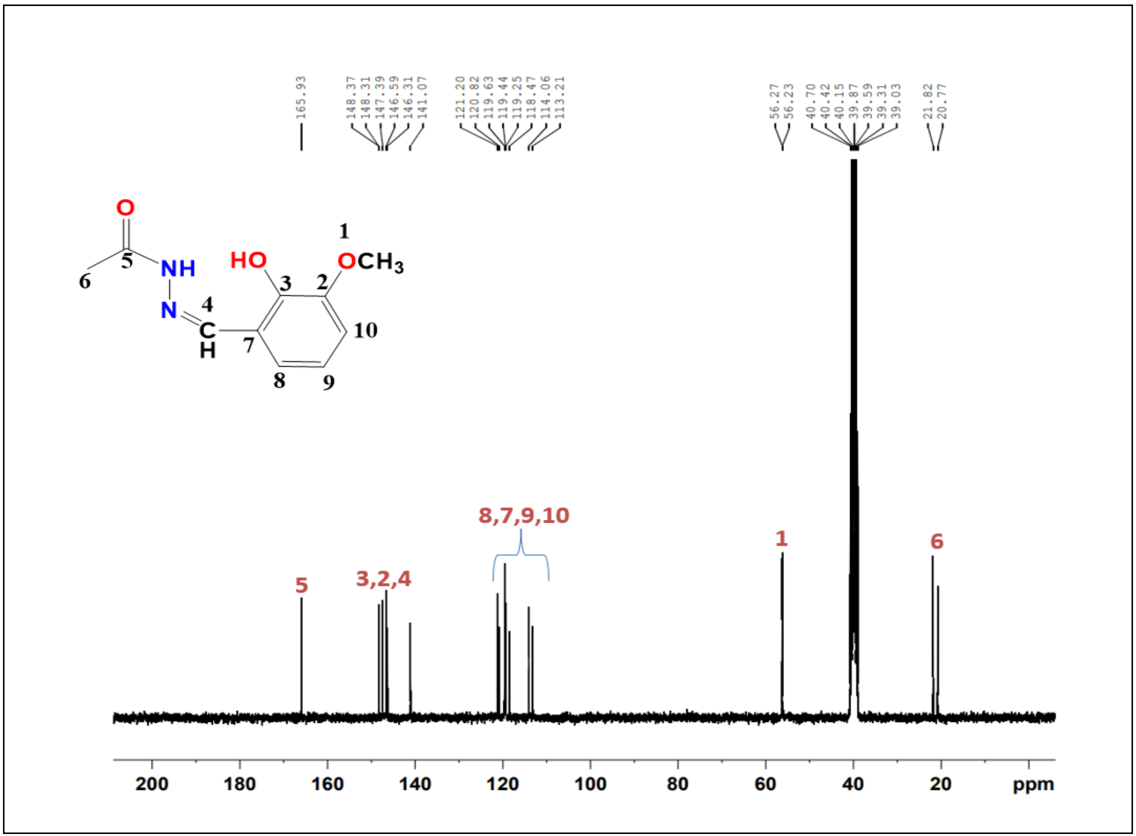

Fig. 5. ^{13}C NMR of ligand **HL^1** in DMSO-d$_6$.

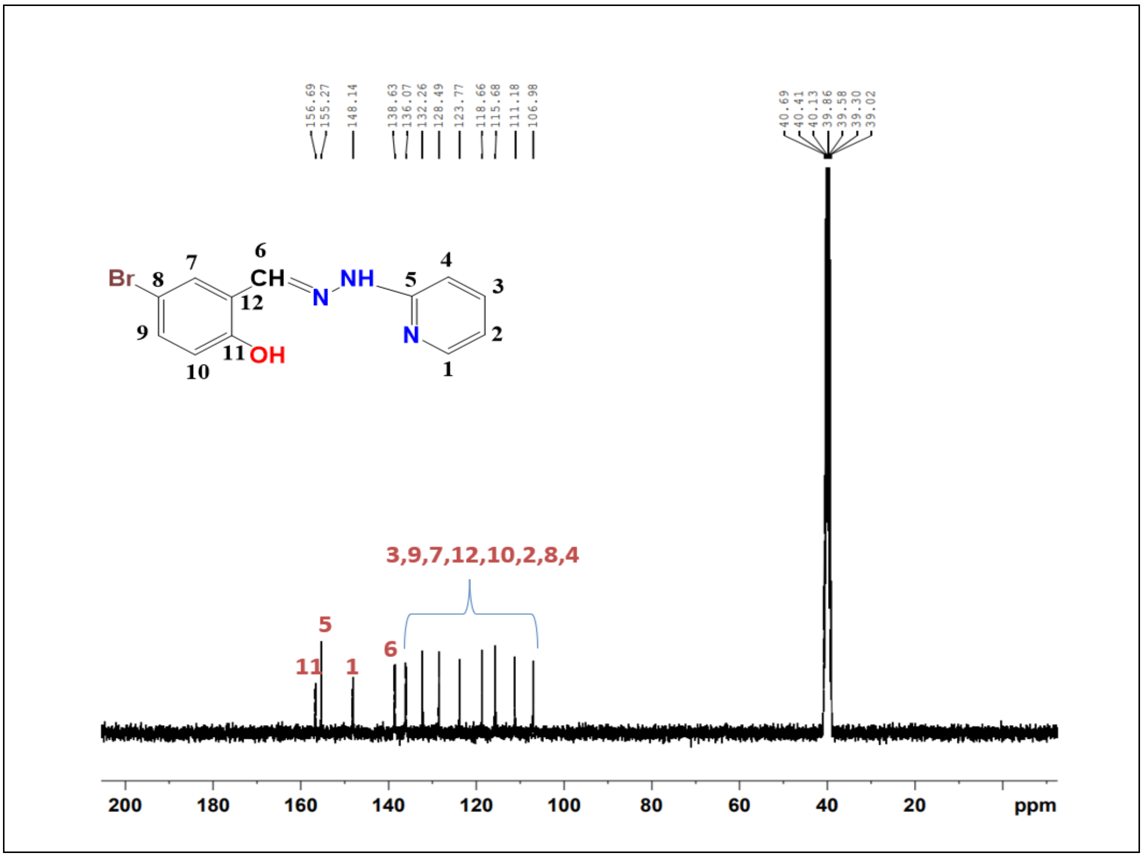

Fig. 6. ^{13}C NMR of ligand **HL^2** in DMSO-d$_6$.

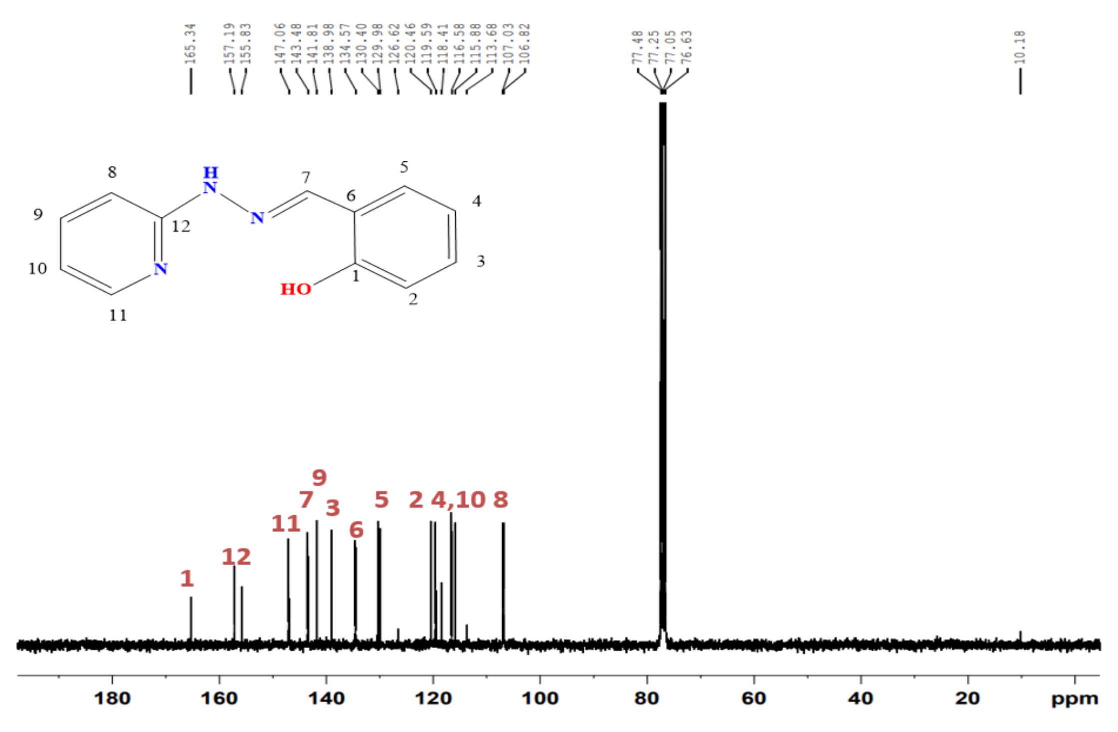

Fig. 7. ^{13}C NMR of ligand **HL^3** in DMSO-d$_6$.

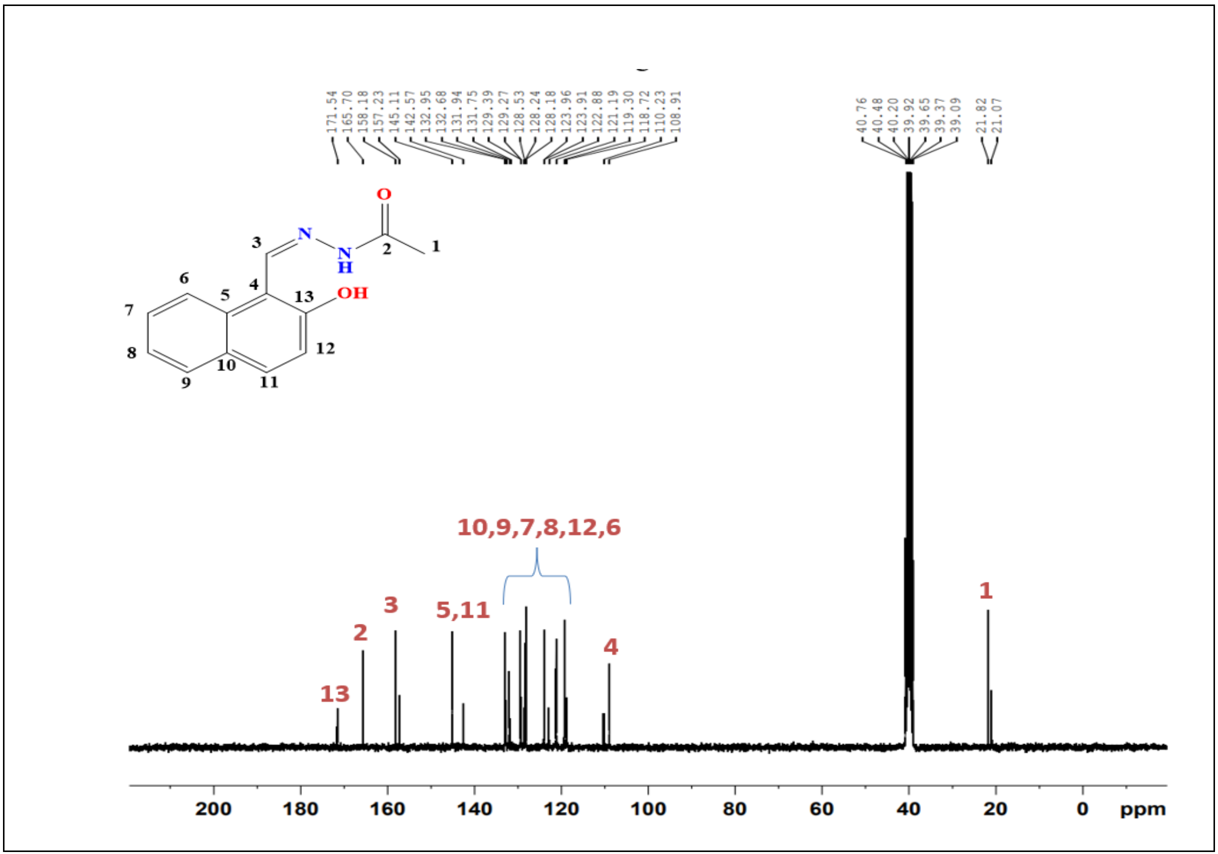

Fig. 8. ^{13}C NMR of ligand **HL^4** in DMSO-d$_6$.

3.3 FTIR Analysis

All Schiff bases ligand (HL^1-HL^4) show strong bands in the region 3411-3441 cm^{-1} and 3017-3127 cm^{-1} which are assigned to ν(OH) and ν(N-H) respectively. The stretching frequency for azomethine ν(C=N) in the ligand is between the range 1633-1679 cm^{-1}.The absence of ν(OH) band at a 3400 cm^{-1} in the corresponding metal complexes due to deprotonation upon coordination. In complexes, the ν(C=N) bands are now located at 1601-1657 cm^{-1}, indicating complexation of azomethine nitrogen to the vanadium [71]. A new band around~1596±2 cm^{-1} in all complexes is assigned to the ν(C−O) vibration [72, 73]. In complexes,**1**, **2**, and **4** ν(NO_3) is seen at ~1405, 1378 and 821 cm^{-1} indicating the ionic nature of nitrate anion [74]. Similarly, in complex **3** a sharp band at 1365 cm^{-1} is due to sulphate ion. All complexes show one sharp band at around ~ 949-988 cm^{-1} assigned to stretching vibration of oxidovanadium moiety ν(V=O) [75]. In complex **1** and **2** a broadband 3432 and 3422cm^{-1} is due to coordinated water molecules in both complexes. In complex **6**, carbonyl band ν(C=O) at 1620 cm^{-1}. However, some peaks medium to weak intensities found in the range 410-481 cm^{-1} in all complexes are assigned to (M−O / M−N) stretching modes [76]. The FTIR spectral data are shown in Table 1. FTIR spectra of ligands and complexes are presented in Fig. 9-19.

Table 1 Summary of FTIR data of Ligand and complexes.

Compound	ν(OH) / (H_2O)	ν(NH)	ν(C=N)	ν(V=O)	ν(V-O)	ν(V-N)
HL^1	3433	3015	1679	-	-	-
HL^2	3411	3017	1667	-	-	-
HL^3	3385	3127	1633	-	-	-
HL^4	3441	3041	1672	-	-	-
1	3432	-	1624	964	581	540
2	3422	-	1633	950	453	446
3	-	-	1631	949	455	426
4	-	-	1603	972	474	446
5	-	-	1601	988	510	471
6	-	-	1601	964	443	421
7	-	-	1657	966	432	410

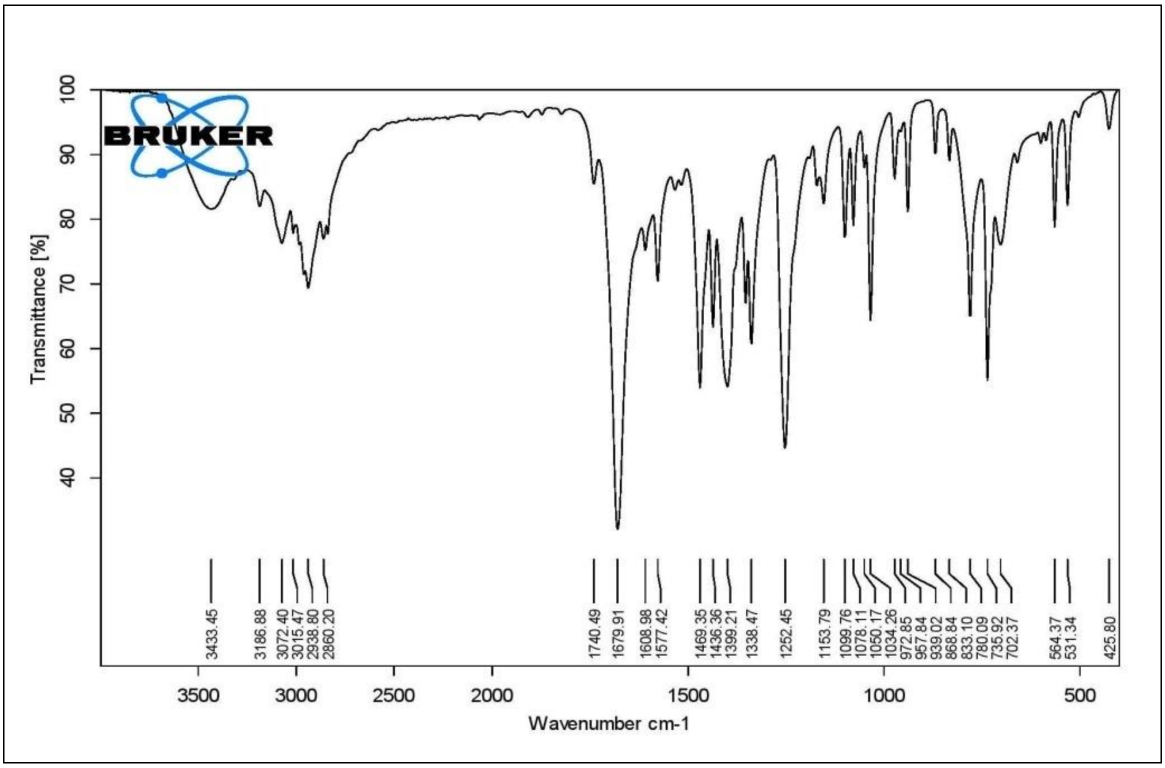

Fig. 9. FTIR spectrum of ligand **HL^{1}**.

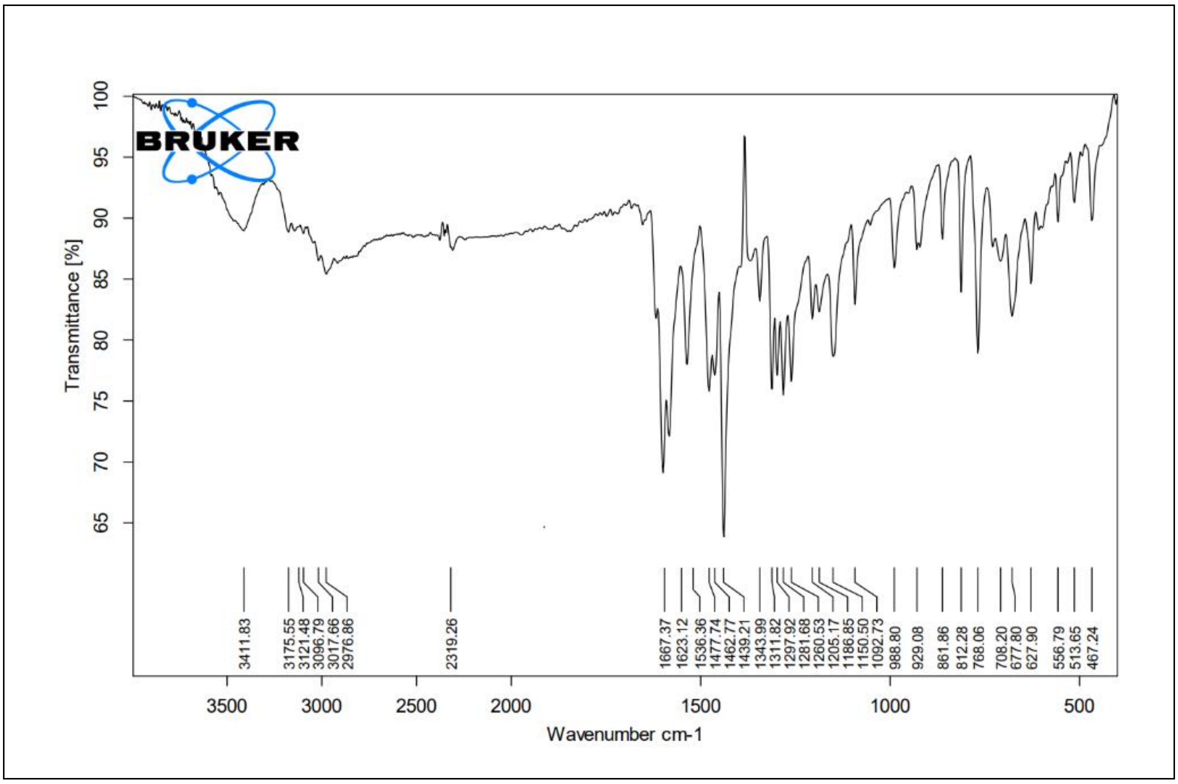

Fig. 10. FTIR spectrum of ligand **HL^{2}**.

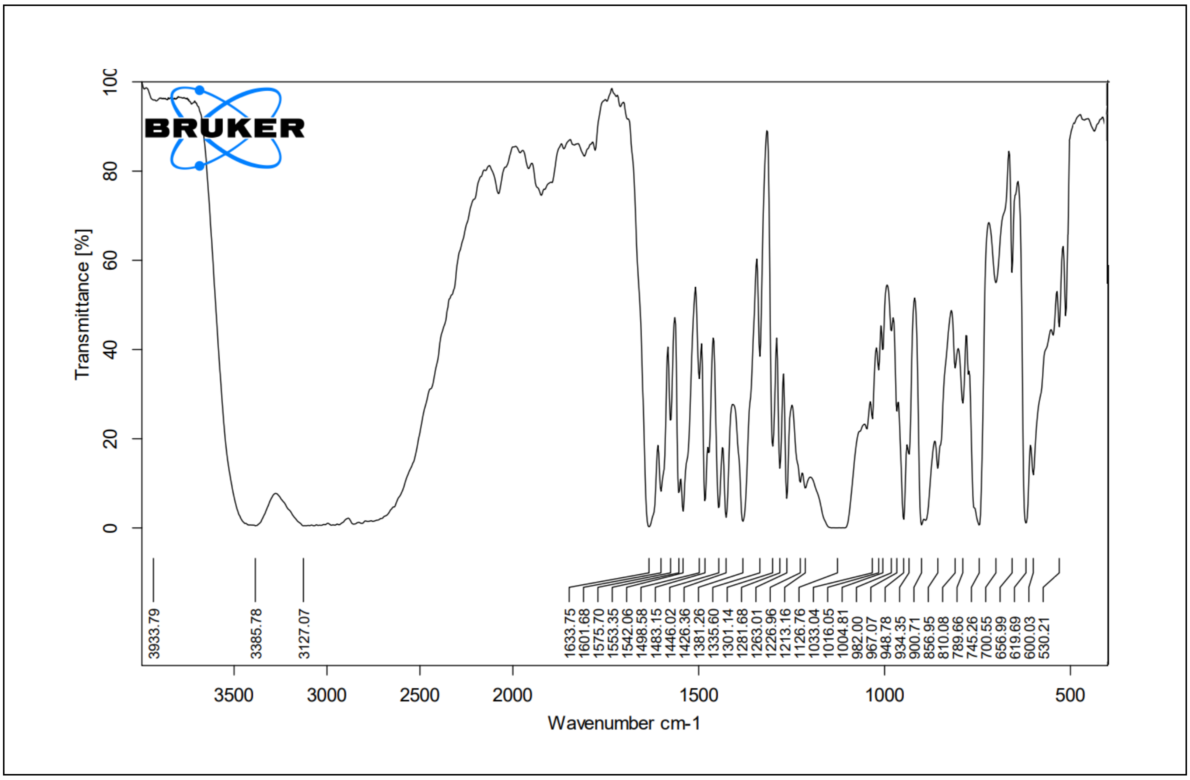

Fig. 11. FTIR spectrum of ligand **HL^3**.

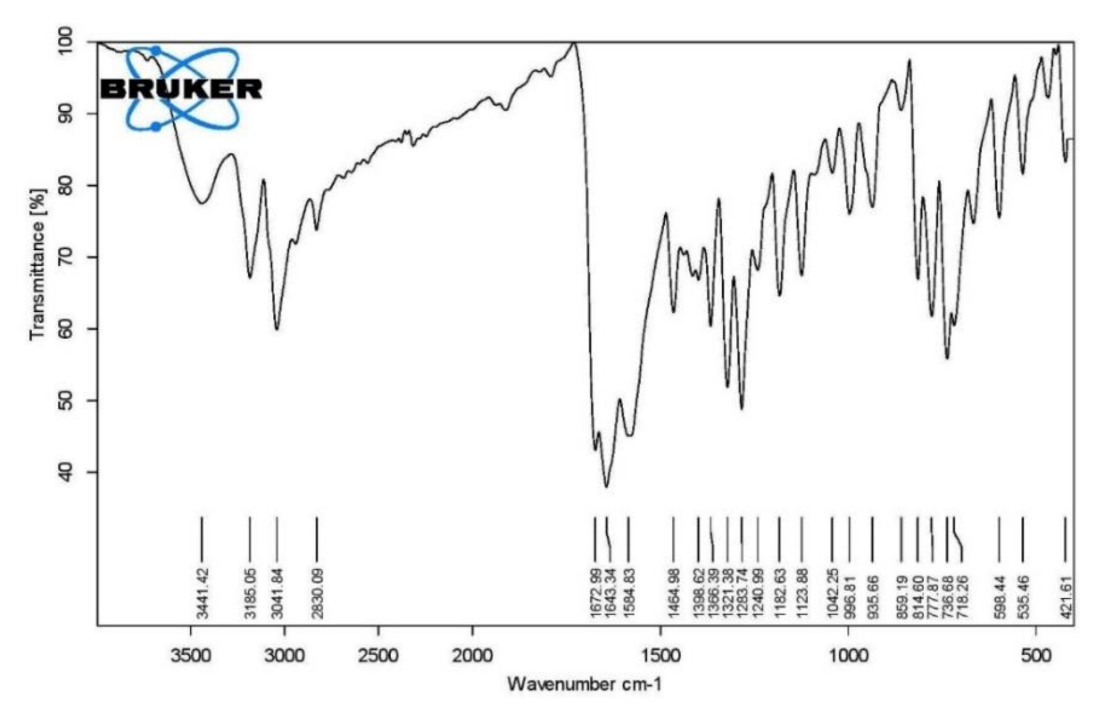

Fig. 12. FTIR spectrum of complexes **HL^4**.

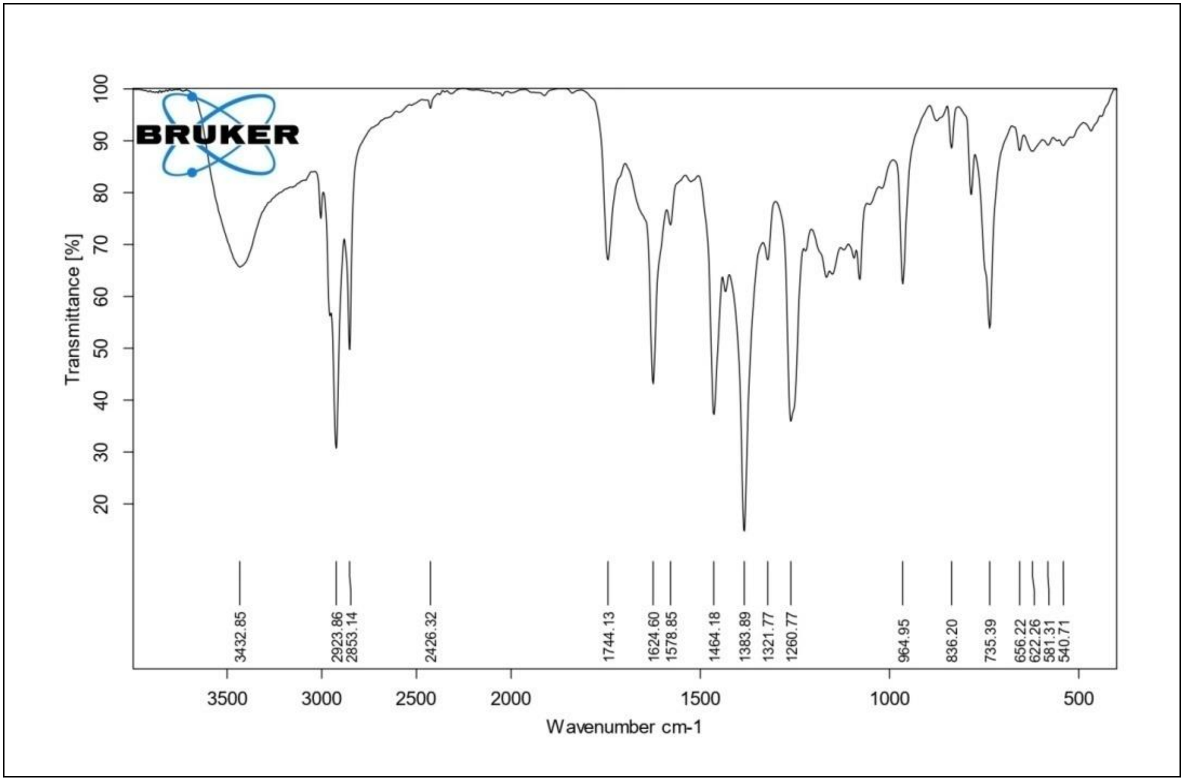

Fig. 13. FTIR spectrum of complexes **1**.

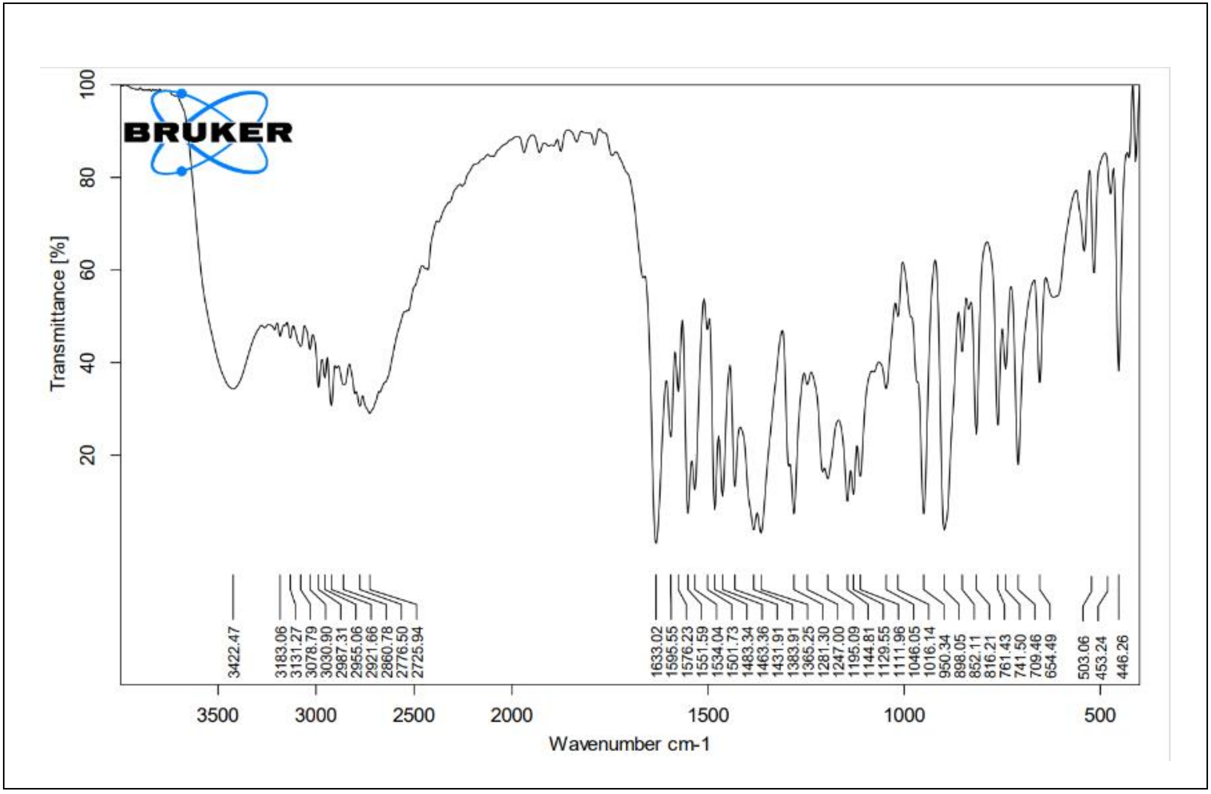

Fig. 14. FTIR spectrum of complexes **2**.

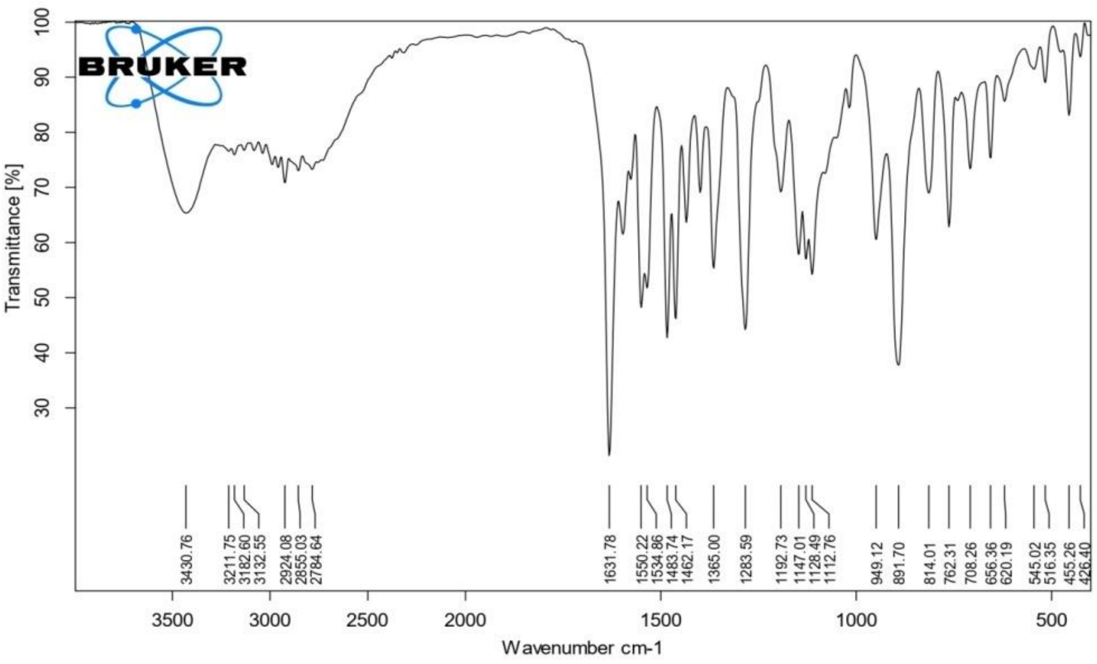

Fig. 15. FTIR spectrum of complexes **3**.

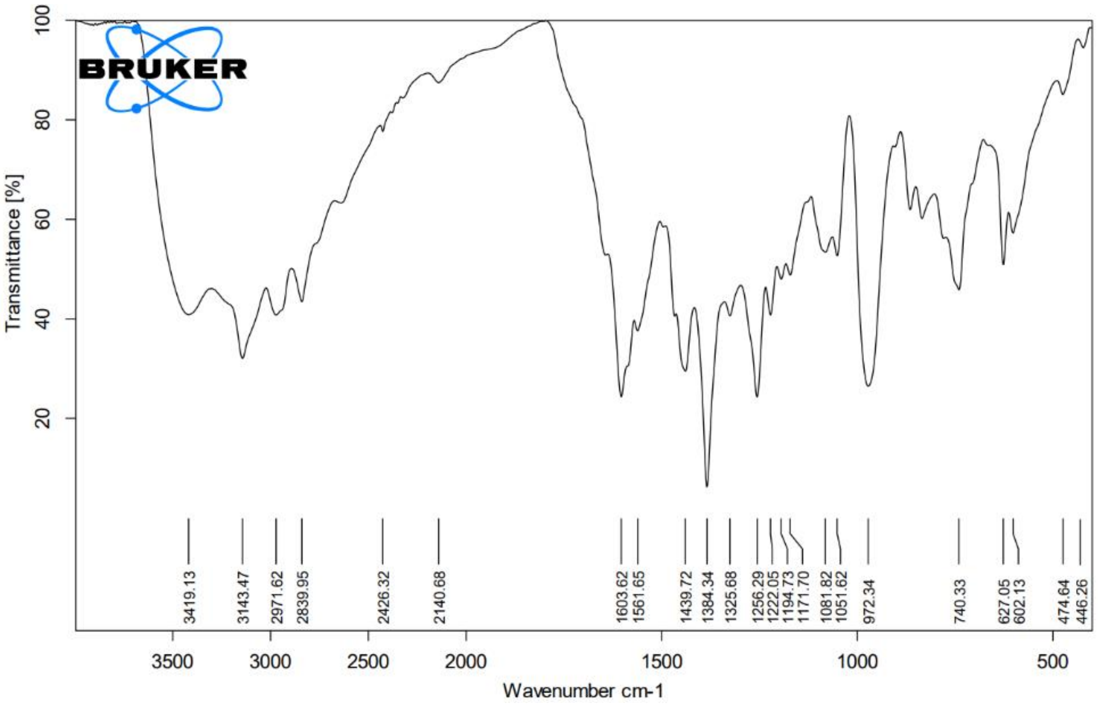

Fig. 16. FTIR spectrum of complexes **4**.

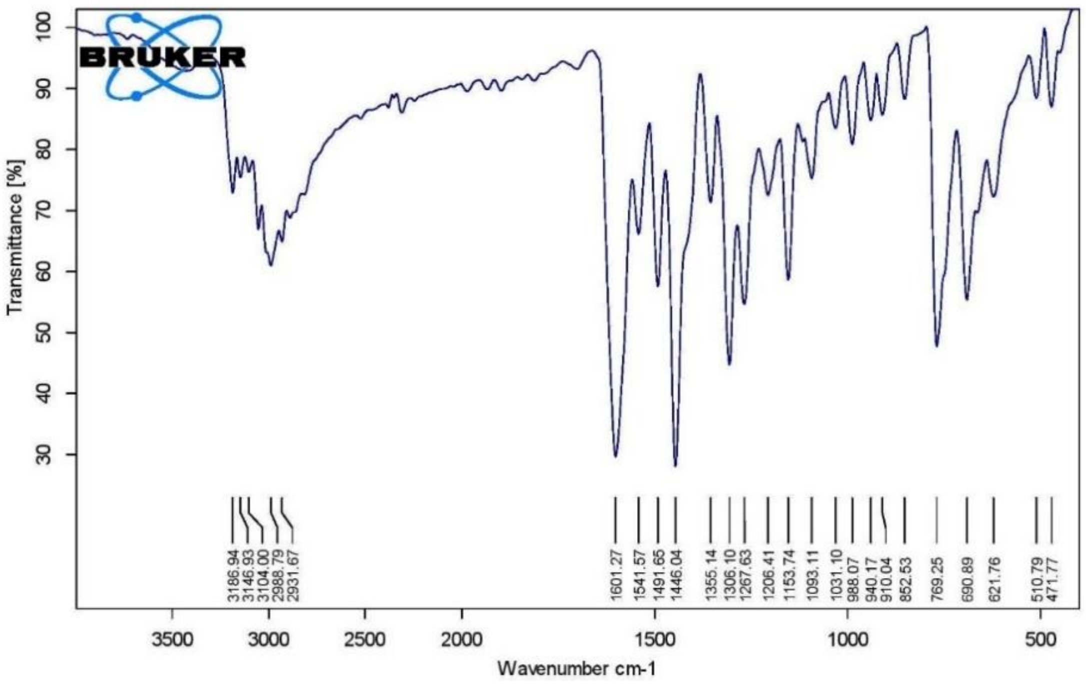

Fig. 17. FTIR spectrum of complexes **5**.

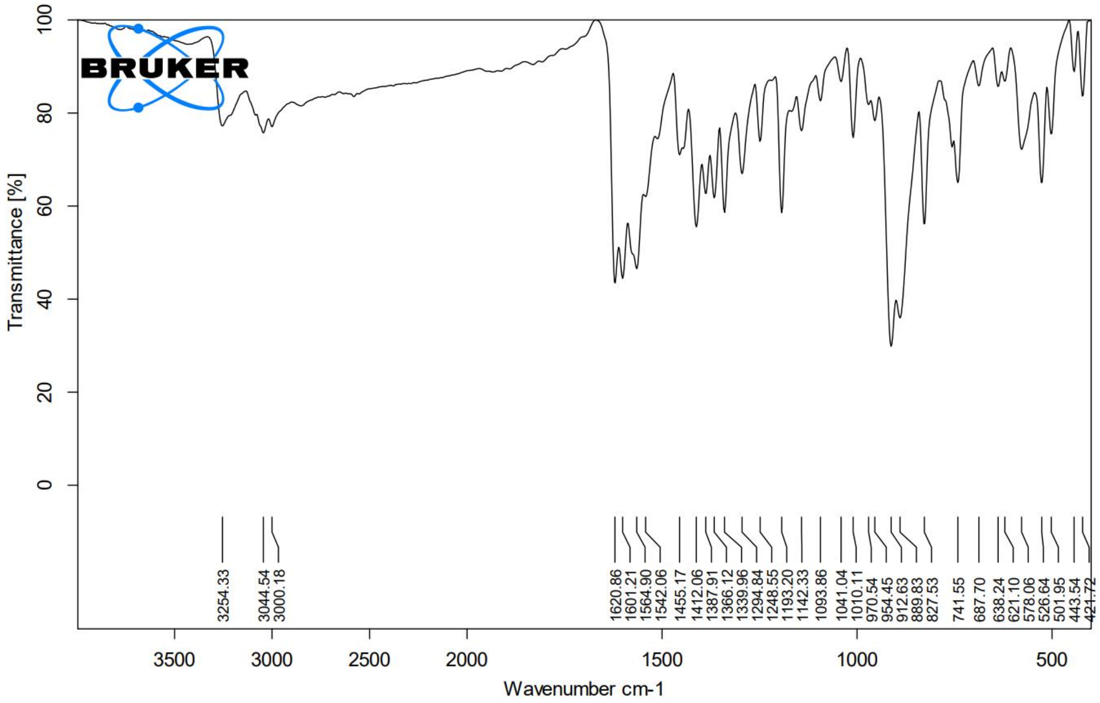

Fig. 18. FTIR spectrum of complexes **6**.

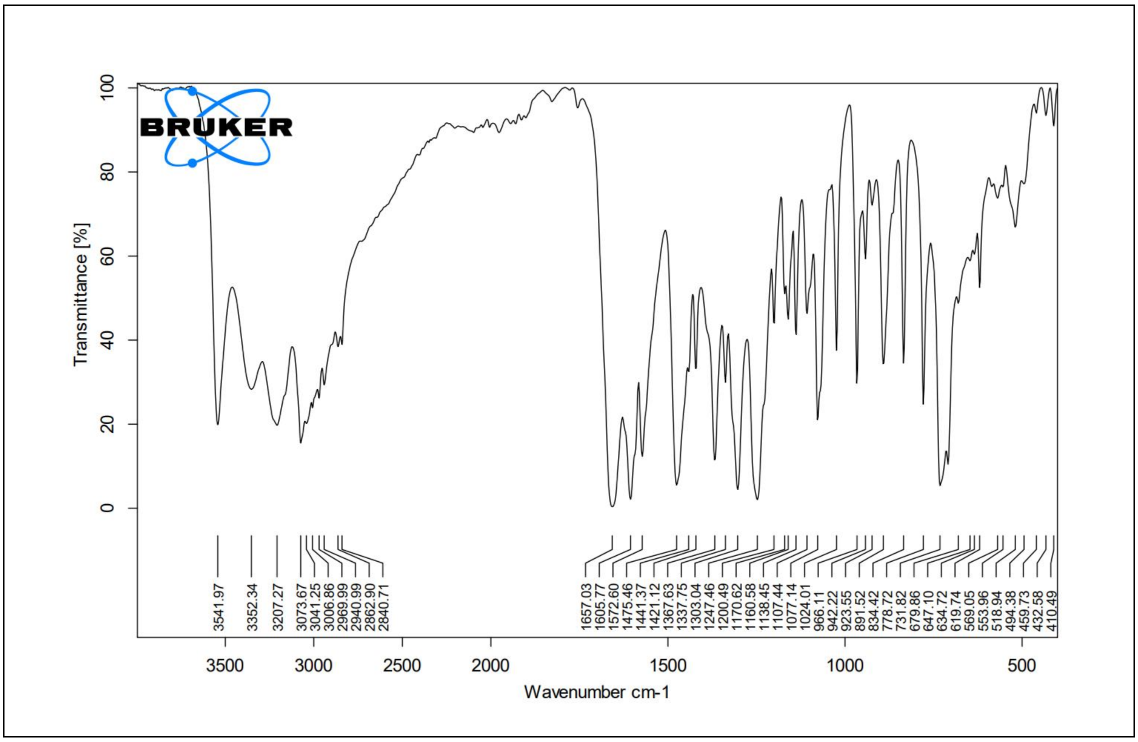

Fig. 19. FTIR spectrum of complexes **7**.

3.4 Electronic spectra

Electronic absorption spectra of complexes **1-7** were recorded in a DMSO solution (3.0×10^{-3} M). UV-visible spectra are shown in Fig. 20 and electronic spectroscopic data for the complexes in DMSO solution are summarized. Complexes **1**, **2** and **4** show visible band in the range 765-810 cm^{-1} along with UV band (Table 2) [77].

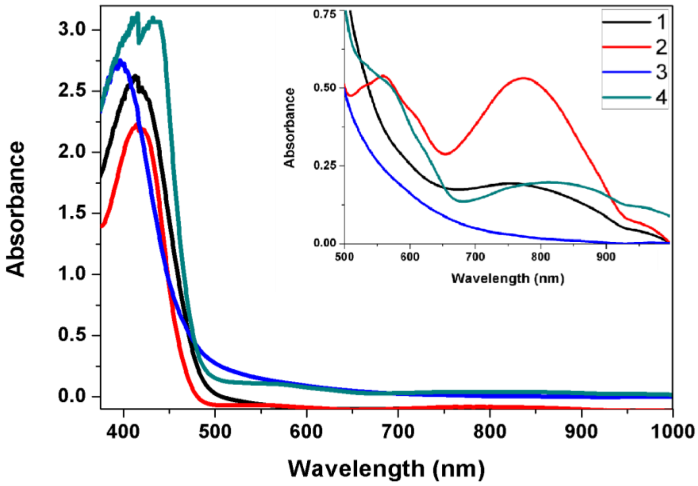

Fig. 20. UV-Visible spectra of vanadium(IV/V) complexes **1-4** in DMSO solution. Inset 3.0 x 10^{-3} M in DMSO solution.

A strong band around 411 nm in complexes **1**, **2**, and **4** correspond to the ligand to metal charge transfer (LMCT) transitions originating from the p_x orbital of phenolate oxygen to the empty d orbital [PhO→V_{dx}] of the vanadium(IV) center [78-80]. Complex **3** only consists of an intense band at 390 nm, assigned to LMCT transition. The d-d band is not seen in **3** indicating V(V) having a $3d^0$ electronic configuration [81]. Comparing the electronic spectrum of this complex with other oxidovanadium **1**, **2** and **4** complexes shows that the LMCT band is a shift to higher energy. It can attribute to the electron-donor of the ligands on stabilizing the lowest unoccupied molecular orbitals. All other complexes show a d-d band corresponding to high valent V(IV). Scan range of the d-d band was considered between 500-1000 nm and the maximum peak was observed in the range of 765-810 nm as shown in the inset (Fig. 20).

Table 2 UV-Vis data of complexes **1-4.**

Complex	**λ_{max}, nm**	
	d-d band	**LMCT**
1	765 (0.36)	410
2	770 (0.97)	412
3	-	390
4	810 (0.38)	410, 440

Electronic spectra of complexes **5-7** were also recorded in DMSO solution and shown in Fig. 21. In the 300-500 nm region, two absorption bands are present in all complexes. The low energy bands of **5** at 410 nm, 379 nm of **6** and **7** at 438 nm may be assigned as a ligand to metal charge transfer (LMCT) transition, arising from the p_π-orbital of the phenolate oxygen to the empty *d* orbital [PhO→V_{dx}] of the vanadium [82-85]. Although the LMCT band of **6** is possibly hidden under the low energy tail of the Schiff base to vanadium charge transfer band. In these complexes more intense bands at ~ 336 nm in **5**, 323 nm in **6** and 340 nm in **7** are expected for intra ligand charge transfer band [85, 86]. The electronic spectral data of these vanadium(V) complexes (**5-7**) are collected in Table 3.

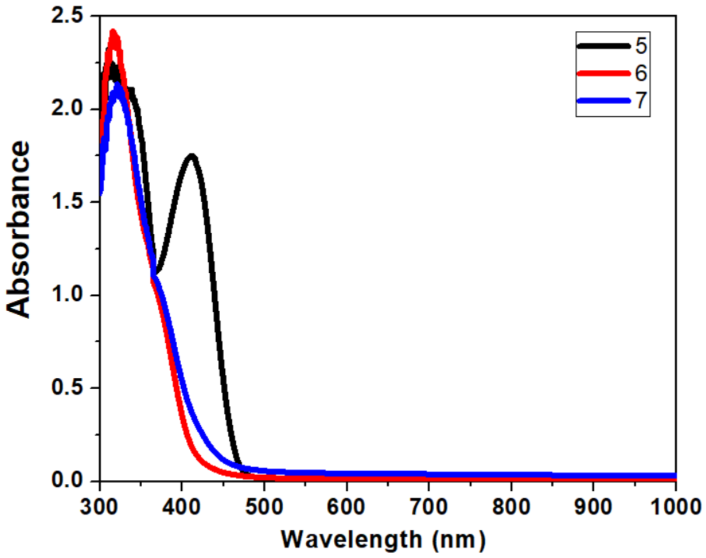

Fig. 21. UV-Visible spectra of vanadium(IV/V) complexes **5-7** in DMSO solution.

Table 3 UV-Vis data of complexes **5-7.**

Complex	**λ_{max}, nm**	
	Intra ligand band	**LMCT**
5	336	410
6	340	379
7	340	438

3.5 Molecular structure of ligand HL^2

The molecular structure of HL^2 is shown in Fig. 22. Crystal data and structure refinements are listed in Table 4. Some important bond lengths and angles are given in Table 4. The HL^2 has three donors (NNO) sites, *viz.*, phenolic oxygen (O1), imine nitrogen (N2) and pyridine nitrogen (N3). The phenol C1-O1(-H) bond of 1.32(2) Å is within the limit of a C-O single bond (Table 5) [87]. The bromine and pyridine atoms in the Schiff base are involved in the intramolecular hydrogen bondings. The hydrogen bond parameters are given in Table 6 with the symmetry code. The packing of the Schiff base is associated with the hydrogen bondings (Fig. 23).

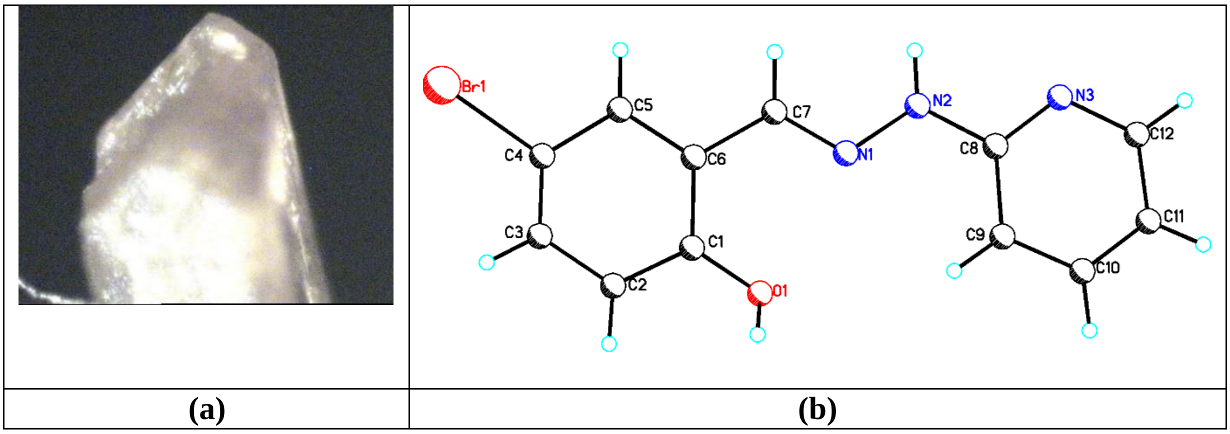

(a) (b)

Fig. 22(a) Crystal image and **(b)** ORTEP view of the ligand **HL²**.

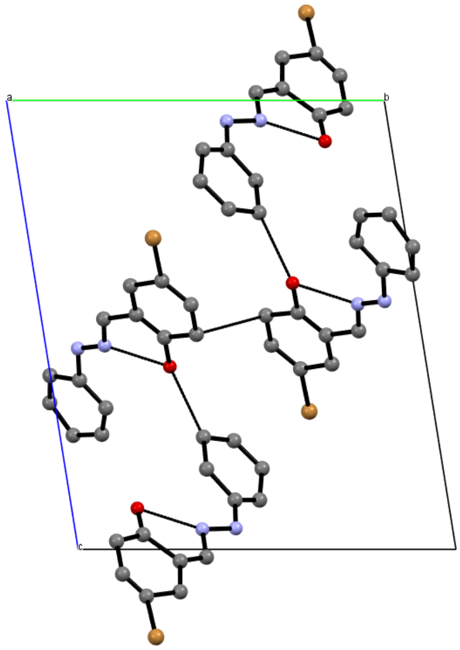

Fig. 23. Crystal packing diagram along a-axis of **HL²**.

Table 4 Crystal data and structure refinement for **HL²**.

Identification code	**HL²**
Empirical formula	$C_{12}H_{10}BrN_3O$
Formula weight	292.14
Temperature(K)	100(2)
Wavelength(Å)	0.71073
Crystal system	Monoclinic
Space group	C 2/c
Unit cell dimensions	a = 26.98(2) Å α = 90° b = 5.491(4) Å β = 124.36°

	c = 19.365(16) Å γ = 90°
Volume (Å^3)	2369(3)
Z	8
Density (calculated)	1.638 Mg/m^3
Absorption coefficient	3.457 mm^{-1}
F(000)	1168
Theta range for data collection (°)	2.548 to 27.907
Index ranges	-34<=h<=34, -6<=k<=7, -24<=l<=25
Reflections collected	10532
Independent reflections	2573 [R(int) = 0.2142]
Completeness to theta = 25.242°	99.3 %
Absorption correction	None
Refinement method	Full-matrix least-squares on F^2
Data / restraints / parameters	2573 / 0 / 155
Goodness-of-fit on F^2	1.168
Final R indices [I>2sigma(I)]	R1 = 0.1957, wR2 = 0.4272
R indices (all data)	R1 = 0.2751, wR2 = 0.4622
Extinction coefficient	n/a
Largest diff. peak and hole (Å^{-3})	3.572 and -2.060 e

Table 5 Bond lengths [Å] and angles [°] for **HL^2**.

Bond lengths			
Br(1)-C(4)	1.95(2)	C(1)-C(2)	1.41(3)
O(1)-C(1)	1.32(2)	C(1)-C(6)	1.46(3)
O(1)-H(1)	0.8400	C(2)-C(3)	1.42(3)
N(1)-N(2)	1.37(2)	C(2)-H(2A)	0.9500
N(2)-C(8)	1.41(3)	C(3)-C(4)	1.28(3)
N(2)-H(2B)	0.8800	C(3)-H(3A)	0.9500
N(3)-C(8)	1.32(3)	C(8)-C(9)	1.45(4)
N(3)-C(12)	1.37(3	C(12)-C(11)	1.40(3)
Bond angles			
C(1)-O(1)-H(1)	109.5	C(1)-C(2)-C(3)	120(2)
C(7)-N(1)-N(2)	116(2)	C(1)-C(2)-H(2A)	120.2
N(1)-N(2)-C(8)	119(2)	C(3)-C(2)-H(2A)	120.2
N(1)-N(2)-H(2B)	120.5	C(5)-C(6)-C(1)	121.5(18)
C(8)-N(2)-H(2B)	120.5	C(5)-C(6)-C(7)	118(2)
C(8)-N(3)-C(12)	117(2)	C(1)-C(6)-C(7)	120.8(18)
O(1)-C(1)-C(2)	120(2)	N(3)-C(8)-N(2)	116(2)
O(1)-C(1)-C(6)	123.0(18)	N(3)-C(8)-C(9)	123.4(19)
C(2)-C(1)-C(6)	117.1(19)	N(2)-C(8)-C(9)	121(2)

Table 6 Hydrogen bonds for **HL^2**.

D-H...A	d(D-H)	d(H...A)	d(D...A)	<(DHA)	Symmetry
N(2)-H(2B)...N(3)#1	0.88	2.29	3.07(3)	147.9	#1 -x+1/2,-y+5/2,-z+1
C(5)-H(5A)...Br(1)#2	0.95	3.03	3.84(2)	144.5	#2 -x+1/2,y+1/2,-z+1/2

3.6 Molecular structure of complex 3

The molecular structure of complex **3**, the vanadium(V) complex is shown in Fig. 24 and the crystallographic data are given in Table 7. Relevant bond parameters are given in Table 8. In the molecular structure, the vanadium ion has an N_4O_2-donor environment, arranged in a distorted octahedral geometry. One of the imidazole rings is disordered over two sets of sites in a 0.55(1):0.45(1) ratio. It's not disordered over a two-fold rotation axis but is disordered over two positions because the S atom is positioned at the inversion center. Half solvent molecule (half water molecule) was also observed. The solvent molecule lies on a two-fold axis. In structure refinement, an oxygen atom of water solvent has only 50% occupancy. Atom O711 of water solvent is further disordered to another position O712 with refinable occupancy, constrained to add up to 0.5. Water hydrogen could not be located due to disorder. The equatorial plane consists of N1, N6, N211 and O2 atoms. While the oxido oxygen atom O1 and the nitrogen atom of azomethine N13 of L^- occupies the axial positions. In the transposition to the terminal oxido group is the N13 atom of the azomethine group with the bond length from vanadium atom of 2.231 A^0 that is significantly longer than equatorial contacts V-O/N (1.921-2.132 A^0) as a consequence of trans effect [88-90]. Moreover, the V1-O1 bond length is 1.594 A^0 due to the double bond in between V and O atoms [91]. These bond lengths are in the range found in other similar vanadium(v) complexes [92-95]. The geometry of vanadium centre is distorted from an octahedral and can illustrated as elongated octahedral which is clearly reflected from the various bond lengths and angles around metal centre. The disposition of the HL^2 deviates from the perpendicular as seen by the reduced value of trans angles N1-V1-N211 = 170° and O2-VI-N6=156°. HL^2 in these complex forms one six-membered and one five-membered rings. The five-membered metal chelate ring comprising V1, N6, C11, N12 and N13 atoms adopts a envelop conformation on C11 atom. However, the six-membered chelate ring comprising V1, O2, C20, C15, C14 and N13 is planar. The space-filling model of the complex is shown of Fig. 25.

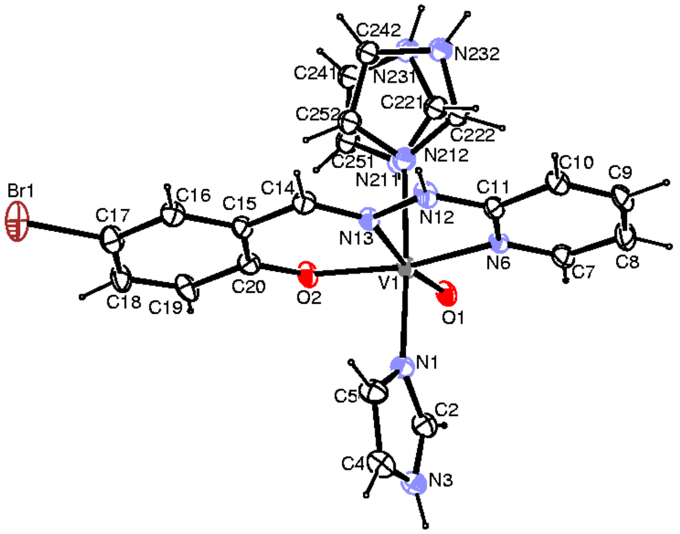

Fig. 24. Molecular structure of complex **3** (for clarity the solvent molecules have not been shown**).**

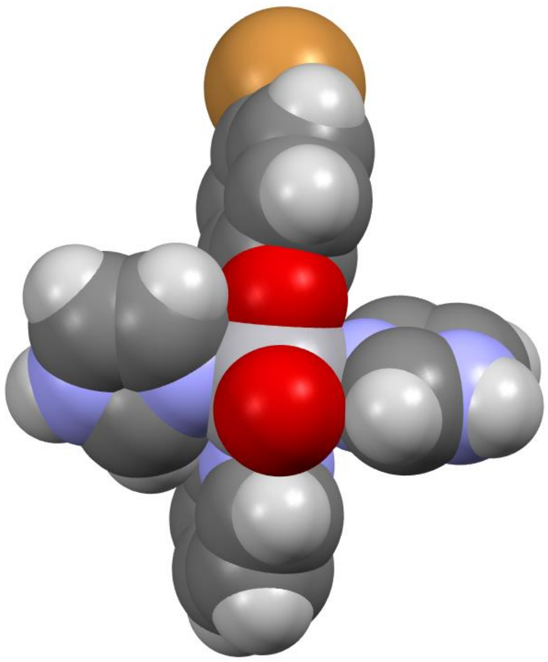

Fig. 25. Space-filling models of complex **3**.

Table 7 Crystal data and structure refinement for complex **3**.

Empirical formula	**$C_{18}H_{17}BrN_7O_7SV$**
Formula weight	606.
Temperature (K)	293(2)
Crystal system	monoclinic

Space group	$P2_1/c$
a (Å)	8.2858(9)
b(Å)	16.6032(14)
c(Å)	16.5490(15)
α(°)	90.00
β(°)	95.784(9)
γ(°)	90.00
Volume (Å^3)	2265.1(4)
Z	2
ρ_{calc}g/cm^3	1.617
M mm^{-1}	2.290
F(000)	1108.0
Crystal size (mm^3)	0.3 × 0.2 × 0.2
Radiation	MoKα ($\lambda = 0.71073$)
2Θ range for data collection (°)	6.64 to 52
Index ranges	$-10 \leq h \leq 10$, $-20 \leq k \leq 19$, $-20 \leq l \leq 20$
Reflections collected	21809
Independent reflections	4444 [$R_{int} = 0.1185$, R_{sigma} = N/A]
Data/restraints/parameters	4444/350/367
Goodness-of-fit on F^2	1.025
Final R indexes [I>=2σ (I)]	$R_1 = 0.0856$, $wR_2 = 0.2032$
Final R indexes [all data]	$R_1 = 0.1606$, $wR_2 = 0.2596$
Largest diff. peak/hole (e Å^{-3})	0.71/-0.86

Table 8 Molecular dimensions (bond lengths in Å and angles in °) about oxidovanadium(V) in complex **3**.

Bond Length			
N211-V1	2.132(16)	N1-V1	2.098(7)
N6-V1	2.098(5)	N13-V1	2.231
O1-V1	1.594(5)	O2-V1	1.923(5)
Bond Angles			
O1-V1-O2	108.7(2)	O1-V1-N13	168.3(2)
O1-V1-N6	94.8(2)	O2-V1-N13	82.8(2)
O1-V1-N6	156.5(2)	N6-V1-N13	73.8(2)
O1-V1-N1	94.4(3)	N1-V1-N13	88.3(2)
O2-V1-N1	88.4(2)	N211-V1-N13	82.4(5)
N6-V1-N1	90.0(2)	O1-V1-N211	95.3(5)
O2-V1-N211	87.6(4)	N6-V1-N211	90.2(4)
N1-V1-N211	170.2(5)		

The molecular structure of **3** is stabilized by intermolecular H-bonding and $\mathrm{C-H\cdots\pi}$ interactions linking, the neighbouring complex molecules into the two-dimensional infinite network. In the asymmetric unit, two units of vanadium complexes are linked by intermolecular H-bonds, Where the $\mathrm{C9\cdots H9\cdots O1}$ and $\mathrm{C9\cdots H9\cdots O2}$ interactions (involving the C9 of the phenyl ring of HL) constitute a pair of bifurcated donor bonds generating a ring of graph set$R_1^2(4)$ [96, 97] (Fig. 26). Also of intermolecular H-bonding, $\mathrm{C-H\cdots\pi}$ interactions are also responsible for assembling the adjacent asymmetric units. The molecular structural data available for the complex revealed that found $\mathrm{C-H\cdots\pi}$ interactions lead to one-dimensional aggregation. The first categories of these features are $\mathrm{C-H\cdots\pi}$ (aryl) interactions with distances range 2.955 Å and 3.587Å and the second category of $\mathrm{C-H\cdots\pi}$(metal chelate ring) with the distances 2.696 Å and 3.176 Å. The first category of $\mathrm{C-H\cdots\pi}$ (aryl) interactions occur two $\mathrm{C-H}$ of bound imidazole and a ring (aryl) of imidazole of second complex molecule. The second category of $\mathrm{C-H\cdots\pi}$ (metal chelates) interaction was seen in between $\mathrm{C-H}$ of imidazole of complex and metal chelate of same complex. Thus, the majority of structures featuring H-bonding and $\mathrm{C-H\cdots\pi}$ (aryl and metal chelate) interactions utilize these synthons to assemble molecules into 1D supramolecular polymeric chains (Fig. 27). The packing diagram of complex 3 is shown in Fig. 28.

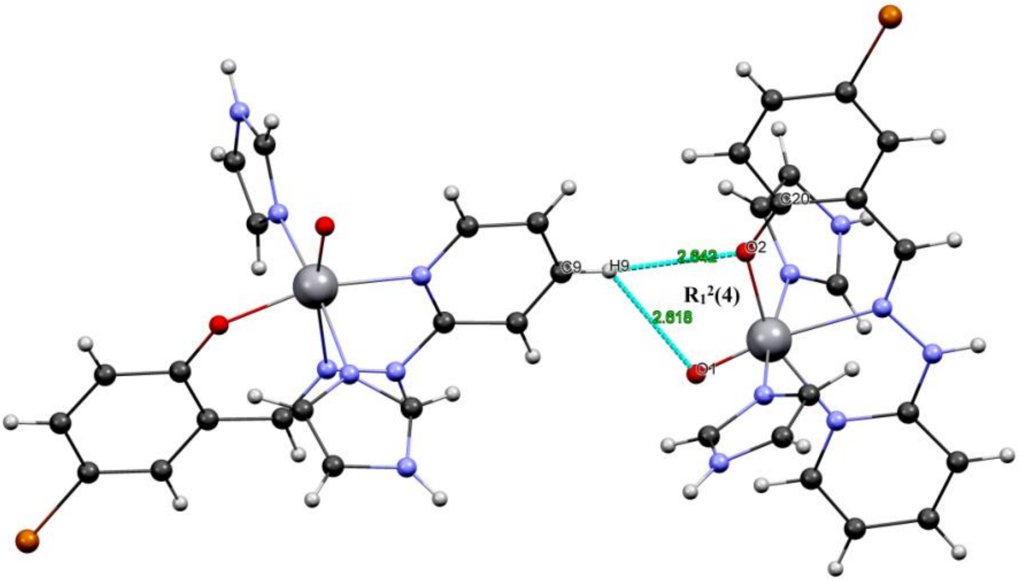

Fig. 26. A perspective view of complex **3** showing two asymmetric units involving intermolecular H-bondings.

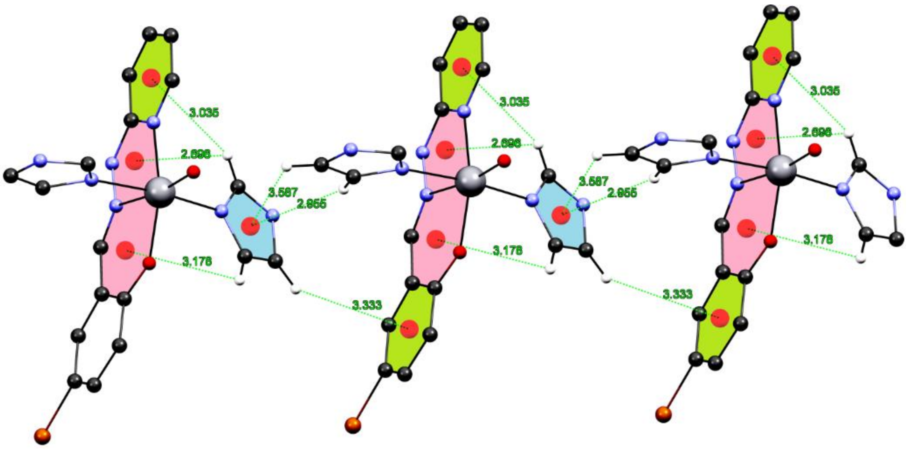

Fig. 27. C − H ⋯ π (aryl and metal chelate) interactions generating a 1D polymeric chain of complex **3**.

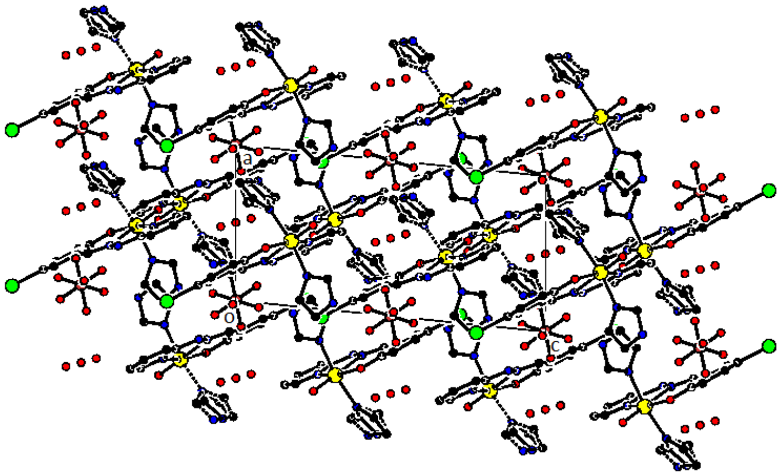

Fig. 28. The packing arrangement of molecules viewed down the b-axis in complex **3**.

3.7 Molecular structures of complexes 5-7

The molecular structures of complexes **5**, **6** and **7** have been solved using single-crystal X-ray analysis. The X-ray analysis displayed that complex **5** is crystallized in the Pc2a1 space group as a racemate. The molecular geometry of **5** in crystals with the atom labelling scheme is presented in Fig. 29. Additional crystal data along with more information about the X-ray structure analyses are given in Table 9. Significant bond distances (Å) and bond angles (º) are summarized in Table 10. This complex consists of a dimer with two independents asymmetric (molecules) units. The monoanionic tridentate ligand (HL^3) spans the meridional sites through pyridine and imino nitrogen’s and phenolate oxygen the basal plane and two dioxido groups at the apical position forming a five coordinated geometry (Fig.

30 coordination sphere). The distortion of a square pyramidal geometry ascertained by the structural parameter (τ_5) which is determined using (β-α)/60, where β is the larger and α is the smaller trans angles [98]. The vanadium coordination sphere is a slightly distorted square pyramid, as τ_5 = 0.15 (0 for square pyramid and1 for an ideal trigonal bipyramid). The V-O (phenolate), the pyridine (V-N) and the V-N (imine) (2.166) bond lengths are comparable with similar to those bond lengths in the similar reported dioxidovanadium complexes [99-102]. With respect to the O1V vector, the complex is nearly C_4 symmetric, as indicated in space filled model and coordination sphere Fig. 31.

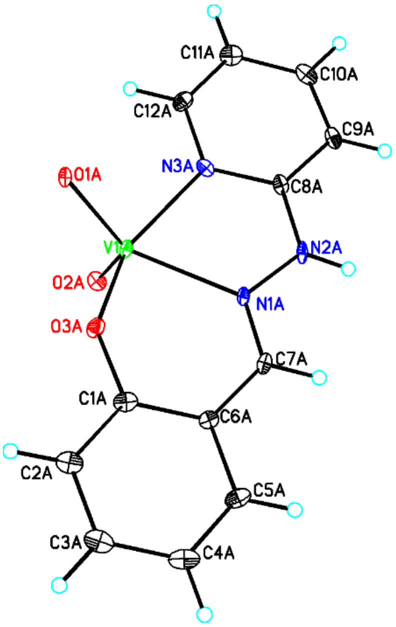

Fig. 29. Crystal structure of complex **5**.

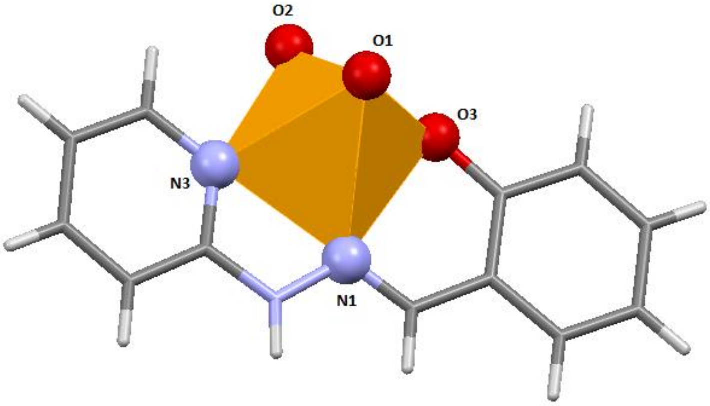

Fig. 30. The coordination sphere of complex **5**.

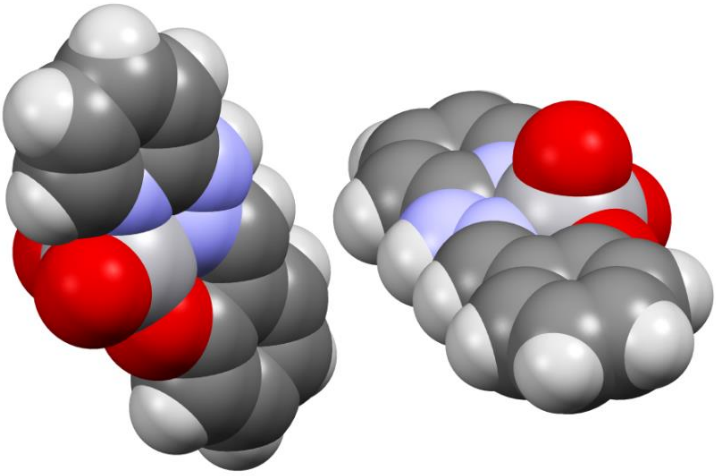

Fig. 31. Space filling models of complex **5**.

Table 9 Crystal data and structure refinement of complexes **5**, **6** and **7**.

	5	**6**	**7**
Empirical formula	$C_{12}H_{10}N_3O_3V$	$C_{13}H_{11}N_2O_4V$	$C_{13}H_{15}N_4O_5V$
Formula weight	295.17	310.18	358.23
Temperature (K)	100(2)	100(2)	123(2) K
Wavelength (Å)	0.71073	0.71073	0.71073 Å
Crystal system	Orthorhombic	Monoclinic	Monoclinic
Space group	Pca21	P 21/n	C 2/c
a **(Å)**	13.2994(9)	9.3926(3)	18.8665(4)
b **(Å)**	9.9406(7)	11.2053(3)	7.4911(2)
c **(Å)**	17.8292(12)	12.0820(4)	21.9511(6)
α **(°)**	90	90	90
β **(°)**	90	104.0010(10)	101.734(2)
γ **(°)**	90	90	90
Volume (Å^3)	2357.1(3)	1233.82(7)	3037.53(13)
Z	8	4	8
Density (calculated) (Mg/m^3)	1.664	1.670	1.567
Absorption coefficient (mm^{-1})	0.849	0.819	0.685
***F*(000)**	1200	632	1472
Theta range for data collection (°)	2.558 to 26.372	2.881 to 35.049	2.205 to 30.645
Index ranges	-16<=h<=16, -12<=k<=12, -22<=l<=22	-14<=h<=14, -17<=k<=17, -19<=l<=19	-24<=h<=26, -10<=k<=10, 30<=l<=30
Reflections collected	27496	23074	35284

Independent reflections	4828 [R(int) = 0.1450]	4879 [R(int) = 0.0249]	4537 [R(int) = 0.0718]
Completeness to theta = 25.242°	99.9 %	99.9 %	99.4 %
Absorption correction	Semi-empirical from equivalents	None	Semi-empirical from equivalents
Refinement method	Full-matrix least-squares on F^2	Full-matrix least-squares on F^2	Full-matrix least-squares on F^2
Data / restraints / parameters	4828 / 281 / 350	4879 / 0 / 186	4537 / 0 / 218
Goodness-of-fit on F^2	1.022	1.032	1.063
Final R indices [I >2sigma(I)]	R1 = 0.0590, wR2 = 0.1071	R1 = 0.0300, wR2 = 0.0735	R1 = 0.0352, wR2 = 0.0957
***R* indices (all data)**	R1 = 0.1095, wR2 = 0.1234	R1 = 0.0405, wR2 = 0.0802	R1 = 0.0410, wR2 = 0.0988
Extinction coefficient	n/a	n/a	n/a
Largest diff. peak and hole (e. Å^{-3})	0.466 and -0.640	0.553 and -0.436	0.681 and -0.585

Table 10 Bond lengths [Å] and angles [°] of complexes **5**, **6** and **7**.

5					
Bond length					
	XRD	**DFT**		**XRD**	**DFT**
V(1)-O(2A)	1.612(6)	1.612	V(1)-N(3A)	2.101(8)	2.100
V(1)-O(1A)	1.637(6)	1.630	V(1)-N(1A)	2.166(6)	2.169
V(1)-O(3A)	1.878(7)	1.871			
Bond angle					
O(2A)-V(1)-O(1A)	108.1(3)	108.10	O(3A)-V(1)-N(3A)	150.4(3)	150.40
O(2A)-V(1)-O(3A)	105.6(3)	105.62	O(2A)-V(1)-N(1A)	108.8(3)	108.84
O(1A)-V(1)-O(3A)	98.4(3)	98.43	O(1A)-V(1)-N(1A)	141.4(3)	141.45
O(2A)-V(1)-N(3A)	98.2(3)	98.25	O(3A)-V(1)-N(1A)	82.2(3)	82.22
O(1A)-V(1)-N(3A)	90.5(3)	90.55	N(3A)-V(1)-N(1A)	73.5(3)	73.55
6					
Bond length					
V-O(2)	1.6148(9)	1.6149	V-O(4)	2.0015(9)	2.0015
V-O(1)	1.6517(9)	1.6513	V-N(1)	2.1695(9)	2.1699
V-O(3)	1.8806(9)	1.8809			
Bond angle					
O(2)-V-O(1)	108.49(5)	108.40	O(3)-V-O(4)	145.70(4)	145.70
O(2)-V-O(3)	106.10(5)	106.10	O(2)-V-N(1)	102.86(4)	102.80

O(1)-V-O(3)	98.43(4)	98.41	O(1)-V-N(1)	147.73(4)	147.73
O(2)-V-O(4)	100.57(4)	100.58	O(3)-V-N(1)	79.70(4)	79.70
O(1)-V-O(4)	93.07(4)	93.07	O(4)-V-N(1)	73.58(3)	73.60
7					
Bond length					
V-O(5)	1.6163(11)	1.6165	V-O(3)	1.9639(9)	1.9638
V-O(4)	1.6467(11)	1.6469	V-N(1)	2.1550(11)	2.1554
V-O(1)	1.9071(9)	1.9078			
Bond angle					
O(5)-V-O(4)	110.67(7)	110.68	O(1)-V-O(3)	147.12(4)	147.11
O(5)-V-O(1)	104.11(5)	104.14	O(5)-V-N(1)	105.02(5)	105.08
O(4)-V-O(1)	95.84(5)	95.84	O(4)-V-N(1)	143.69(6)	143.69
O(5)-V-O(3)	102.68(5)	102.68	O(1)-V-N(1)	81.51(4)	81.56
O(4)-V-O(3)	92.21(5)	92.25	O(3)-V-N(1)	73.37(4)	73.38

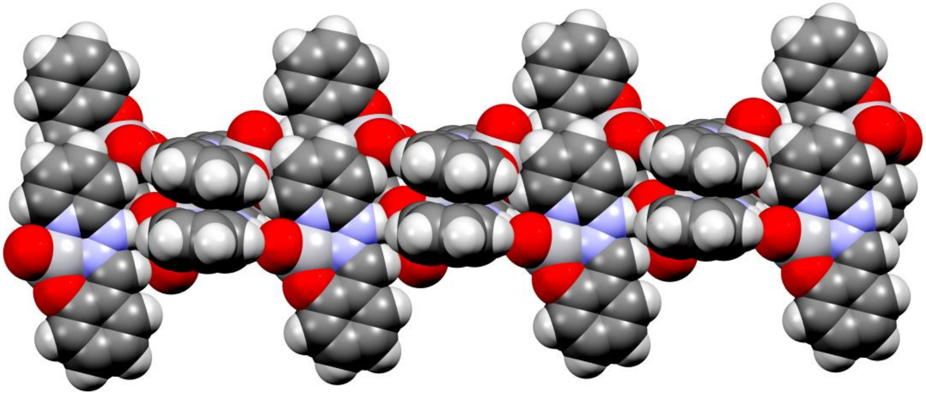

Fig. 33. Space filling packing along a-axis in complex **5**.

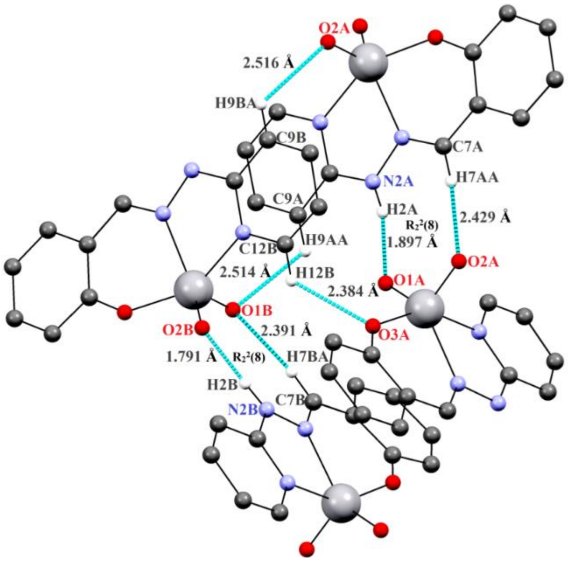

Fig. 34. Hydrogen bondings and supramolecular homosynthones $R_2^2(8)$ in complex **5**.

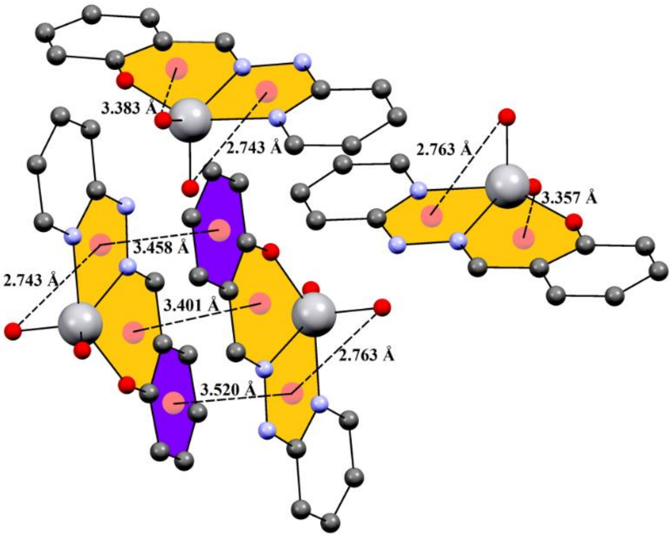

Fig. 35. lp···π and π···π (metal chelate-metal chelate and aryl-metal chelate) interactions in complex **5**.

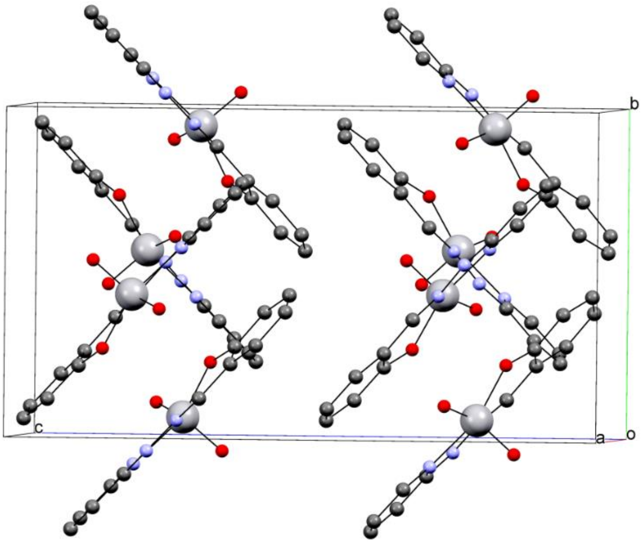

Fig. 36. Crystal packing diagram along a-axis of complex **5**.

In Fig. 33. solid state structure of **5** is shown. It is noticed that presence of self-assembled dimers that are disposed of in two different orientations forming 2D layers. The sophisticated formation of interactions that are well-established in this dimer have been analysed and dictate its formation. Hydrogen bond interactions are shown in Table 11. Interestingly complex **5** internally stabilized by several intermolecular C-H···O/ N-H···O hydrogen bonds between the C (azo carbon)/ N (imino nitrogen) of HL as H-donors and the O atoms of oxido(VO_2^+) as acceptor. In the crystal lattice, a set of carbon and nitrogen atoms are intermolecularly hydrogen-bonded to oxido oxygen atoms of the neighbouring molecule by a pair of N2H2A···O1A (d_{D-A} = ~ 1.90Å) and C7A-H7A···O2A (d_{D-A} = ~ 2.93Å) hydrogen bonds leading to the formation of dimers with $R^2_2(8)$ graph set ring motif (cyclic dimers) [108]. One more $R^2_2(8)$ graph set ring motif is formed by a similar fashion of N-H···O /C-H···O type of intermolecular hydrogen bondings but d_{D-A} are different (Fig. 34). Furthermore, both chelate rings are stacked in an antiparallel fashion, also devoting to a dimer formation. The dimerization energy is large and negative (ΔE1= -15.6 kcal/ mol) due to supplying of both types of interactions. In this dimer an oxygen atom of VO_2^+ moiety forms a bifurcated H-bond with the proton of an azo moiety of HL^3 and an aromatic hydrogen atom. The interaction energy (ΔE1= -15.6 kcal/ mol), thus authenticating the strong hydrogen bonding interaction. The anti-parallel Cg-Cg (π···π) stacking interactions between the chelates is also indicated (Fig. 34).

Dimer units are linked by neighbouring dimer units by intermolecular C9B-H9B-O2A (d_{D-A}= ~ 3.15Å) and C9A-H9A-O1B (d_{D-A} = ~ 3.10 Å) hydrogen bondings. The cohesion of crystal packing in this complex is further secured by lone pair (lp)···π, Cg-Cg (π···π) (aryl-metal chelate) and π···π (metal chelate-metal chelate) weak contacts (Fig. 35). Oxido O atoms of VO_2^+ moiety forms a unique intramolecular ln···π ($d_{lp\cdots\pi}$ = 2.74 Å and 3.36 Å) contact are formed by the O atoms of VO_2^+ moiety with the same molecule's five-membered chelate rings and thus molecule is internally stablished. In the same way, two molecules are stablished by two types of intermolecular Cg-Cg (π···π) stacking interactions. The π···π (metal chelate - metal chelate) distance (d_{Cg-Cg}) is 3.40 Å. Similarly, aryl moiety of HL of one molecule sand metal chelate ring of neighbouring molecule is interconnected by a set of (π···π) (aryl-metal chelate rings) contacts with d_{Cg-Cg}= 3.52Å and 3.46 Å. Supramolecular architecture is therefore composed by additional weak hydrogen bonds, ln···π and Cg-Cg (π···π) interactions. View of packing diagrams along with a-axis is shown in Fig. 36.

Complex **6** crystallizes the P21/n space group with a monoclinic crystal system. In complex **6**, again vanadium coordination sphere is a distorted square pyramid as estimated by the structural parameter τ_5 = 0.03 which is very close to an ideal square pyramidal geometry (Fig. 37). For this complex coordinating atoms of tridentate (HL^4) ligand are natphthalate O, imine N and ketonic O atoms at the basal plane and two dioxido oxygen atoms one basal plane other in the apical position forming a pentacoordinated geometry around the metal centre. The arrangement of the tridentate Schiff base around the vanadium centre for **6** are similar to those of **5**, with the vanadium(V) centre also maintain a square pyramidal geometry. The V-N (imine) bond length is in the range observed to similar pentacoordinated Schiff base complexes [103, 104]. The V-N (imine) bond length is also comparable to complex **5**. In this complex, the structural parameter $\boldsymbol{\tau}_5$ (0.03) is noticeably smaller than complex **5** (0.15). Such an unexpected difference in τ_5 values in these complexes is due to the larger α value (147.73°) in complex **6** in comparison to α value (141.4°) in complex **5**. The larger angle α (O1VN1) in **5** causes a small tilt of a VO_2^+ group. The distortion in VO_2^+ moiety perhaps happens due to the involvement of only one oxido oxygen atom of VO_2^+ moiety (1.6517(9)) *vs.* (1.6148(9) Å) which is the larger difference than V = O distances (1.637(6) *vs.* 1.612(6) Å) in **5**. Concerning the 01V vector, the complex is almost c_4 symmetric, as indicated in space filled model and coordination sphere Fig. 38. The same conclusion is drawn by $\boldsymbol{\tau}_5$(= 0.03) value. The deviations of V(V) center from the same plane in the directions of the terminal oxygen atom O (2/3), is ~0.489 Å. The V(1)-O2(A) and V(1)-O(1A) bond distances ~1.6 Å. This kind of V-O short distances are typical V=O double bonds [105]. The V=O bond lengths are comparable with those found in other V(V) complexes [106,107].

The crystal packing of **6** exhibited the formation of 1D supramolecular chain build through intermolecular N2H2···O1 ($d_{D\text{-}A}$= ~2.64 Å) hydrogen bond between the N- atom of NH (imino) moiety as H-donor and the O-atom of the oxido (VO_2^+) group as H-acceptor (Fig. 39). The <DHA of this intermolecular H-bond is 173°. Similarly, C2H2 of aryl moiety of HL acts as an H-bond donor to O4 (carbonyl group) of adjacent molecule forming an intermolecular C2H2A···O4 H-bond with $d_{D\cdots A}$ = ~3.23 Å and <DHA = 131.9°. This distance remains into the range of distances reported for the C-H···O hydrogen bonds. Stabilization of crystal structure is further controlled by CH···π (aryl and metal chelates) and ln···π (metal chelate) intramolecular interactions.

In this molecule the unprecedented formation of lp···π (metal chelate) intramolecular interactions stabilises the molecule. The O atom of VO_2^+ moiety of complex donates the lone pair of electrons to five membered chelate ring by forming lp···π (3.076Å) intramolecular interactions. This molecule is also stablished by various CH···π (aryl and metal chelate) intramolecular interactions (Fig. 40) No significant Cg-Cg (π···π) stacking interactions have been observed. The packing diagram along the a-axis and space filled packing along c-axis is shown in Fig. 41 and 42.

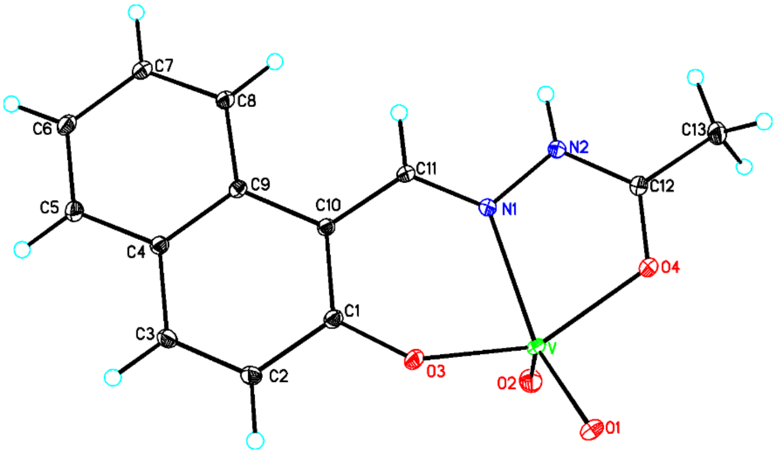

Fig. 37. Crystal structure of complex **6**.

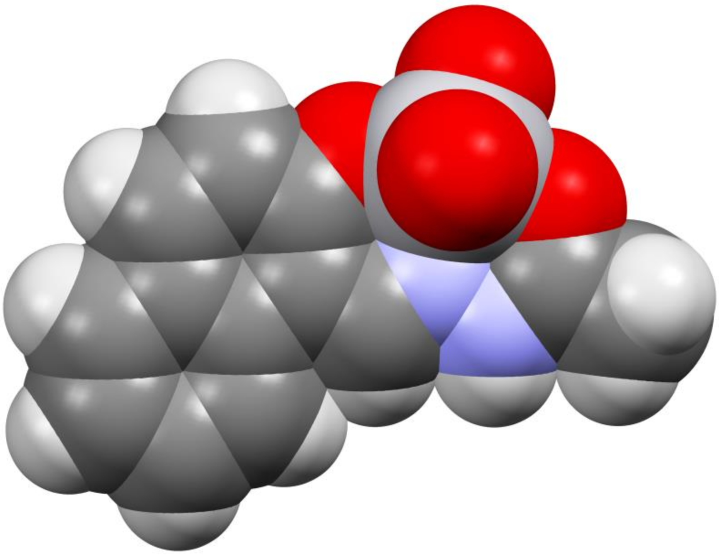

Fig. 38. Space-filling model of complex **6**.

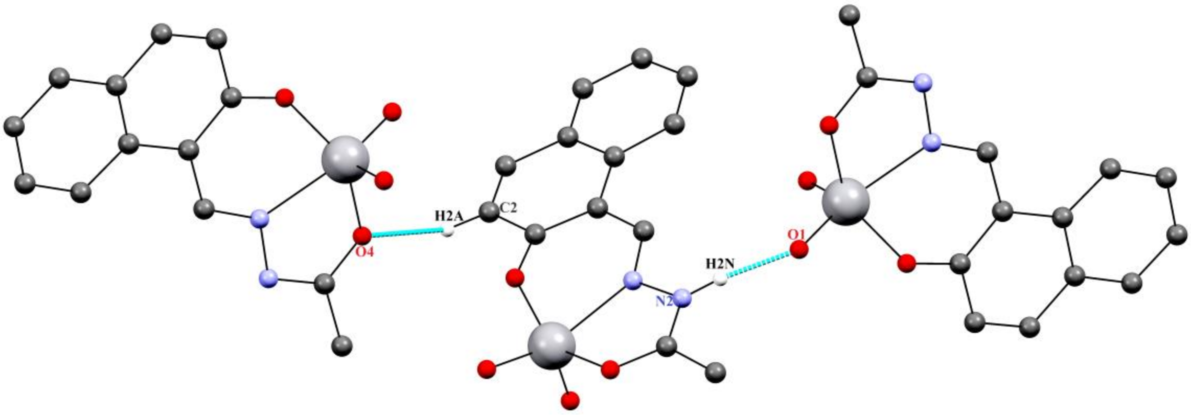

Fig. 39. Intermolecular hydrogen bonding interaction in complex **6**.

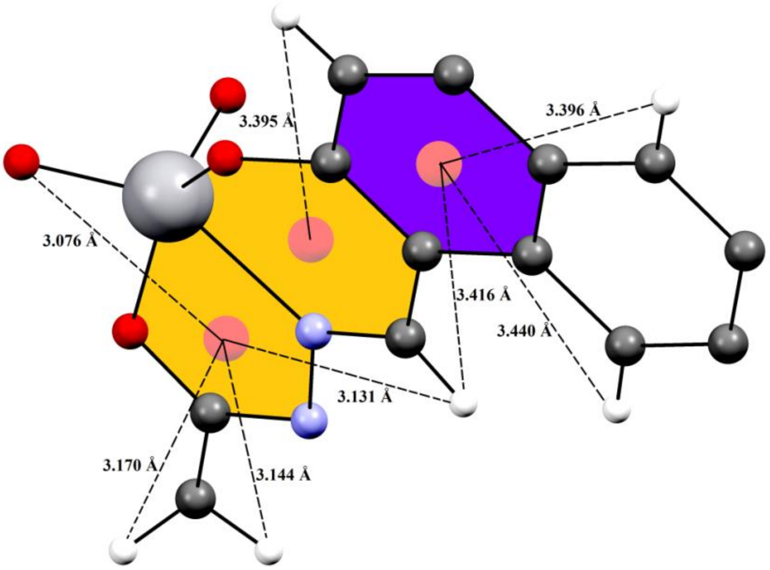

Fig. 40. lp···π and C-H···π(aryl and metal chelate) interaction in complex **6**.

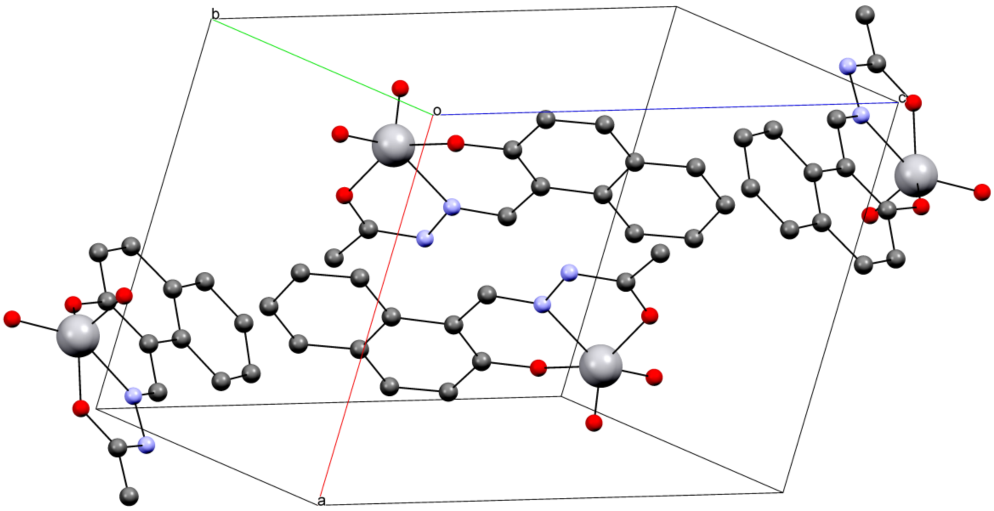

Fig. 41. Crystal packing of complex **6** along a-axis.

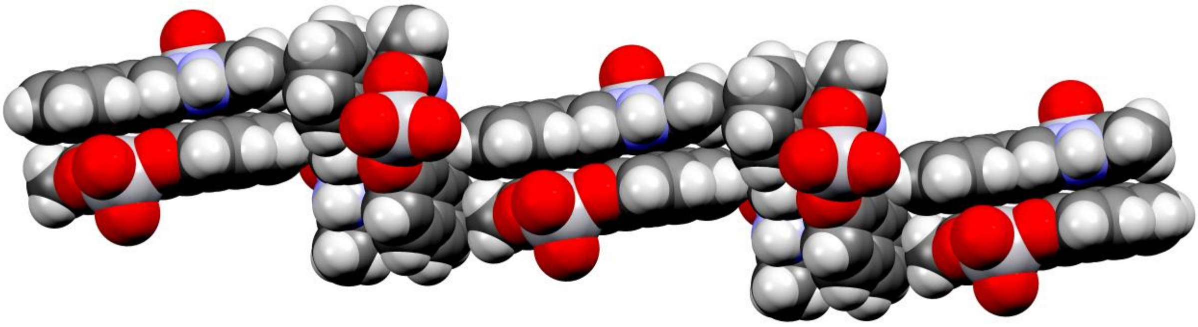

Fig. 42. Space filling packing along c-axis complex **6**.

Table 11 Hydrogen bonds of complexes **5**, **6** and **7** [Å and °].

D-H...A	d(D-H)	d(H...A)	d(D...A)	<(DHA)	Symmetry transformations
5					
N(2A)-H(2A)...O(1A)#1	0.85(8)	1.90(9)	2.727(9)	166(8)	#1 x+1/2,-y+1,z
C(7A)-H(7AA)...O(2A)#1	0.95	2.43	3.340(11)	160.7	
C(9A)-H(9AA)...O(1B)#2	0.95	2.51	3.106(11)	120.4	
C(12A)-H(12A)...O(3B)#3	0.95	2.49	3.232(11)	135.2	#3 x-1,y,z
N(2B)-H(2B)...O(2B)#2	0.92(9)	1.80(9)	2.704(9)	169(9)	#2 x-1/2,-y,z
C(7B)-H(7BA)...O(1B)#2	0.95	2.39	3.311(11)	163.0	
C(9B)-H(9BA)...O(2A)#4	0.95	2.52	3.152(11)	124.4	#4 x+1/2,-y,z
C(12B)-H(12B)...O(3A)#5	0.95	2.38	3.085(11)	130.3	#5 x+1,y-1,z
6					
N(2)-H(2N)...O(1)#1	0.89(2)	1.75(2)	2.6374(13)	173(2)	#1 x+1/2,y+3/2,z+1/2
C(2)-H(2A)...O(4)#2	0.95	2.52	3.2284(14)	131.9	#2 -x+1/2,y-1/2,-z+1/2
7					
N(3)-H(3N)...N(2)#1	0.72(2)	2.10(2)	2.8080(17)	168(2)	#1 x,-y+1,z+1/2
N(4)-H(4N)...O(4)	0.80(2)	1.87(2)	2.6563(16)	166(2)	#2 -x+1,-y,-z+1
C(8)-H(8A)...O(5)#2	0.95	2.63	3.3387(18)	131.8	#3 -x+1,y,-z+3/2
C(11)-H(11A)...O(1)#3	0.95	2.19	3.0279(16)	147.2	#4 x,y+1,z
C(11)-H(11A)...O(2)#3	0.95	2.37	3.0691(17)	129.9	#5 -x+1,y+1,-z+3/2
C(12)-H(12A)...O(5)#4	0.95	2.28	3.2025(17)	163.4	
C(13)-H(13A)...O(2)#5	0.95	2.43	3.1817(18)	136.2	

Complex **7** crystallized in the monoclinic lattice with four molecules in the unit cell. The ORTEP view of one unit is shown in Fig. 43. The important bond distances and angles are shown in Table 10. The complex containing mononuclear dioxide $[VO_2(L)]^-$ vanadate(V) anion. The vanadium(V) center is surrounded by four base positions being occupied by the donor atoms O1, N1 and O3 from the tridentate Schiff base ligand and two of the oxo group O4. The axial position is occupied by the remaining oxo atom O5 of the VO_2^+ core. The vanadium (V) center in $[VO_2(L)]^-$ has a distorted square-pyramidal coordination sphere. The distorted geometry is characterized by structural parameter τ (0 for an ideal square pyramid and 1 for an ideal trigonal pyramid) [98], which is 0.057. Therefore, the geometry around V(V) center is a slightly distorted square pyramid. The V(V) center is displaced ~ 0.049 Å from the molecular plane O1-O3-O4. The bond distances of V=O are V-O(5) = 1.6163(11) and V-O(4) = 1.6467(11) Å are in the range reported for similar dioxidovanadium complexes [99]. Also, the V-N(1) (imine) bond distance is in the range for similar complexes reported in the literature [100-103]. The two dioxide atoms are in a cis position and the Schiff base (L^{2-}) coordinated to the VO_2^+ moiety through the imine nitrogen atom, one phenolate oxygen and one enolate oxygen atom. An interesting feature of this molecule is the presence of a

$LVO_2^-$the unit which acts as an inorganic analogue of the bridging carboxylate moiety [98]. The space-filling model of complex is shown in Fig. 44.

In this complex, cations and anions are associated by *via* N-H…O and C-H…O hydrogen bonds. The hydrogen bond distances ($d_{D...A}$) are presented in Table 11. Thus, the three-dimensional structure is assembled *via* the columbic interactions between $[VO_2(L)]^-$ anions and imidazolium cations supported through charge assisted hydrogen bonding between protonated imidazolium NH and CH of L^{2-} as hydrogen bond donors, while oxido and methoxy oxygen atoms of the anions act as hydrogen bond acceptors (Fig. 45). The crystal lattice is additionally stabilized by weak lone pair metal chelate interactions with distances ($d_{lp...\pi}$) 3.039 and 2.838 Å (Fig. 46) view of the packing diagram along b axis is shown on Fig. 47. The packing of the complex molecule is controlled by “charge-assisted” by hydrogen bondings, thus hydrogen bond donor and acceptor bear positive-negative charges respectively [104-107]. In unit cell, four molecules of complexes accommodated with charge-assisted hydrogen bondings.

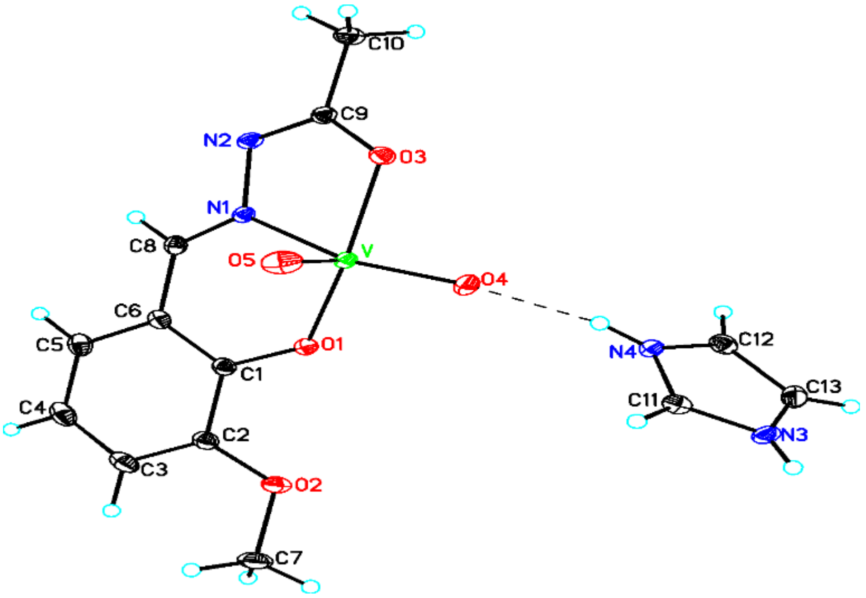

Fig. 43. ORTEP view of complex **7**.

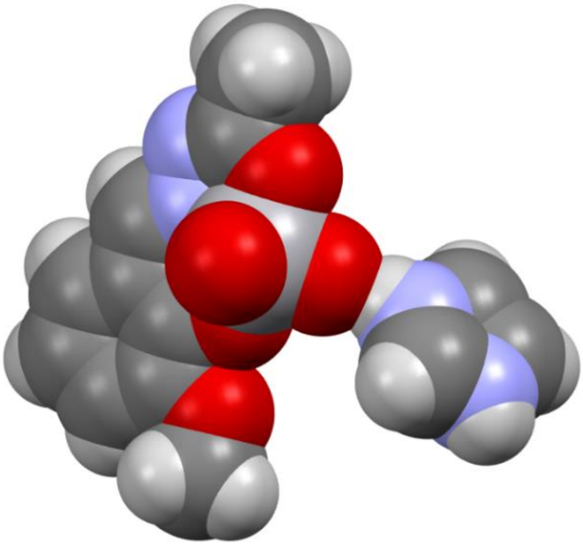

Fig. 44. Space filling model of complex **7**.

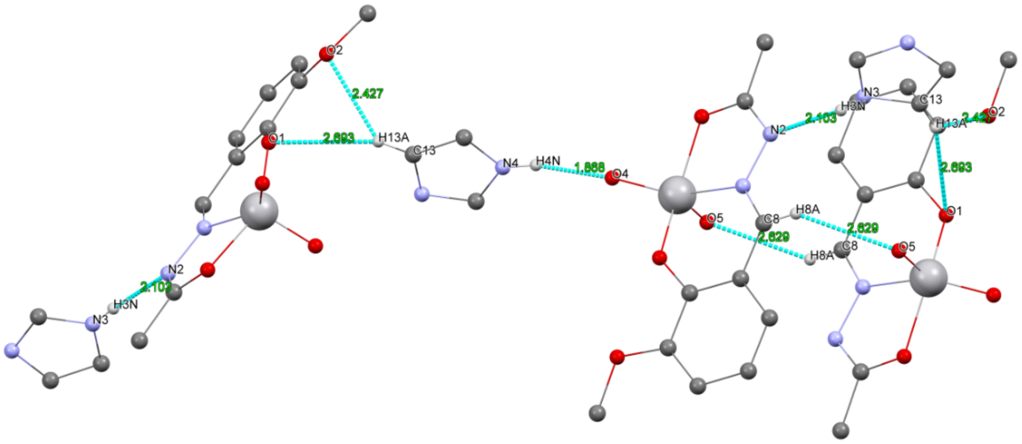

Fig. 45. H-bonding of complex **7**.

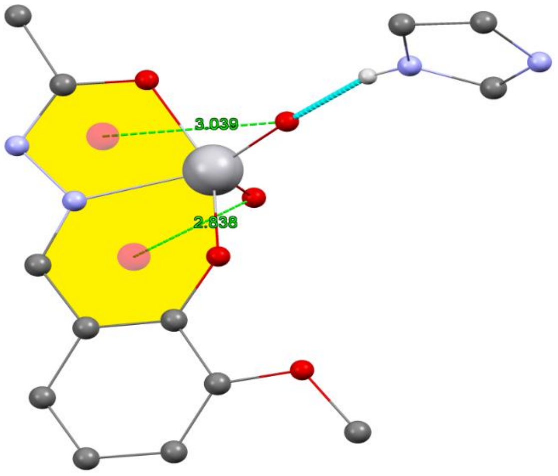

Fig. 46. lp-metal chelate interactions of complex **7**.

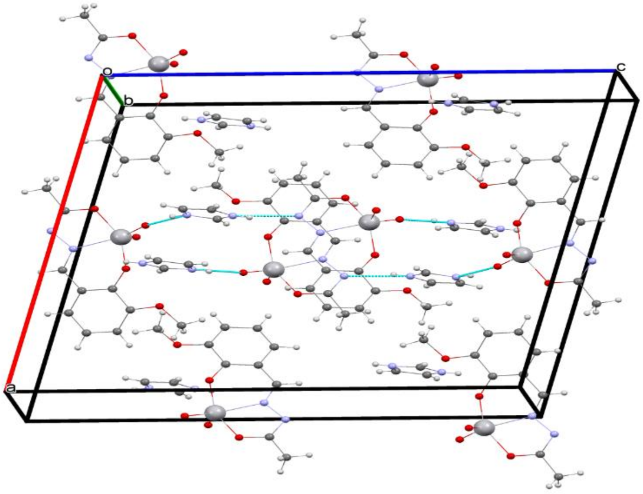

Fig. 47. Packing diagram of complex **7** along with b-axis.

3.8 Hirshfeld Surface Analysis

3.8.1 Hirshfeld surfaces analysis of complexes 3

The Hirshfeld surfaces analysis of complexes **3**, **5**, **6** and **7** were done for guessing the interactions in the formation of supramolecular architecture. The Hirshfeld surfaces for the vanadium complex **3** shown in Fig. 48. To gain an idea about the molecular framework especially the aromatic and chelate rings the surfaces are plotted as transparent. The d_{norm} surface is mapped between -0.25 to 1.25 Å range, shape index plots are constructed between -0.8 to 0.8 Å while curvedness plots are mapped in the range -3.0 to 0.3 Å. In this complex, the O···H interactions as described in crystal structure description (vide supra) can be seen as the large circular deep red depressions and the weaker π···π interactions are shown as the faint red shaded area.

Another salient result of the Hirshfeld surface analysis is the fingerprint plots which are useful for analysing the relative contribution of different intermolecular contacts Fig. 49. In this plot, the complementary regions are presented in such a manner where one molecule act asa donor ($d_e > d_i$) and another as an acceptor ($d_e < d_i$). Also, the total fingerprint plot can be cleaved into several fragments to emphasize specific atom pair close contacts. This helps to estimate the varied contributions of interactions that are present in the molecule. The fingerprint plots of the complex show equal-sized pair of spikes as the light blue region. The most important interaction in the complex is the O···H/H···O interaction which appears as discrete spikes 1.0 Å < (d_e + d_i) < 2.4 Å in the total fingerprint plot of the complex. This is the most dominant interaction existing in the complex with a total contribution of 30.0% of the total Hirshfeld surface area. Apart from this the complex exhibit C-H···π interaction which appears in 1.0 Å < (d_e + d_i) < 2.6 Å in the middle of the fingerprint area with a net contribution of 15.0% in the total Hirshfeld surface area.

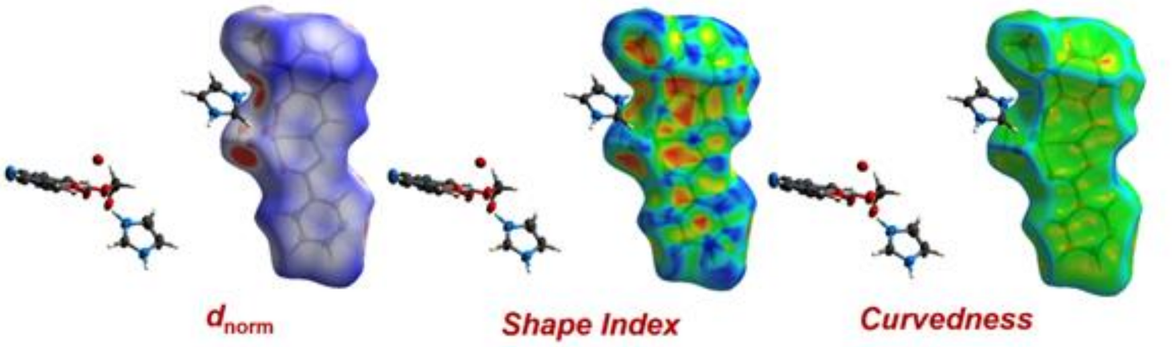

Fig. 48. Hirshfeld surfaces mapped with d_{norm}, shape index and curvedness for the complex **3**.

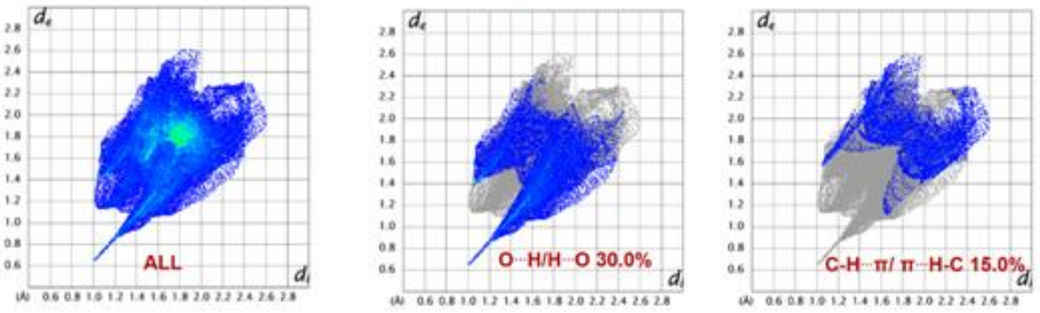

Fig. 49. Fingerprint plots for the complex showing percentages of contact contributed to the total Hirshfeld surface area in complex **3**.

3.8.2 The Hirshfeld surface analysis of complexes 5 and 6

The Hirshfeld surface analysis of complexes **5** and **6** were performed to explore non-covalent interactions present in newly synthesized complexes. The Hirshfeld surfaces for complexes **5** and **6** are presented in Fig. 50. The different surfaces have been mapped over a d_{norm} range of -0.5 to 1.5 Å, shape index (-1.0 to 1.0 Å) and curvedness (-4.0 to 0.4 Å) and for better conception of the aromatic rings, all the surfaces have been constructed in transparent mode. The weak interactions as discussed for both **5** and **6** are portrayed effectively in the spots where large circular deep red depressions as evinced on the d_{norm} surfaces are indicative of hydrogen bonding contacts. The other dominant interaction π···π interactions for **5** and

C−H···π interactions for **6** in Hirshfeld surface plots are evident as the faint red shaded area in Fig. 51.

The fingerprint plots for **5** and **6** are shown in Fig. 51. The complementary regions in the fingerprint plots are visible where one molecule acts as a donor ($d_e > d_i$) while the other acts as an acceptor ($d_e < d_i$). The N−H···O and C-H···O interactions for both **5** and **6** appear as two distinct spikes of almost equal lengths in the 2D fingerprint plots in the region 2.62 Å < ($d_e + d_i$) < 2.61 Å as a light sky-blue pattern in full fingerprint 2D plots. In **5**, π···π interaction area is lying at the center of the fingerprint plot in the region 2.12 Å < ($d_e + d_i$) < 2.10 Å while in **6**, C−H···π interactions appears with two equal spikes in the region 2.45 Å < ($d_e + d_i$) < 2.43 Å. The fingerprint plots can be decomposed to highlight particular atom pair close contacts. This decomposition enables the separation of contributions from different interaction types, which overlap in the full fingerprint. The proportion of O···H interactions constitutes 30.9% and 36.1% of the total Hirshfeld surfaces in **5** and **6**, respectively. While other relevant interactions like π···π and C–H···π interactions in **5** and **6** are having contributions of 6.1% and 20.0% in their respective Hirshfeld surfaces.

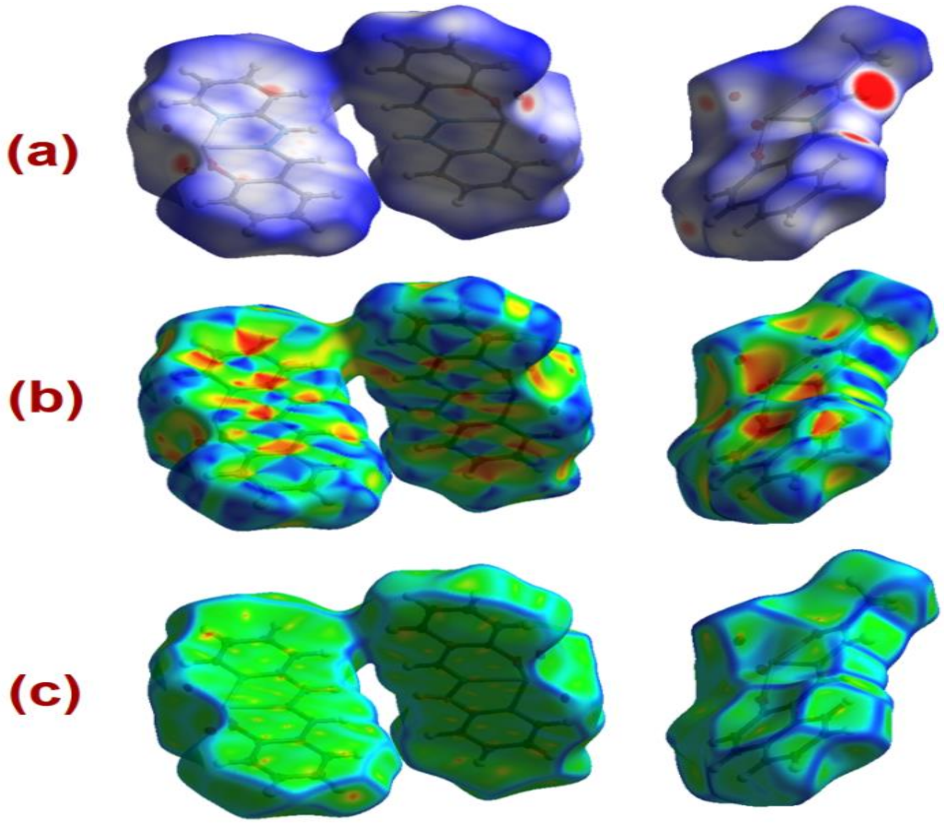

Fig. 50. Hirshfeld surfaces mapped with (a) d_{norm}, (b) shape index and (c) curvedness for complex **5** (left panel) and complex **6** (right panel).

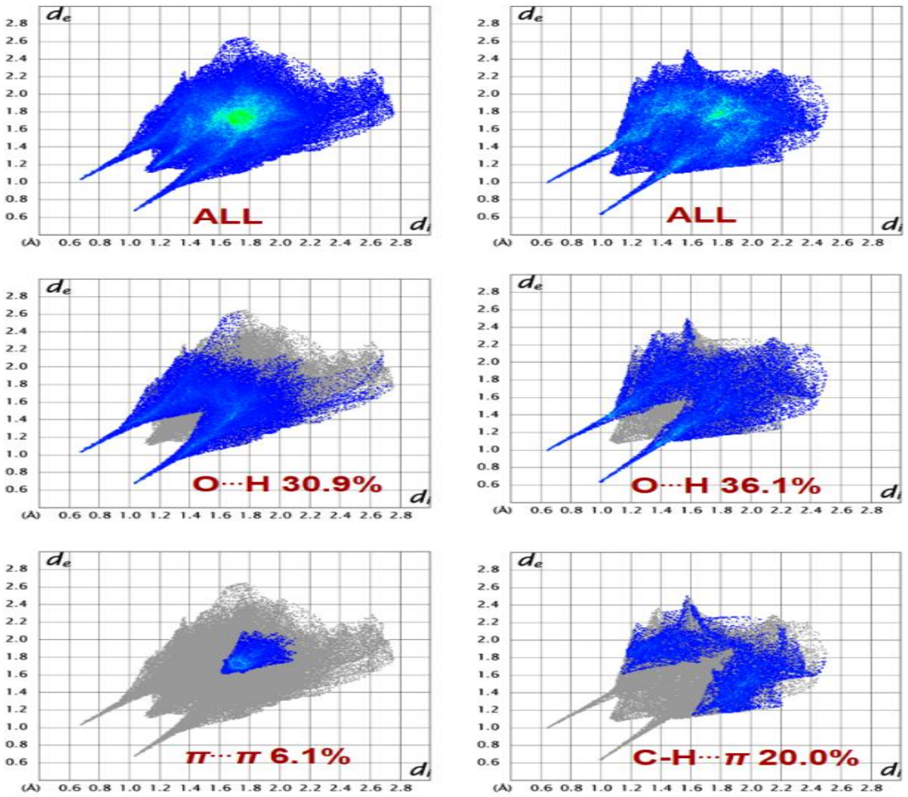

Fig. 51. Fingerprint plots for compplex **5** (left panel) and complex **6** (right panel) showing percentages of contact contributed to the total Hirshfeld surface area of the molecules.

3.8.3 Hirshfeld surface of the complex 7

The Hirshfeld surface and fingerprint plots of a compound yield a comparative picture of modes of non-covalent interactions. The Hirshfeld surface of complex **7** is shown in Fig. 52. For the complex the d_{norm} surface is mapped between the range of -0.73 to 1.45 Å, shape index is constructed between -1.0 to 1.0 Å and the curvedness is mapped in the range -4.0 to 0.4 Å. All of these surfaces are presented transparently to offer better visualization of all the aromatic rings present in the ligand. The O···H-N and O···H-C interactions which are discussed in the molecular structure description (vide supra) can be visualized as a different type of spots in the d_{norm} surface. The large circular deep red depressions in d_{norm} surface are indicative of O···H-N and O···H-C hydrogen bonding interactions as faint red shaded area while the weak π···π interactions are present as faded areas in the d_{norm} plot of the complex.

In the fingerprint plot of the complex Fig. 53. the opposite regions are shown in the mode where one molecule is acting as a donor ($d_e > d_i$) whilst another behave as an acceptor ($d_e < d_i$). The fingerprint plot of the complex possess various equal-sized spikes which are indicative of the different interactions present in the complex (vide infra). The most important interaction in the ligand is the O···HN/NH···O and O···HC/CH···O interactions which appear as discrete but unequal pair of spikes 1.0 Å < (d_e + d_i) < 2.5 Å in the total fingerprint plot of the complex and contributes 17.9% of the total Hirshfeld surface area. Besides, Cl···H/H···Cl interaction also appears as pair of equal-sized spikes appearing in the region 1.0 Å < (d_e + d_i) < 3.0 Å in the total fingerprint plot of the complex and contributing 37.7% of the total Hirshfeld surface area. Unlike, these interactions, the π···π interactions are appearing as the very small sized patch in the center of the total fingerprint plot of the complex appearing in the region 1.7 Å < (d_e + d_i) < 2.1 Å in the total fingerprint plot of the complex and contributes 2.3% of the total Hirshfeld surface area.

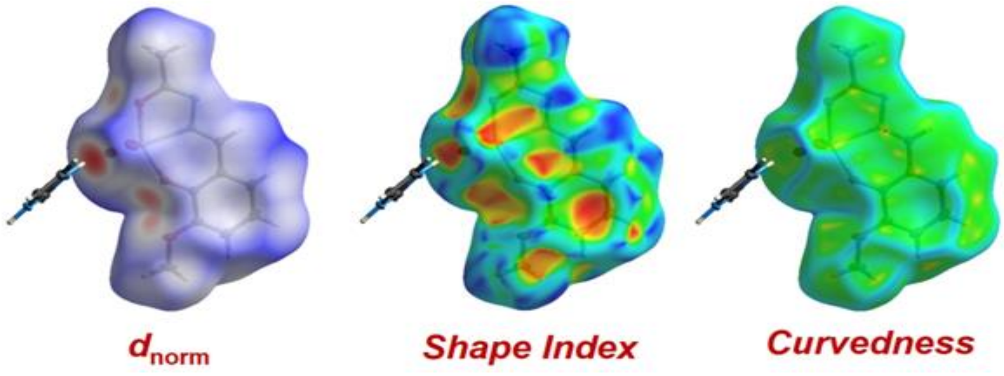

Fig. 52. Hirshfeld surfaces mapped with d_{norm}, shape index and curvedness for the complex **7**.

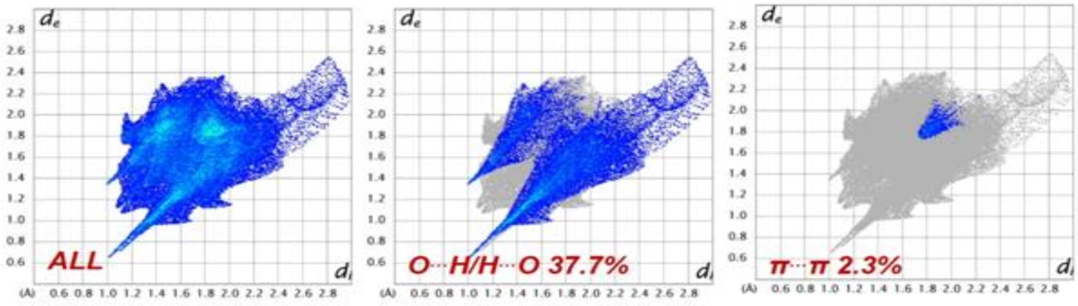

Fig. 53. Fingerprint plots for the complex showing percentages of contact contributed to the total Hirshfeld surface area of complex **7**.

3.9 Magnetic and EPR spectral study

Room temperature magnetic measurements of complexes **1**, **2** and **4** were performed. The complexes **1**, **2** and **4** show magnetic moment of 1.79, 1.77 and 1.83 BM respectively in accord with a spin only value of a d^1 the system, whereas vanadium(V) complex **3**,**5**, **6** and **7** which are d^0 system is diamagnetic. The magnetic moment values of **1**, **2** and **4** are in agreement with EPR results. The complexes **1-4** were also characterized by EPR spectral measurements at room temperature (RT) Fig. 54. and liquid nitrogen temperature (LNT) Fig. 55. by dissolving complexes in DMSO. The EPR parameters from isotropic and anisotropic spectra for oxidovanadium (IV) complexes were evaluated from the experimental EPR spectrum (Table 12). The oxidovanadium complexes **1**, **2** and **4** are characteristic of the +4-oxidation state of the ^{51}V isotope (99.76% atom nuclear spin I = 7/2) and have a S = 1/2 electron spin. EPR spectra in liquid at RT of the oxidovanadium(IV) complexes viz., **1**, **2** and **4** reveal eight resonance lines attributable to a single S = 1/2 complex in which the unpaired electron in a d_{xy} orbital is coupled to the nuclear spin I = 7/2 of the vanadium nucleus. Such eight-lines isotropic spectral patterns are consistent with the magnetic moments and reveal that the ligand dissociation has not occurred during EPR sample preparations. The anisotropic EPR parameters for these complexes also evaluated from anisotropic EPR spectra (Table 12). From the anisotropic parameters it is clear, only subtle changes are incurred between the parameters of these complexes, despite the different equatorial ligand field strengths for N_2O_2 and NO_3. However, such anisotropic EPR data should prove useful for recognizing donor equatorial atoms bound to the vanadyl (VO^{2+}) unit in various proteins and enzymes. Such electronic and nuclear spin features are used to know the types of sites coordinated to the complex ion. Additively relationship is used to estimate the parallel hyperfine constant of oxidovanadium(IV) complexes based on the contribution to $A_{||}$ from each of four equatorial donor sites [109]. This relationship gives a good criterion to guess the equatorial donor atoms. The calculations were made according to the additive relationship, using closing values of partial contribution of the equatorial ligand functions [110]. Complex **3, 5, 6** and **7** do not give eight lines isotropic EPR spectral features. Also, the anisotropic EPR spectra of this complex are featureless. Such EPR spectral features are indicative of oxidovanadium(V) oxidation state of the vanadium and being diamagnetic, it is EPR silent.

Table 12 EPR parameters of oxidovanadium complexes.

Complex	**Donor set**	$g_{\|\|}$	$g_{\perp}$	g_{iso}	$A_{\|\|}$ $(1x10^{-4}cm^{-1})$	$A_{\perp}$ $(1x10^{-4}cm^{-1})$	A_{iso} $(1x10^{-4}cm^{-1})$
1	NO_3	1.936	1.988	1.976	180	71	104
2	N_2O_2	1.932	1.985	1.973	183	71	105
4	N_2O_2	1.932	1.987	1.876	182	71	105

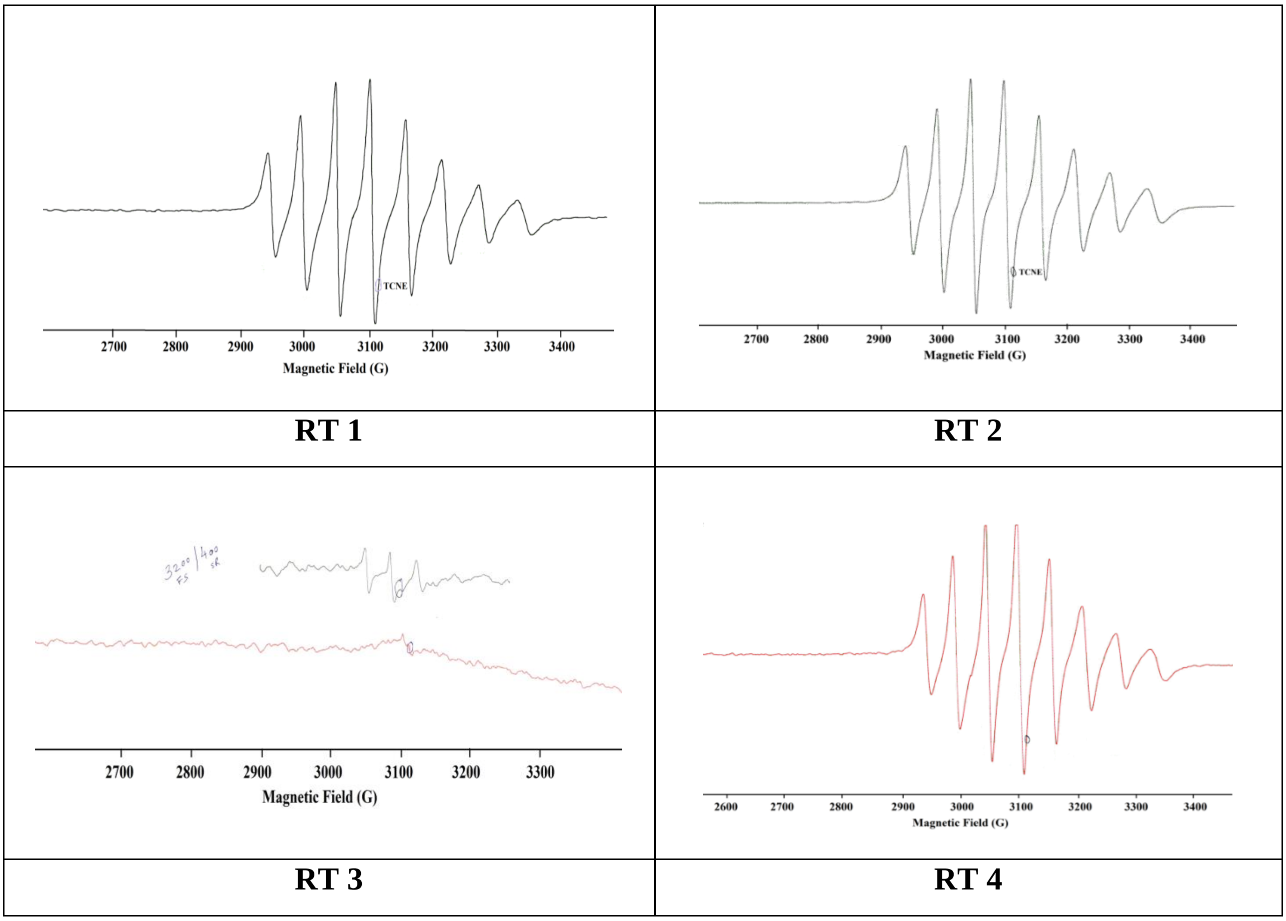

RT 1

RT 2

RT 3

RT 4

Fig. 54. EPR spectra of complexes **1-4** at room temperature.

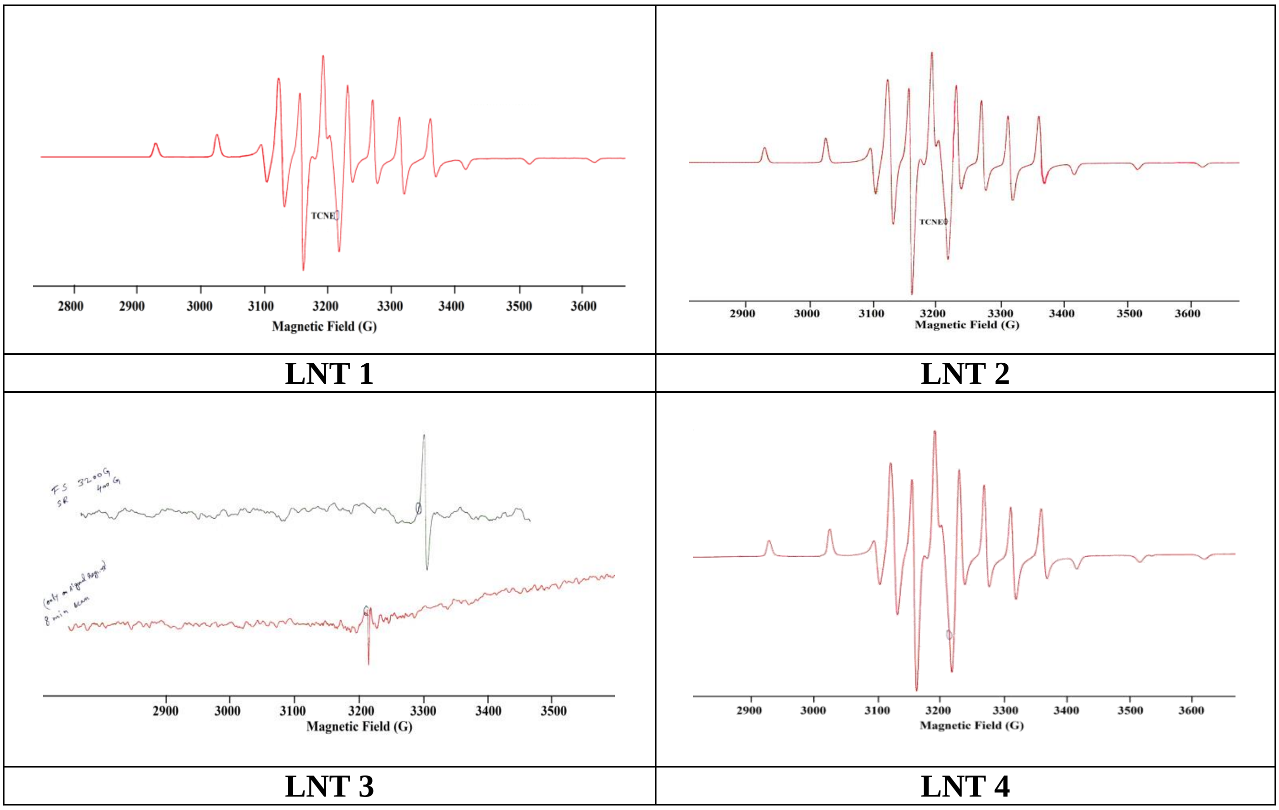

LNT 1

LNT 2

LNT 3

LNT 4

Fig. 55. EPR spectra of complexes **1-4** at Liquid nitrogen temperature.

3.10 Cyclic Voltammetry of complexes 1-4

The electrochemical behaviour of all complexes was studied in DMSO solution (3.0 × 10^{-3} M) using cyclic voltammetry (CV). Tetra butyl ammonium perchlorate (TBAP) was used as a supporting electrolyte. Cyclic voltammograms are shown in Fig. 56. The results of the cyclic voltammetric studies for oxidovanadium(IV/V) complexes are presented in Table 13. The cyclic voltammetric studies in DMSO reveal a one-electron reduction process in the range of -0.73 to -0.84 V [111]. In this oxidovanadium(IV/V) complexes, there is not an obvious oxidation peak that can be assigned to

Vanadium(III) → Vanadium(IV)

Vanadium(IV) → Vanadium(V)

the reaction during the reverse anodic scan. The oxidovanadium(V) complex **3** has a different coordination number and equatorial donor set. Therefore, it probably shows less negative cathode potential than that of oxidovanadium(IV) complexes.

Table 13 Cyclic voltammetric data of complexes **1-4.**

Complex	E_{pc}(V)	E_{pa}(V)	Reduction Process	Equatorial donor set
1	-0.83	Not defined	IV → III	NO_3
2	-0.77	Not defined	IV → III	N_2O_2
3	-0.73	Not defined	V → IV	N_3O
4	-0.84	Not defined	IV → III	N_2O_2

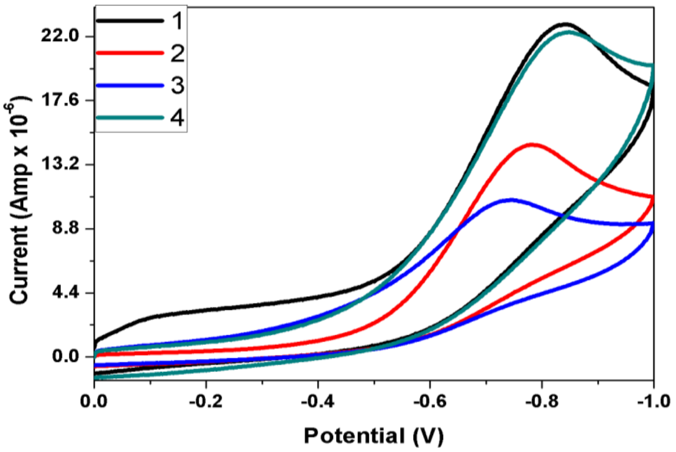

Fig. 56. Cyclic voltammograms of vanadium(IV/V) complexes **1-4** in DMSO at an Ag/AgCl electrode with a scan rate of 300 mVs^{-1} and temperature 20°C.

3.10.1 Cyclic voltammograms of complexes 5-7

The redox behavior of complexes **5**, **6** and **7** were studied using cyclic voltammetry (CV) and differential pulse voltammetry (DPV) techniques in DMSO solution (0.1M TBAP) at a 300mV scan rate. CV and DPV diagrams are shown in Fig. 57. and electrochemical parameters are shown in Table 14. One reduction and one oxidation peak are seen in the CV of all complexes corresponding to electron transfer Fig. 57 (a). Although the oxidation waves are less defined. The associated reduction of the metal ion as showing below

$$\mathbf{V(V)\rightarrow V(IV)}$$

The values of cathodic peak potential (E_{pc}) for these complexes are highly negative (Table 14) owing to anionic Schiff base coordination to the vanadium centre which makes the reduction of the metal centre unfavourable [85]. The cathodic peak potential (E_{pc}) in these complexes is within the range of previously reported values for the reduction (V^{V}/ V^{IV}) of the similar hydrazone Schiff bases [112]. The redox waves are quasi-reversible as the peak-to-peak separation remain ΔE 0.272 V in **5**, 0.292 in **6** and0.360 in **7** [85, 112, 113]. The quasiirreversible behaviour of the redox process was ascertained by comparing the cyclic voltammetry at different scan rate [114, 115]. Similar reduction peaks (Fig. 57 (b) were observed using differential pulse voltammetry.

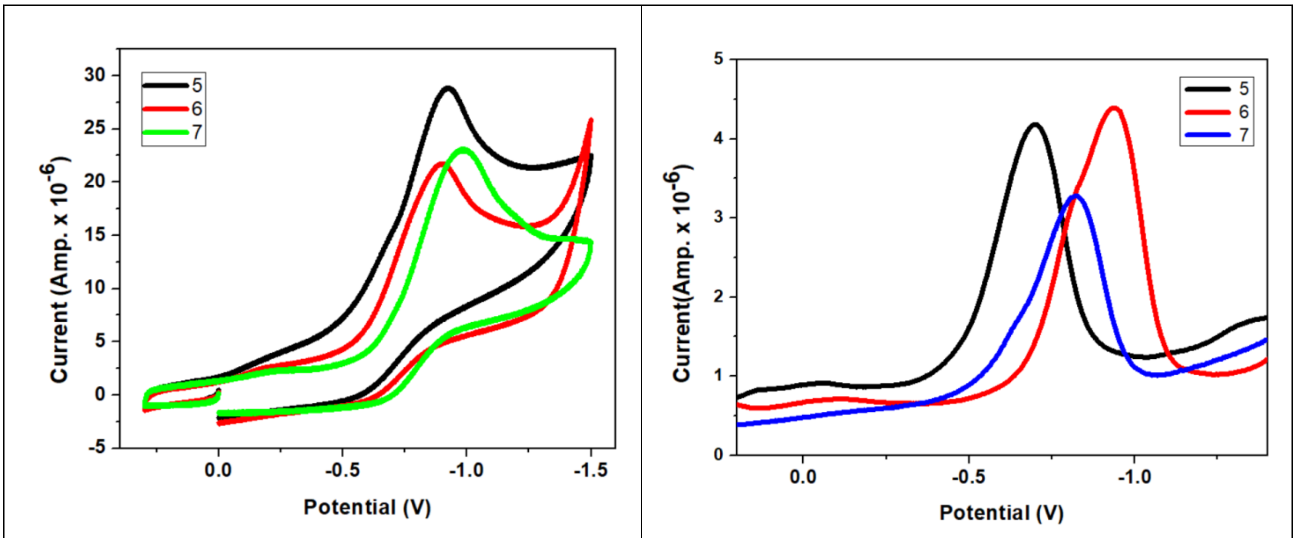

(a) **(b)**

Fig. 57(a) Cyclic voltammograms and **(b)** differential pulse voltammograms of vanadium(IV/V) complexes **1-4** in DMSO at an Ag/AgCl electrode with a scan rate of 300 mVs^{-1} and temperature 20°C.

Table 14 Electrochemical parameters for complexes **5-7**.

Complex	**E_{pc}(V)**	**E_{pa}(V)**	**ΔE(V)**	**$E_{1/2}$(V)**	**d_{pc}**
5	-0.9240	-0.6511	0.272	-0.787	-0.6978
6	-0.8984	-0.6011	0.297	-0.750	-0.6412
7	-0.9832	-0.6230	0.360	-0.803	-0.6096

3.11 Theoretical calculations

To gain insight into the electronic structures of complexes full geometrical optimization of complexes **1-4** was performed. The optimized geometrical parameters (bond lengths and angles), Mullikan densities and charges, global reactivity parameters and energies of frontier molecular orbitals (FMO) were computed and analyzed. From the elemental analysis (C,H,N) and spectroscopic experimental data, it is proved that vanadium ions coordinated to the tridentate Schiff base *via* N and O atoms forming the complexes **1** and **2** whereas in **3** and **4** co-ligand imidazoles are also coordinated. Molecular structures of **3** are also analyzed by single-crystal X-ray analysis.

The optimized molecular geometry of complexes with atom numbering **1-4** is shown in Fig 58-61. The bond parameters are listed in Table 15. The molecular geometry in complexes **1**, **2** and **4** is distorted square pyramidal whereas in **3** is octahedral. The distortion in five coordinated complexes was ascertained using angular structural index τ_5 (equation. 1) [98],

$$\tau_5 = \theta_1 - \theta_2 / 60 \qquad \ldots(1)$$

where θ_1 and θ_2 are the largest angles in five-coordinate complexes **1**, **2** and **4**. Hence, for a perfect trigonal pyramidal structure with D_{3h} symmetry has a τ_5 =1, while for perfect square pyramidal structure with C_{4v}symmetry has $\tau_5 = 0$.For present complexes τ_5 is 0.07 for **1**, 0.142 for **2**, and 0.262 for **4**. Therefore, in complex **1** there is a minor distortion in comparison to remaining complexes **2** and **4**. Complex **3** is hexacoordinated with distortion. In hexacoordinated geometry, the distortion can be shown through a tetragonality parameter (τ) as $T = R_{int}/ R_{out,}$ in which R_{int} is average in-plane and R_{out} average out of plane bond distances. The value of $T < 0.9$ reveals static and $T = 1$ dynamic distortion in hexacoordinated geometry. For this complex value of $T = 0.95$ which is almost equal to unity. Therefore, the geometry around vanadium center is assigned as a dynamic distortion. In complex **3** dynamic distortion

T = 0.95 on is observed [116]. The bond lengths and bond angles of this complex compare nicely with the experimental data as obtained from single crystal X-ray analysis. In these complexes the bond length of V=O is 1.636 Å for **1**, 1.836 Å for **2**, 1.593 Å for **3** and 1.642 Å for **4** is similar to the reported similar geometry vanadium complexes [117, 118]. Other bond lengths *viz.*, V-N and V-O are also comparable to reported values of bond lengths in similar complexes [117-119].

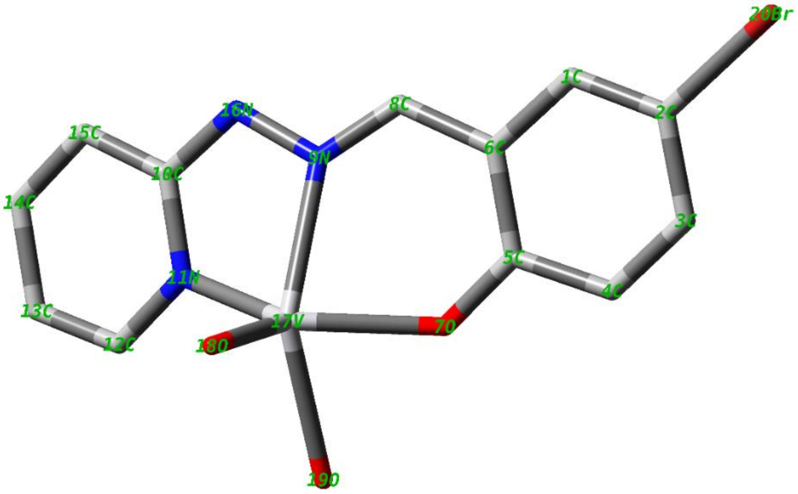

Fig. 58. Optimized structures of complexes **1**.

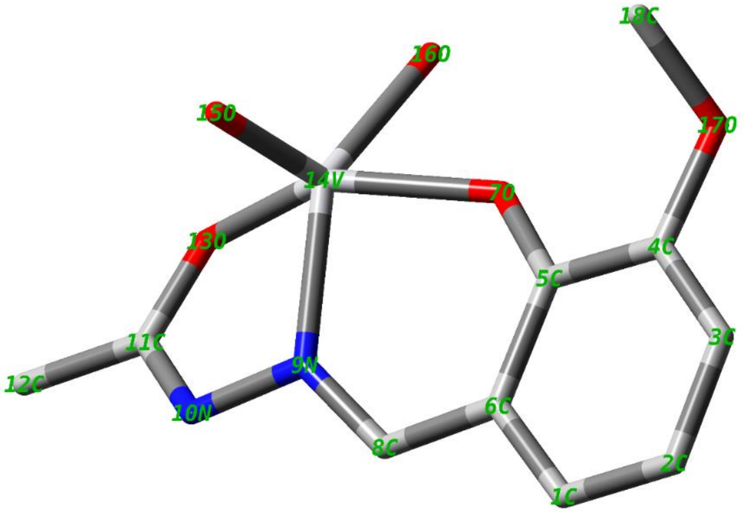

Fig. 59. Optimized structures of complexes **2**.

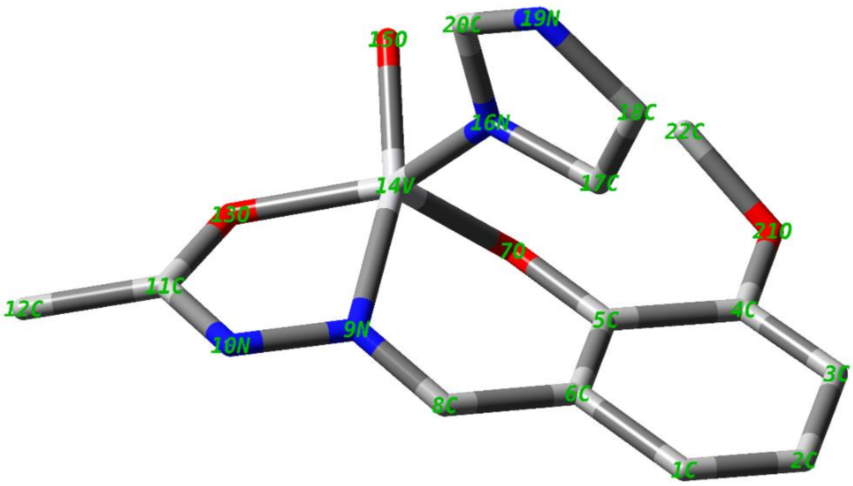

Fig. 60. Optimized structures of complexes **3**.

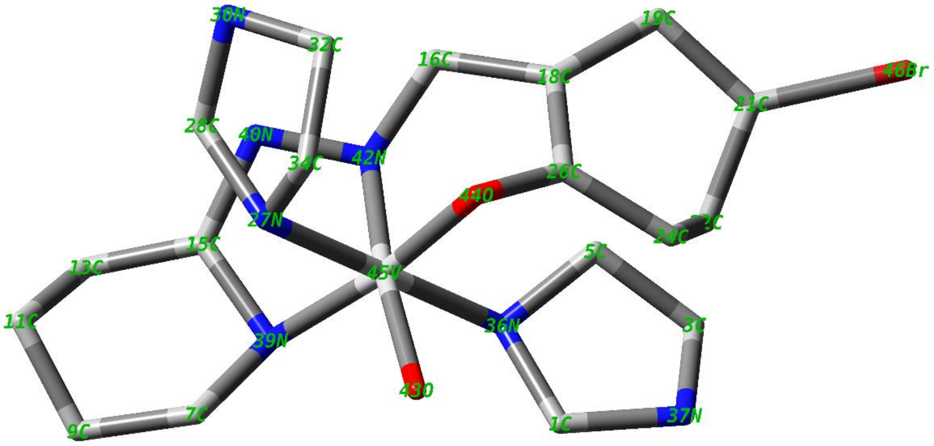

Fig. 61. Optimized structures of complexes **4**.

Table 15 Theoretical Bond lengths [Å] and angles [°] for complexes **1-4**.

1		**2**		**3**		**4**	
Bond lengths							
V(14)-N(9)	1.884	V(17)-N(9)	1.897	V(45)-N(27)	2.132	V(14)-N(9)	1.880
V(14)-O(7)	1.862	V(17)-N(11)	1.899	V(45)-N(36)	1.097	V(14)-N(16)	1.901
V(14)-O(13)	1.865	V(17)-O(7)	1.858	V(45)-N(39)	2.097	V(14)-O(7)	1.845
V(14)-O(15)	1.636	V(17)-O(18)	1.836	V(45)-N(42)	2.230	V(14)-O(13)	1.870
V(14)-O(16)	1.860	V(17)-O(19)	1.860	V(45)-O(43)	1.593	V(14)-O(15)	1.642
				V(45)-O(44)	1.923		
Bond angles							

O(7)-V(14)-N(9)	99.55	O(7)-V(17)-N(9)	93.39	N(27)-V(45)-N(39)	90.16	O(7)-V(14)-N(9)	99.95
O(7)-V(14)-O(13)	127.58	O(7)-V(17)-N(11)	126.37	N(27)-V(45)-N(42)	82.34	O(7)-V(14)-O(13)	112.28
O(7)-V(14)-O(15)	109.01	O(7)-V(17)-O(18)	87.65	N(27)-V(45)-O(43)	95.35	O(7)-V(14)-O(15)	101.48
O(7)-V(14)-O(16)	87.39	O(7)-V(17)-O(19)	115.80	N(27)-V(45)-O(44)	87.57	O(7)-V(14)-N(16)	104.62
N(9)-V(14)-O(13)	78.48	N(9)-V(17)-N(11)	81.52	N(36)-V(45)-N(39)	89.98	N(9)-V(14)-O(13)	80.18
N(9)-V(14)-O(15)	92.33	N(9)-V(17)-O(19)	94.73	N(36)-V(45)-N(42)	88.30	N(9)-V(14)-O(15)	158.54
O(13)-V(14)-O(15)	123.38	N(11)-V(17)-O(18)	91.50	N(36)-V(45)-O(43)	94.37	N(9)-V(14)-N(16)	89.64
O(13)-V(14)-O(16)	89.15	N(11)-V(17)-O(19)	117.80	N(36)-V(45)-O(44)	88.40	O(13)-V(14)-O(15)	91.10
O(15)-V(14)-O(16)	95.06	O(18)-V(17)-O(19)	91.88	N(39)-V(45)-N(42)	73.79	O(13)-V(14)-N(16)	142.84
				N(39)-V(45)-O(43)	94.75	O(15)-V(14)-N(16)	85.56
				N(39)-V(45)-O(44)	156.55		
				N(42)-V(45)-O(44)	82.78		
				O(43)-V(45)-O(44)	108.68		

3.12 HOMO-LUMO analysis

The frontier molecular orbitals (FMO), highest occupied molecular orbital (HOMO), lowest unoccupied molecular orbitals (LUMO) are used to ascertain electron donors and acceptors. These parameters affect the bioactivity and give an idea about the way a molecule interact with the biological species [120,121]. The research on their FMO can yield knowledge for the operating mechanism of the biologically active compounds [122,123]. The HOMO-LUMO plots are complexes **1-4** shown in Fig. 62-65. In complex **1** HOMO and LUMO orbitals are confined on tridentate Schiff base ligand except in HOMO-1 and LUMO+3. These are localized on vanadium cation. In complex **2**, all HOMO and LUMO are limited on tridentate Schiff base ligand except HOMO-1 is hosed on vanadium ion. In complex **3**, all HOMO and LUMO are restricted on Schiff base ligand. In complex **4**, all HOMO (HOMO, HOMO-1, HOMO-2 and HOMO-3) are confined on Schiff base ligand. Similarly, LUMO and LUMO-3 are exclusively limited on imidazole co-ligand and LUMO+1 is restricted on vanadium(V), Schiff base and imidazole and LUMO+2 is confined on only Schiff base. On the basis of these observations one can suggest that the vanadium cation coordinated tridentate Schiff base and imidazole (co-ligand) may be the reactive sites of complexes **1**-**4**.

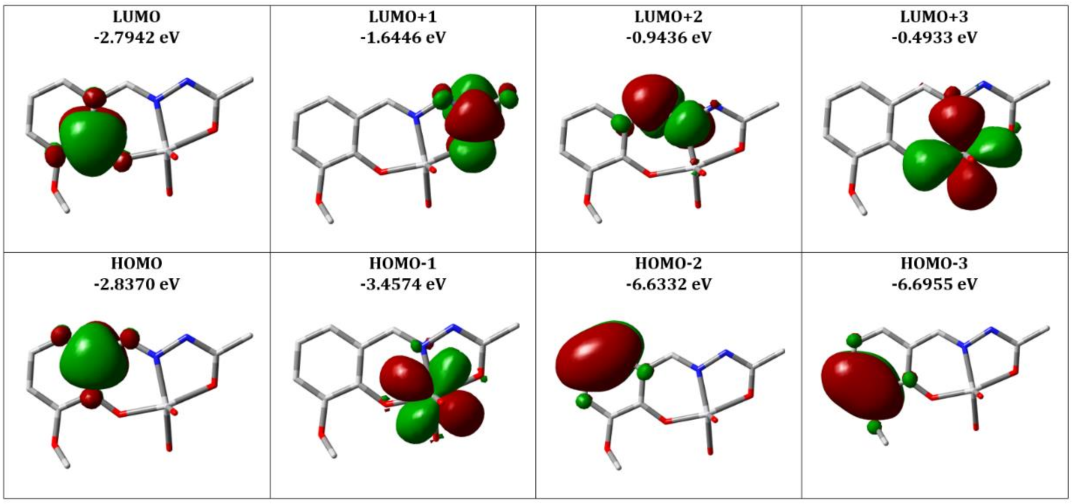

Fig. 62. HOMO-LUMO energy diagrams of complex **1**.

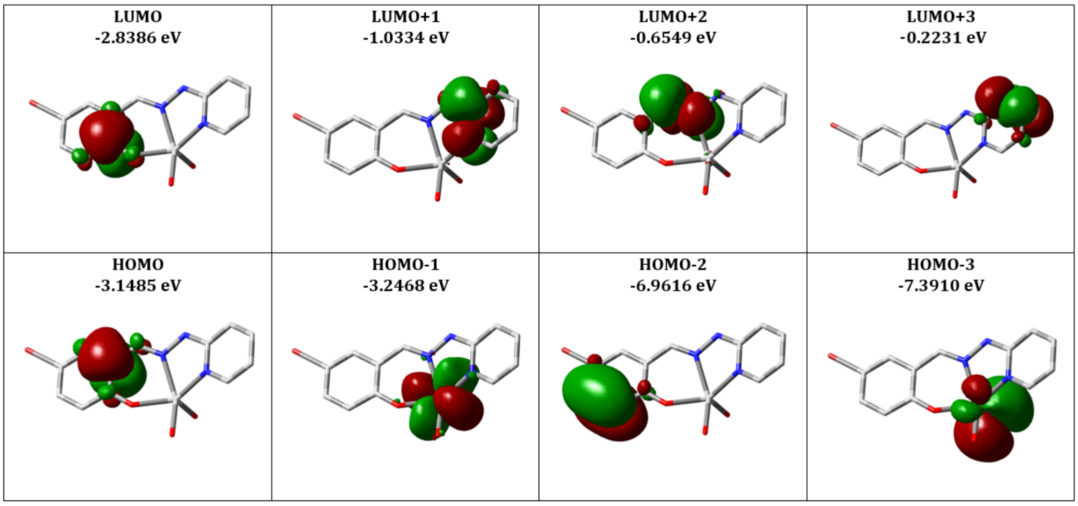

Fig. 63. HOMO-LUMO energy diagrams of complex **2**.

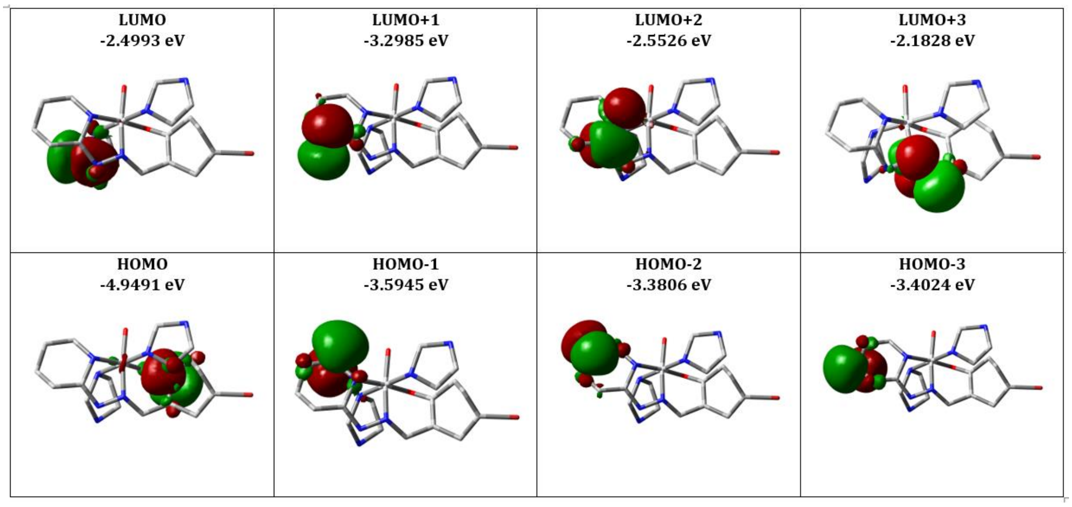

Fig. 64. HOMO-LUMO energy diagrams of complex **3**.

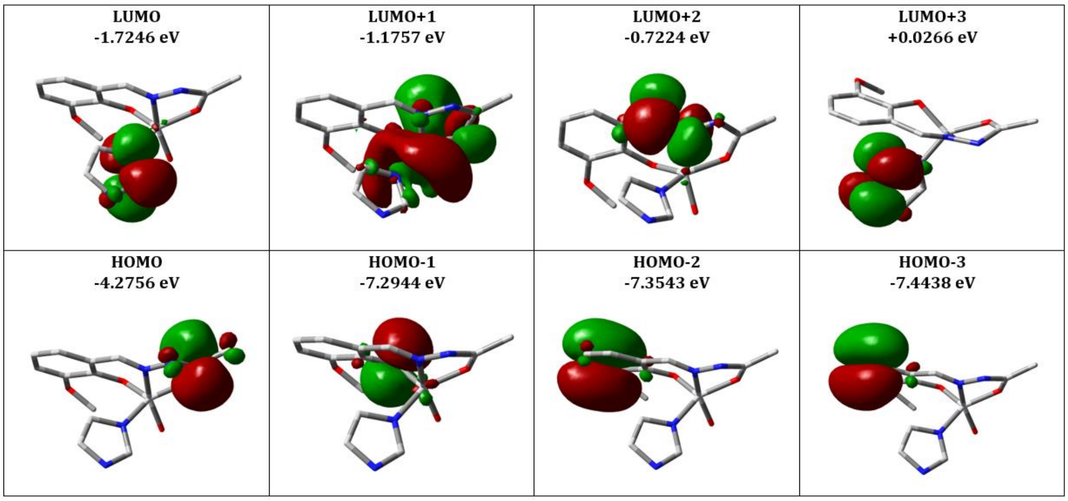

Fig. 65. HOMO-LUMO energy diagrams of complex **4**.

3.13 Mulliken charge analysis

The Mulliken charge analysis of present complexes was also performed and listed in Table 16. It is established that the atomic charge populations of a molecule are well correlated to active sites in its electrophilic or nucleophilic reactions and the charge interactions between two species [123], such interactions can show the functional role in inhibiting the growth of fungi [123]. On perusal of Mulliken population data, it is apparent that the coordination leads to the redistribution of electron density in the coordinated moieties. The transferred charge reduces the polarization of complex molecules [124]. In the studies of complexes, the vanadium cation gains electrons to reveal positive charges of 0.8263 for **1**, 1.0260 for **2**, 0.3609 for **3** and 0.7555 for **4**. Similarly, Mulliken densities remain positive on vanadium centers only. The reduced polarity of compounds is useful for the enhanced penetration of complexes into the lipid membranes and hence increases the bioactivities of the compounds.

Table 16 The Mullikendensities and charges of metal and donor atoms for complexes **1-4**.

Complexes	Metal and Donor atom	Mulliken charges	Mulliken densities
1	V14	0.8263	0.9661
	N9	-0.2535	-0.0409
	O7	-0.5878	-0.0275
	O13	-0.3796	-0.0179
	O15	-0.4339	-0.1749
	O16	-0.7552	-0.0028
2	V17	1.0260	1.3043
	N9	-0.3884	-0.0189
	N11	s-0.6415	-0.1396
	O7	-0.6939	-0.0069
	O18	-0.7879	-0.0967
	O19	-0.8567	-0.0358
3	V45	0.3609	0.7637
	N27	-0.2243	-0.0185
	N36	-0.2133	-0.0035
	N39	-0.2834	-0.0196
	N42	-0.2224	-0.0682
	O43	-0.4364	-0.0167
	O44	-0.2961	-0.0032
4	V14	0.7555	0.8964
	N9	-0.2439	-0.0157
	N16	-0.2351	-0.0169
	O7	-0.5393	-0.0289
	O13	-0.3313	-0.1967
	O15	-0.4034	-0.1896

3.14 Global chemical reactivity indices of complexes 1-4

Density functional theory yields the important molecular descriptors [125]. These descriptors decide the structural stability and reactivity of a molecule. From the energies of frontier molecular orbitals (FMO), the highest occupied molecular orbitals (HOMO) and lowest unoccupied molecular orbitals (LUMO) are useful in deciding some global reactivity parameters of molecules [126,127]. The parameters are defined in Table 17. These are electronic chemical potential (μ), electro-negativity (χ), ionization potential (I) and electron affinity (EA). The electronic chemical potential (μ) of a molecule is the escaping tendency of electrons from a molecule, the negative value of μ reveals that the molecule does not decompose spontaneously into its constitutional elements. Global hardness decides the resistivity of molecules [128]. A molecule with a large energy gap (ΔE) is a feature of a hard molecule whereas with a small ΔE a soft molecule being more reactive. Hard molecules are small and less polarizable in comparison to soft molecules having high polarizability. From the table, it is clear that complex **4** is the hardest among all complexes, whereas complex **1** is the most chemically soft molecule. The observed trend with respect to softness: **1** > **2** > **3** > **4**. These results are inconsistent with the ΔE. The electrophilicity index (ω) is a thermodynamic feature of a molecule and related to chemical potential and global hardness are suggestive of nucleophilicity power. Therefore, ω plays an important role in illustrating the chemical reactivity of a molecule [129]. Complex **4** showed the lowest value with the lowest electrophilicity index, whereas complex **1** has the highest value of ω and is the strongest electrophilic. The observed trend is: **1** > **2** > **3** > **4**.

Table 17 Global reactivity parameters for complexes **1-4**.

Molecular descriptors	Mathematical description	1	2	3	4
E_{HOMO}	Energy of HOMO	-2.8370	-3.1485	-4.9491	-4.2756
E_{LUMO}	Energy of LUMO	-2.7942	-2.8386	-2.4993	-1.7246
Energy gap	$\Delta E_g = E_{HOMO} - E_{LUMO}$	0.0428	0.3099	2.4498	2.5510
Ionization potential (IP)	$IP = - E_{HOMO}$	2.8370	3.1485	4.9491	4.2756
Electron Affinity (EA)	$EA = - E_{LUMO}$	2.794	2.8386	2.4993	1.7246
Electronegativity (χ)	$(\chi) = -\frac{1}{2}(E_{HOMO} + E_{LUMO})$	2.8156	2.9936	3.7242	3.0001
Chemical potential (μ)	$(\mu) = \frac{1}{2}(E_{HOMO} + E_{LUMO})$	-2.8156	-2.9936	-3.7242	-3.0001
Global Hardness (η)	$(\eta) = -\frac{1}{2}(E_{HOMO} - E_{LUMO})$	0.0214	0.1549	1.2249	1.2755
Softness (S)	$(S) = \frac{1}{2\eta}$	23.3645	3.2279	0.4082	0.3920
Electrophilicity index (ω)	$(\omega) = \frac{\mu^2}{2\eta}$	185.2244	28.9252	5.661	3.5282
Electron donating capability (ω^-)	$(\omega^-) = (3E_{Homo}+E_{Lumo})^2 / 16 (E_{Homo}- E_{Lumo})$	186.6348	30.4324	7.6767	5.1877
Electron accepting capability (ω^+)	$(\omega^+) = (E_{Homo}+3E_{Lumo})^2 / 16 (E_{Homo}- E_{Lumo})$	183.8192	27.4394	3.9526	2.2479

3.15 Computational studies of complexes 5-7

Theoretical studies for the electronic structures of both dioxidovanadium(V) complexes was also optimized by DFT methods [44-46]. Frontier molecular orbitals (FMO) have a major role in elucidating the molecular reactivity, electrical and optical properties of compounds. These orbitals are familiar as the highest occupied molecular orbital (HOMO) and lowest unoccupied molecular orbital (LUMO). The optimized structures of complexes **5-7**are shown in Fig. 66-68. The contour plots of some selected molecular orbitals and their energy gaps (ΔE = HOMO-LUMO) are shown in Fig. 69-71. The energies of eight molecular orbitals *viz*., HOMO, LUMO and their two upper and two lower energy orbitals as shown in Fig. 69-71. (HOMO-1, HOMO-2, LUMO+1 and LUMO+2) for both complexes were examined in negative values suggesting that these complexes are stable [130]. The ΔE between two HOMO and LUMO indicates a stable structure, while a smaller ΔE shows a more reactive molecule. The calculated ΔE for present complexes is collected in Table 18. The order of ΔE is as: **6** > **5** > **7**. Spin density plot of complex 7 is shown in Fig. 72.

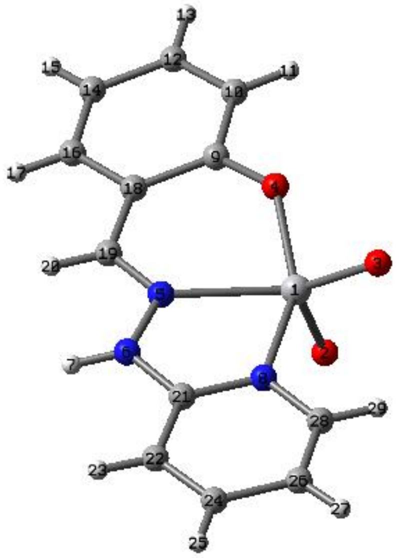

Fig. 66. Optimized structure of complex **5**.

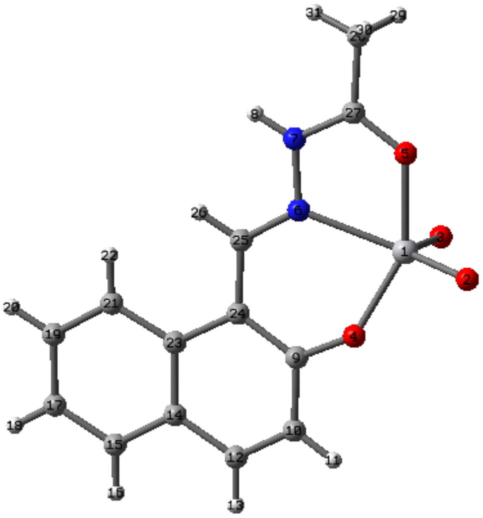

Fig. 67. Optimized structure of complex **6**.

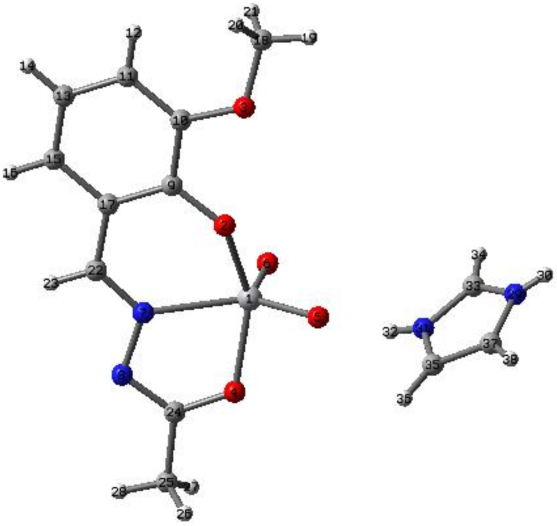

Fig. 68. Optimized structure of complex **7**.

Also, ΔE, E_{HOMO} and E_{LUMO} values are used to predict the global reactivity descriptors, which also explain the internal charge transfer, stability and reactivity of molecules [130]. The global reactivity parameters such as electro-negativity (χ), global hardness (η), electrophilicity (ω), ω^+, ω^- and global softness (δ) calculated from FMO energies using the formulas based on Koopmans theorem [131-133].

$$\text{Electronegativity } (\chi) = -\tfrac{1}{2}\,(E_{Homo} + E_{Lumo})$$

$$\text{Global hardness } (\eta) = -\ \tfrac{1}{2}\,(E_{Homo} - E_{Lumo})$$

$$\text{Chemical potential } (\mu) = \tfrac{1}{2}\,(E_{Homo} + E_{Lumo})$$

$$\text{Global softness } (\delta) = 1/\eta$$

$$\text{Electrophilicity } (\omega) = \chi^2 /2\eta$$

$$\text{Electron donating capability } (\omega^-) = (3E_{Homo} + E_{Lumo})^2 / 16\ (E_{Homo} - E_{Lumo})$$

$$\text{Electron accepting capability } (\omega^+) = (E_{Homo} + 3E_{Lumo})^2 / 16\ (E_{Homo} - E_{Lumo})$$

Calculated values of these descriptors are presented in Table 18. On perusal of these values, it could be concluded that complex **5** is more reactive and polarisable than **6**. The spin density plot of complex **7** is shown in Fig. 72.

Table 18 Global reactivity parameters for complexes **5-7**.

Molecular descriptors	Mathematical description	5	6	7
E_{HOMO}	Energy of HOMO	-3.5763	-3.5496	-2.0149
E_{LUMO}	Energy of LUMO	-5.7161	-5.0982	-4.2653
Energy gap	$\Delta E_g = E_{HOMO} - E_{LUMO}$	2.1398	1.5486	2.2504
Ionization potential (IP)	$IP = - E_{HOMO}$	3.5763	3.5496	2.0149
Electron Affinity (EA)	$EA = - E_{LUMO}$	5.7161	5.0982	4.2653
Electronegativity (χ)	$(\chi) = -\frac{1}{2}(E_{HOMO} + E_{LUMO})$	4.6462	4.3239	3.1401
Chemical potential (μ)	$(\mu) = \frac{1}{2}(E_{HOMO} + E_{LUMO})$	-4.6462	-4.3239	-3.1401
Global Hardness (η)	$(\eta) = -\frac{1}{2}(E_{HOMO} - E_{LUMO})$	1.0699	0.7743	1.1252
Softness (S)	$(S) = \frac{1}{2\eta}$	0.4673	0.6457	0.4443
Electrophilicity index (ω)	$(\omega) = \frac{\mu^2}{2\eta}$	10.0884	12.0729	4.3815
Electron donating capability (ω^-)	$(\omega^-) = (3E_{Homo}+E_{Lumo})^2 / 16\ (E_{Homo}-E_{Lumo})$	7.8990	10.0077	2.9510
Electron accepting capability (ω^+)	$(\omega^+) = (E_{Homo}+3E_{Lumo})^2 / 16\ (E_{Homo}-E_{Lumo})$	12.5476	14.3316	3.2118

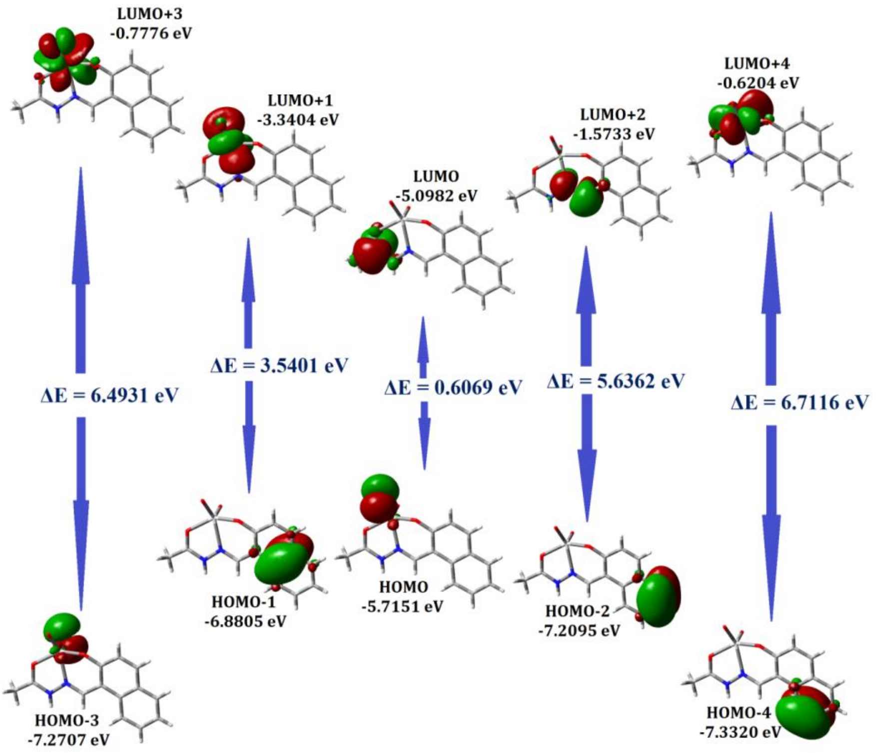

Fig. 69. HOMO-LUMO energy diagrams of complex **5**.

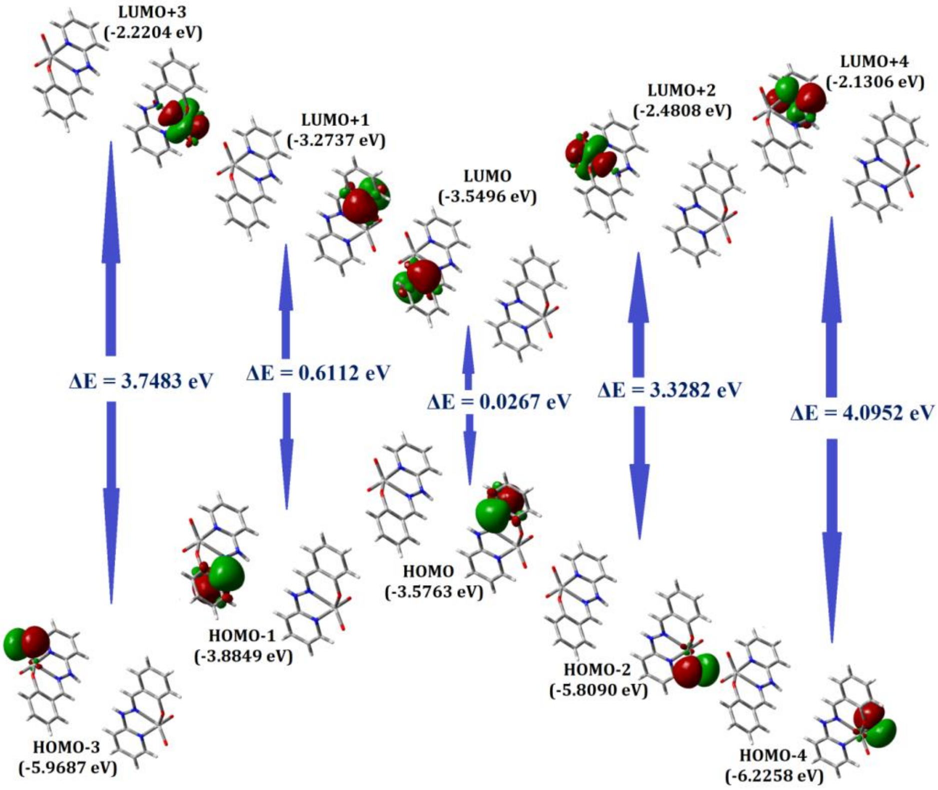

Fig. 70. HOMO-LUMO energy diagrams of complex **6**.

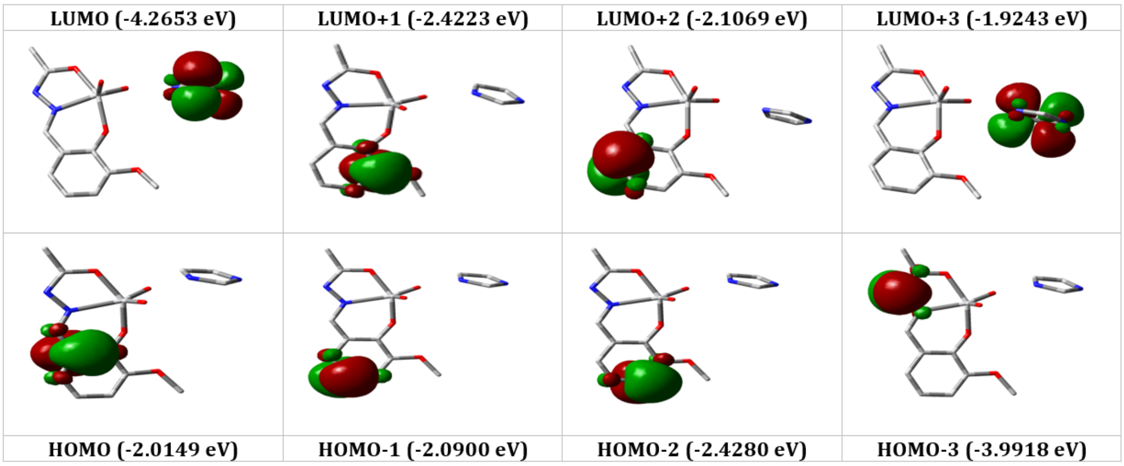

Fig. 71. HOMO-LUMO energy diagrams of complex **7**.

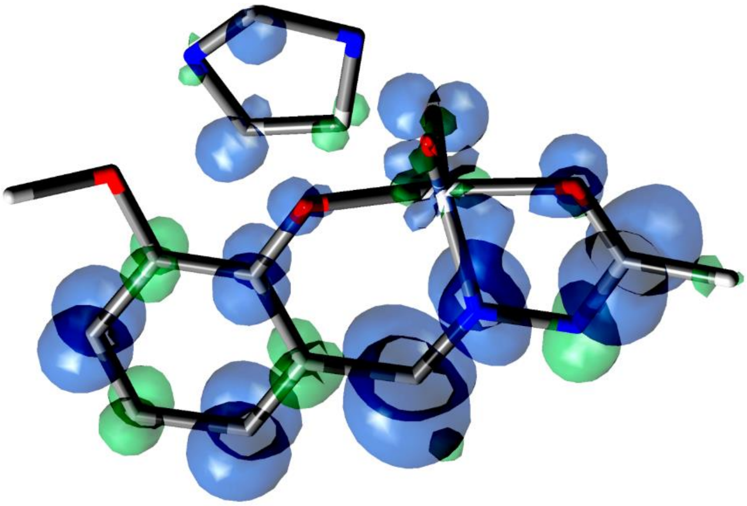

Fig. 72. Spin density plot of complex **7**.

3.16 Molecular Docking

For complex **1** of protein receptor with vanadium derivative, the binding energy observed was -4.940 Kcal/mol and ligand was observed to form five favourable interactions with alpha glucosidase. The anisole ring of the compound indicated Pi-alkyl interaction with Ile146, while the methyl group indicated Hydrogen bond Gly228. Side chains of Glu271, Arg400 and Asp333 of the protein were involved in the hydrogen bonds with the “vanadiumoylol” group. Also, the amino group of the Asp202 was involved in the hydrogen bond with the hydrazinyl group of the compound (Fig. 73).

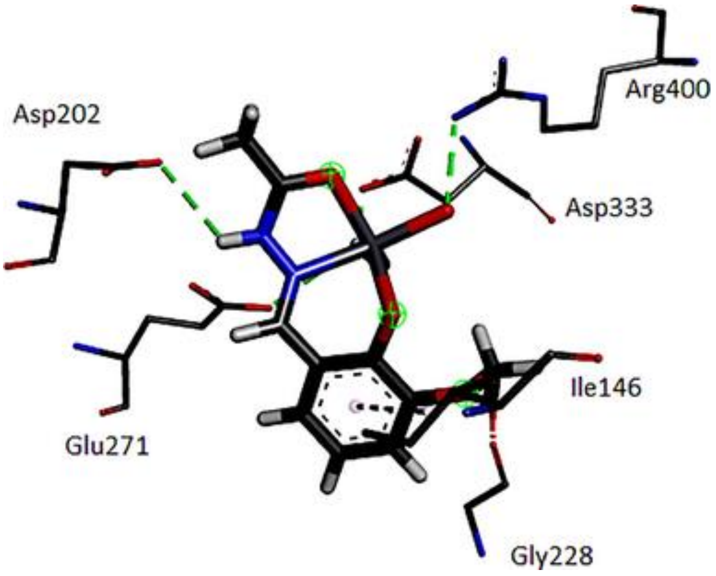

Fig. 73. The image indicates the interactions of the vanadium derivative -**1** with the receptor protein.

For complex **2** of protein receptor with vanadium derivative-2,the binding energy observed was -4.612Kcal/mol and ligand was observed to form six favourable interactions with the receptor. The Bromo-anisole ring of the compound indicated Pi-Pi interaction with the aromatic ring of Phe147 and Pi-anion interaction with the side chain of Glu271. Notably, the bromine group indicated Pi-alkyl interaction with the aromatic ring of Tyr65. Sidechains of Asp333 of the protein were involved in the hydrazinyl group of the compound. Also, the Phe297 indicated Pi-Pi interaction and Leu227 indicated hydrogen bond with the pyridinyl group of compounds (Fig. 74).

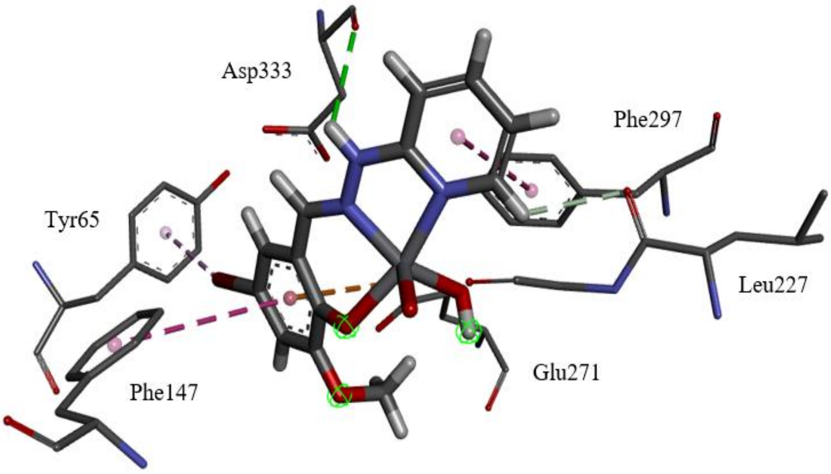

Fig. 74. The image indicates the interactions of the vanadium derivative-**2** with the receptor.

For complex **3** of protein receptor with vanadium derivative-3 the binding energy observed was -4.91Kcal/mol and ligand was observed to form seven favourable interactions with the receptor. The Bromo-benzyl ring of the compound indicated alkyl interaction with Lys225. Hydrazinyl group forms a Hydrogen bond with Leu227 and pyridinyl group forms Pi-alkyl interactions with Pro230 and Val334. Also, the imidazole groups attached to the vanadium were observed to form Pi-alkyl interactions with the backbone of Met302 and side chain of Val335 and Pi-Pi T shaped interaction with the aromatic ring of Phe397 (Fig.75).

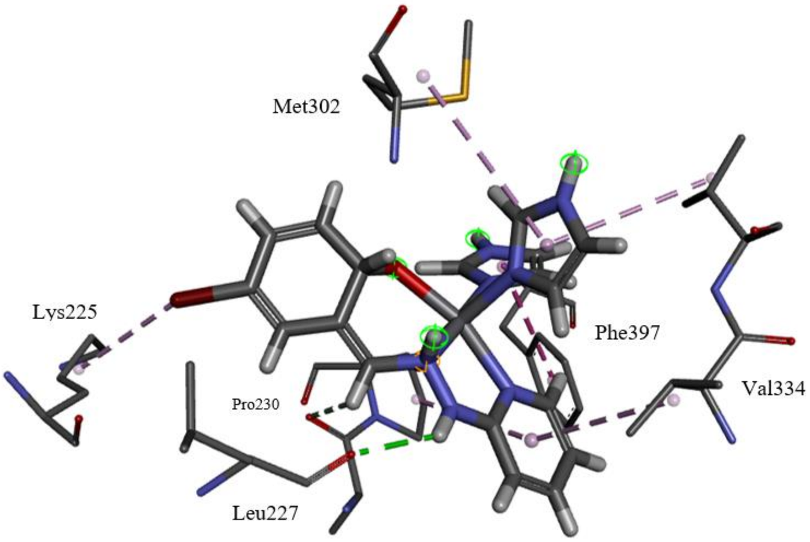

Fig. 75. The image indicates the interactions of the vanadium derivative-**3** with the receptor.

For complex **4** of protein receptor with vanadium derivative-4, the binding energy observed was -4.41Kcal/mol and ligand was observed to form four favourable interactions with the receptor. The anisole ring of the compound indicated Pi-alkyl interactions interaction with the side chain of Asp202 and Asp333. The imidazole groups attached to the vanadium were observed to form Pi-cation interaction with the guanidine group of the Arg400 (Fig. 76).

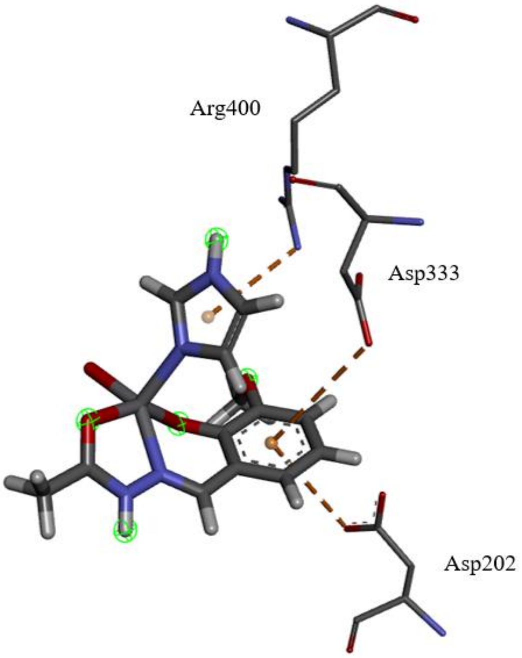

Fig. 76. The image indicates the interactions of the vanadium derivative-**4** with the receptor.

3.17 Antidiabetic activity

3.17.1 α-Glucosidase inhibition activity

The activity of HL^1, HL^2, complexes **1-4** were carried out, against alpha glucosidase and inhibition graph is shown in Fig. 77. We found lowest IC_{50} value for **1** while highest IC_{50} were found in HL^2 and moderately in **2, 3** and **4**. The IC_{50} values for α-glucosidase inhibition activity were ranged from 4-400 µg/mL.**2** observed most potent among all the complexes with IC_{50} value 4 µg/mL while HL^2 was cheapest inhibitor with IC_{50} value 432 µg/mL (Table 19). Therefore, it can be concluded that the complexes gave remarkable alpha glucosidase inhibition and showed concentration dependent activities. This study predicts the dose-dependent α-glucosidase inhibition caused by the present oxidovanadium complexes. The inhibition activity was found to increase as the concentration of complexes increased in the tested ligands and complexes. In previous studies, similar results were observed [134, 135].

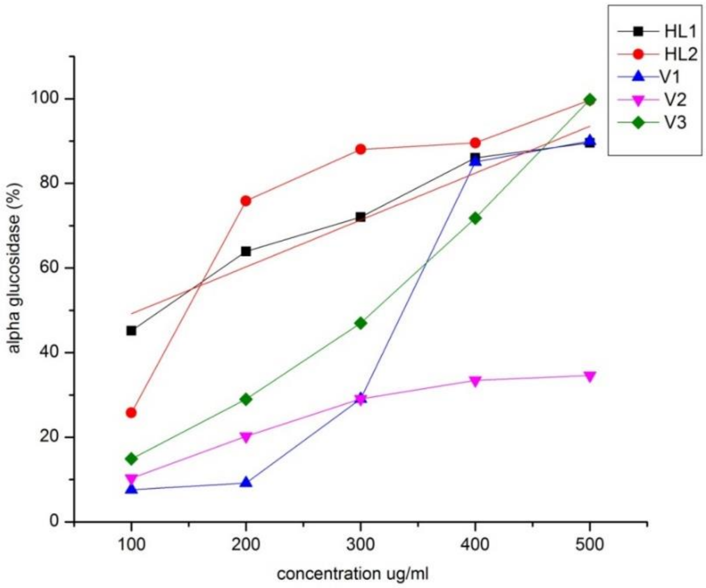

Fig. 77. α-Glucosidase inhibition graph of compounds.

Table 19 Concentration, % inhibition and IC$_{50}$ value of compounds.

Concentration	**HL^{1}**	**HL^{2}**	**1**	**2**	**3**	**4**
ug/mL	%inhibition	%inhibition	%inhibition	%inhibition	%inhibition	%inhibition
100	32.63076	27.94692	30.99141	30.99141	22.79469	12.95863
200	47.61905	34.34817	46.52615	46.52615	32.16237	21.7018
300	55.58158	47.77518	50.89774	50.89774	49.96097	39.65652
400	65.57377	51.44418	60.26542	60.26542	75.56596	63.85636
500	73.69243	66.66667	62.52927	62.52927	89.30523	93.52069
600	89.85168	74.23888	78.06401	72.6776	72.6776	96.87744
IC$_{50}$ (μg/mL)	9.15	434.9935	4.16	394.3758	394.3758	411.24

3.17.2 α-Amylase inhibition activity

In the present study activity of HL^{1}, HL^{2}, complexes **1-3** were carried out against alpha amylase and the inhibition graph is shown in Fig. 78. Lowest IC$_{50}$ value observed in **1** while the highest IC$_{50}$ were found in HL^{2}, **2** and **3** showing moderate inhibition against αAmylase at different concentration (Table 20). It can be concluded that these complexes are potent α-amylase inhibitors. Therefore, all compounds gave remarkable alpha amylase inhibition and showed concentration-dependent activities.

We evaluated the in vitro α-amylase inhibition activity of ligands and vanadium complexes, results compared with acarbose and expressed in terms of IC_{50} value and percentage of inhibition as in literature [136]. All complexes showed concentration-dependent activity, on increasing the concentration of test samples more Inhibition of α-amylase enzyme seen. The IC_{50} values for α-amylase inhibition activity were ranged from 122-700 µg/mL. The **1** seen the most potent among all the complexes with an IC_{50} value of 122.28 µg/mL while **2** was a weak inhibitor with an IC_{50} value of 793 µg/mL.

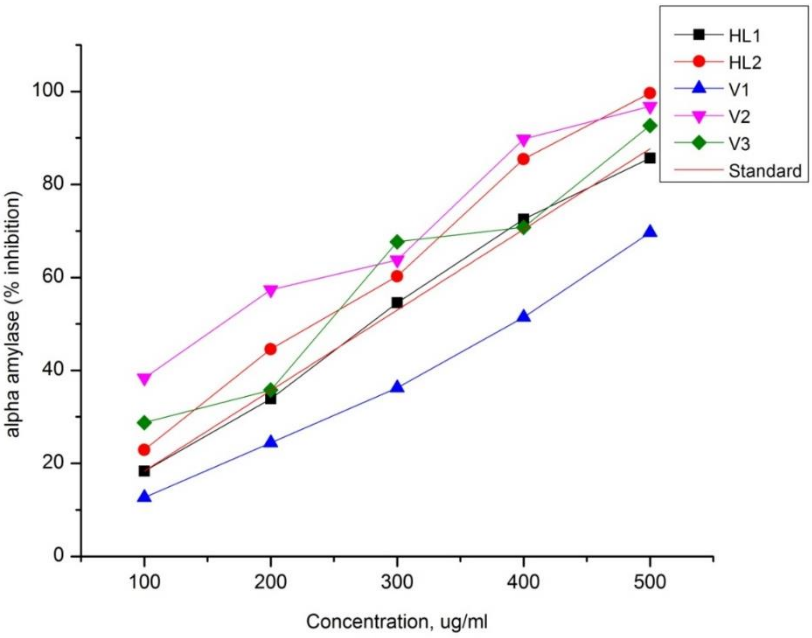

Fig. 78. α-Amylase inhibition graph of compounds.

Table 20 Concentration, % inhibition and IC_{50} value of compounds.

Concentration	**HL^1**	**HL^2**	**1**	**2**	**3**
µg/mL	%inhibition	%inhibition	%inhibition	%inhibition	%inhibition
100	18.35	22.93	12.67	38.35	28.76
200	33.87	44.56	24.45	57.35	35.76
300	54.58	60.27	36.23	63.76	67.68
400	72.57	85.45	51.45	89.77	70.78
500	85.67	99.63	69.65	96.78	92.67
IC_{50}	357.32	736.54	122.28	793.25	336.51

3.17.3 α-Glucosidase inhibition activity

The α-glucosidase activity of HL^3, HL^4, **5**, **6** and **7** were also measured against α-glucosidase. The percentage inhibition plots of these compounds are shown in Fig. 79. And IC_{50} and α-glucosidase activity are collected in Table 21. It is observed that the IC_{50} values of complexes are lower in comparison to the corresponding free ligands (Table 21). Suggesting these vanadium complexes exerted stronger inhibition than free ligands. In the same table calculated α-glucosidase activity also given. The α-glucosidase activity of all complexes is higher than the free ligands. The findings proved that these complexes are potent inhibition against α-glucosidase. The major macronutrients in biological systems are carbohydrates, fats and proteins. Monosaccharides glucose can easily be observed into the bloodstream from the gastrointestinal tract. α-glucosidase can convert most of the carbohydrates (polysaccharides and starch) molecules into absorbable Monosaccharides (glucose and fructose). So that, diabetes and obesity could be controlled by inhibiting enzyme activity of α-glucosidase to delay the absorption of carbohydrates from diet. The present complexes showed good α-glucosidase activity. Similar in result *in vitro* α-glucosidase activity were reported [34-36]. Moreover, it can be found that these complexes had higher inhibitory activity than corresponding free ligands and complexes might be useful for lowering the glucose level.

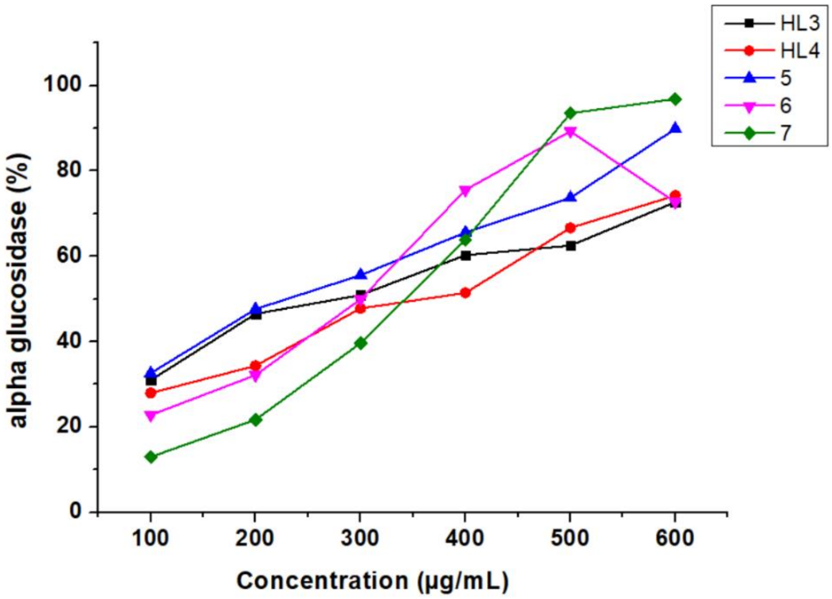

Fig. 79. α-Glucosidase inhibition graph of complexes **5-7**.

Table 21 α-Glucosidase inhibitory activity data of ligand and complexes **5-7**.

Complex	IC_{50} (μg/mL)	Antidiabetic activity (μg^{-1})
HL^3	289.49	3.454
HL^4	374.63	2.669
5	228.68	4.373
6	300.66	3.32
7	343.79	2.909

3.17.4 α-Amylase inhibition activity

The α-amylase inhibitory data of ligands activity HL^3 and HL^4 and their complexes (**5-7**) with vanadium were performed by the reported method [70]. The inhibitory plots of present compounds are shown in Fig. 80. From these plots, IC_{50} values were evaluated and collected in Table 22. In the same table α-amylase inhibitory is also indicated for each ligand and complexes. It can be seen from the Table 22 that complexes showed better inhibitory activity in comparison used ligands. α-amylase performs a major role in the useful in reducing postprandial hyperglycaemia and then controlling diabetes or obesity. The α-amylase activity inhibitory data of ligand and complexes showed a significant inhibitory effect on α-amylase. Moreover, it in observed that complexes had higher inhibitory activity in comparison to free ligand.

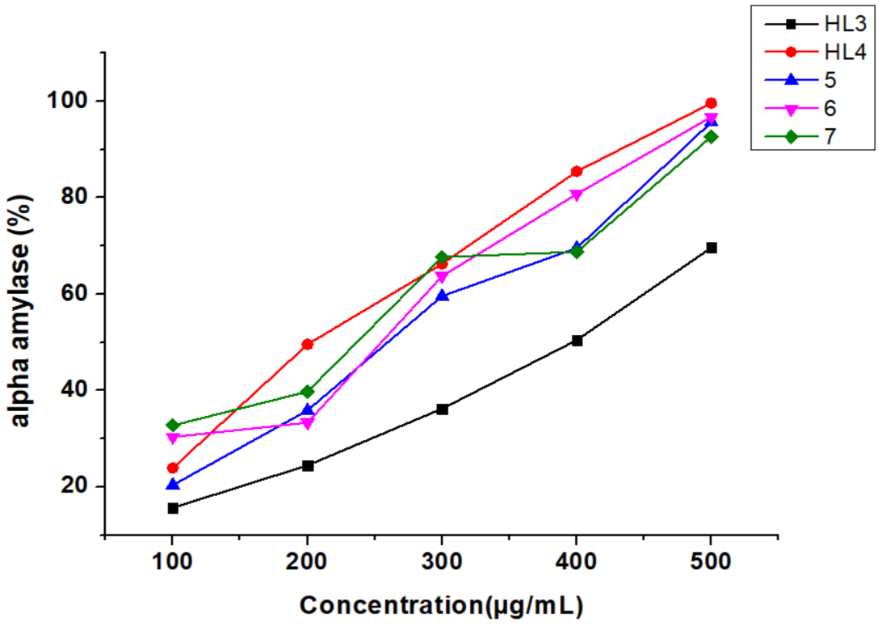

Fig. 80. α-Amylase inhibition graph of compounds **5-7**.

Table 22 α-Amylase inhibitory activity data of ligand and complexes **5-7**.

Complex	IC_{50} (μg/mL)	Antidiabetic activity (μg^{-1})
HL^3	397.75	2.514
HL^4	199.63	5.010
5	261.28	3.827
6	257.31	3.880
7	238.61	4.190

4 Conclusions

In this work, we have synthesized HL^1, HL^2, HL^3 and HL^4 hydrazide ligand and characterized by FTIR, ^1H and ^{13}C NMR. a series of vanadium (IV/V) complexes **1**-7 of tridentate Schiff bases were synthesized and characterized by various physicochemical methods such as elemental analysis, FTIR, UV-Vis, CV and EPR techniques. The structures determined on ligand HL^2, complex 3,5,6 and 7 by single-crystal X-ray diffraction. The geometry of five coordinated complexes (**1**, **2**, **4**, **5**, **6** and **7**) can be described in terms of trigonal bipyramidal or square pyramidal. The room temperature magnetic measurements of complex **1**, **2** and **4** are in the range of 1.79 to 1.83 B.M. The molecular structure of complex **3** shows that the central metal ion has an N_4O_2-donor environment and has octahedral geometry. *In-vitro* α-glucosidase inhibition activity and α-amylase inhibition activity results proved that these complexes are promising anti-diabetic agents.

References

1 F. Zechel, P. Schwendt, R. Gyepes, J. Simunek, J. Tatiersky, L.K. Rivosudsy, New J.Chem. 43(2019) 17696-17702.
2 S. Parihar, R.N. Jadeja, V.K. Gupta, RSC Adv. 4 (2014) 10295-10302.
3 R.N. Patel, Y.P. Singh, J. Mol. Struct. 1153 (2014) 162-169.
4 D. Sanna, J. Palomba, G. Lubinu, P. Buglyo, S. Nagy, F.Perdih, E. Garribba, J. Med. Chem. 62 (2019) 654-664.
5 S. Kundu, S. Maity, A.N. Maity, S.C. Ke, P. Ghosh, Dalton Trans. 42 (2013) 4586-4601.
6 K.H. Thamson, C. Orvig, J. Inorg. Biochem. 100 (2006) 1925-1935.
7 W. Basuki, M. Hiromura, Y. Adachi, K. Tayama, M. Hattori, H. Sakurai, Biochem. Biophys. Res. Commun. 349 (2006) 1163-1170.
8 K.D. Mjos, C. Orvig, Chem. Rev. 114 (2014) 4540-4563.
9 D. Rehder, Future Med. Chem. 4 (2012) 1823-1837.
10 C.E. Heyliger, A.G. Tahiliani, J.H. McNeill, Science 227 (1985) 1474-1477.

11 K.H. Thompson, C. Orvig, J. Inorg. Biochem. 100 (2006) 1925-1935.
12 R. Yanardag,T.B. Demirci, B. Ulkuseven, S. Bolkent, S. Tunali, S. Bolkent, Eur. J. Med. Chem. 44 (2009) 818-826.
13 J.C. Craig, D. Wills, S.D. Rubbo, J. Edgar, Nature 176 (1955) 34-35.
14 K.H. Thomson, J.H. McNeill, C. Orvig, Chem. Rev. 99 (1999) 2885-2891.
15 R. Yanardag, T.B. Demirci, B. Ulkuseven, S. Bolkent, S. Tunali, S. Bolkent, Eur. J. Inorg. Chem. 44 (2009) 818-826.
16 Y. Adachi, J. Yoshida, Y. Kodera, A. Katoh, J. Takada, H. Sakurai, J. Med. Chem. 49 (2006) 3251-3256.
17 J.C. Craig, D Willis, S.D. Rubbo, J. Edgar, Nature 176 (1955) 34-35.
18 K.H. Thamson, J.H. McNill, C. Orvig, Chem. Rev. 99 (1999) 2561–2571.
19 M. Enamullah, A.K.M.R. Uddin, G. Pescitelli, R. Berardozzi, G. Makhloufi, V. Vasylyeva, A.C. Chamayoud, C. Janiak, Dalton Trans. 43 (2014) 3313-3329.
20 M. Enamullah, V. Vasylyeva, C. Janiak, Inorg. Chim. Acta 408 (2013) 109-119.
21 K. Pyta, A. Janas, M. Szukowska, P. Pecyna, M. Jaworska, M. Gajecka, F. Bartl, P. Przybylski, Eur. J. Med. Chem. 167 (2019) 96-104.
22 R. Sreenivasulu, K.T. Reddy, P. Sujitha, C.G. Kumar, R. Raju, Biorg. Med. Chem. 27 (2019) 1043-1055.
23 U. Ghani, Biorg. Chem. 83 (2019) 235-241.
24 K.C. Gupta, A.K. Sutar, Coord. Chem. Rev. 252 (2008) 1420-1450.
25 M. Rezaeivala, H. Keypour, Coord. Chem. Rev. 280 (2014) 203-253.
26 D.C Crans, J.J Smee, E. Gaidamauskas, L. Yang, Chem. Rev. 104 (2004) 849-902.
27 J.C. Pessoa, E. Garribba, M.F.A. Santos, T.S.S. Pessoa, Coord. Chem. Rev. 301-302 (2015) 49-86.
28 D. Rehder, Inorg. Chem. Acta 455 (2017) 378-389.
29 E. Tsuchida, K. Oyaizu, Coord. Chem. Rev. 237 (2003) 213.
30 S. Dey, S.P. Rath, Dalton Trans. 43(2014) 2301–2314.
31 M.J. Clague, N.L. Keder, A. Butler, Inorg. Chem. 32 (1993) 4754-4761.
32 R.N. Patel, Y.P. Singh, Y. Singh, R.J. Butcher, J.P. Jasinski, Polyhedron 129 (2017) 164-181.
33 R.N. Patel, Y.P. Singh, Y. Singh, R.J. Butcher, M. Zeller, R.K. Bhubon Singh, U. Oinam, J. Mol. Struct. 1136 (2017) 157-172.
34 N. Patel, A.K. Prajapati, R.N. Jadeja, I.P. Tripathi, N. Dwivedi, J. Coord. Chem. 73 (2020) 1131-1146.
35 N. Patel, A.K. Prajapati, R.N. Jadeja, R.N. Patel, S.K. Patel, V.K. Gupta, I.P. Tripathi, N. Dwivedi, Inorg. Chim. Acta, 493 (2019) 20-29.
36 N. Patel, A.K. Prajapati, R.N. Jadeja, R.N. Patel, S.K. Patel, I.P. Tripathi, N. Dwivedi, V.K. Gupta, R.J. Butcher, Polyhedron 180 (2020) 114434.
37 Bruker, SMART (Version 5.631), SAINT (Version 6.45) and SADABS (Version 2.05), Bruker AXS Inc., Madison, Wisconsin, USA, (2003).
38 G. M. Sheldrick, SHELXS97 and SHELXL97, University of Gottingen, Germany, 1997.
39 A.L. Spek, PLATON for Windows. September 1999 Version, University of Utrecht, Netherlands, (1999).
40 M. Nardelli, J. Appl. Crystallogr. 28 (1995) 659.
41 P. Buglyo, D.C. Crans, E.M. Nagy, R.L. Lindo, L. Yang, J.J. Smee, W. Jin, L.–H. Chi, M.E. Godzala, G.R. Willsky, Inorg. Chem. 44 (2005) 5416–5427.
42 S. Kundu, S. Maity, T. Weyhermülle, P. Ghosh, Inorg. Chem. 52 (2013) 7417-7430.

43 A. Sarkar, S. Pal, Polyhedron 26 (2007) 1205–1210.
44 J.J. Koenderink, A.J.V. Doorn, Image Vision Comput. 10 (1992) 557-564.
45 M.J. Frisch, G.W. Trucks, H.B. Schlegel, G.E. Scuseria, M.A. Robb, J.R. Cheeseman, G. Scalmani, V. Barone, B. Mennucci, G.A. Petersson, H. Nakatsuji, M. Caricato, X. Li, H.P. Hratchian, A.F. Izmaylov, J. Bloino, G. Zheng, J.L. Sonnenberg, M. Hada, M. Ehara, K. Toyota, R. Fukuda, J. Hasegawa, M. Ishida, T. Nakajima, Y. Honda, O. Kitao, H. Nakai, T. Vreven, J.A. Montgomery Jr., J.E. Peralta, F. Ogliaro, M. Bearpark, J.J. Heyd, E. Brothers, K.N. Kudin, V.N. Staroverov, T. Keith, R. Kobayashi, J. Normand, K. Raghavachari, A. Rendell, J.C. Burant, S.S. Iyengar, J. Tomasi, M. Cossi, N. Rega, J.M. Millam, M. Klene, J.E. Knox, J.B. Cross, V. Bakken, C. Adamo, J. Jaramillo, R. Gomperts, R.E. Stratmann, O. Yazyev, A.J. Austin, R. Cammi, C. Pomelli, J.W. Ochterski, R.L. Martin, K. Morokuma, V.G. Zakrzewski, G.A. Voth, P. Salvador, J.J. Dannenberg, S. Dapprich, A.D. Daniels, O. Farkas, J.B. Foresman, J.V. Ortiz, J. Cioslowski, D.J. Fox, Gaussian 09, Revision D.01, Gaussian, Inc., Wallingford, CT, 2013.
46 P.J. Hay, W.R. Wadt, J. Chem. Phys. 82 (1985) 299-310.
47 P.J. Hay, W.R. Wadt, J. Chem. Phys. 82 (1985) 284-298.
48 P.J. Hay, W.R. Wadt, J. Chem. Phys. 82 (1985) 270-283.
49 Gauss View 5.0.9 (Gaussian Inc., Wallingford, CT, USA) (2009).
50 A.E. Reed, R.B. Weinstock, F. Weinhold, J. Phys. Chem. 83 (1985) 735–746.
51 (a) R. Bauernschmitt, R. Ahlrichs, Chem. Phys. Lett. 256 (1996) 454–464; (b) R.E. Stratmann, G.E. Scuseria, M.J. Frisch, J. Chem. Phys. 109 (1998) 8218–8224; (c) M.E. Casida, C. Jamorski, K.C. Casida, D.R. Salahub, J. Chem. Phys. 108 (1998) 4439–4449.
52 (a) V. Barone, M. Cossi, J. Phys. Chem. 102 (1998) 1995–2001; (b) M. Cossi, V. Barone, J. Chem. Phys. 115 (2001) 4708–4717.
53 M.A. Spackman, J.J. McKinnon, Cryst. Eng. Comm. 4 (2002) 378-392.
54 M.A. Spackman, P.G. Byrom, Chem. Phy. Lett. 267 (1997) 309.
55 J.J. McKinnon, A.S. Mitchell, M.A. Spackman, J. Eur. Chem. 4 (1998) 2136-2141.
56 J.J. McKinnon, M.A. Spackman, A.S. Mitchell, Acta Crystallogr. Sec. B 60 (2004) 627-668.
57 A.L. Rohl, M. Moret, W. Kaminsky, K. Claborn, J.J. McKinnon, B. Kahr, Cryst. Growth Des. 8 (2008) 4517-4525.
58 A. Parkin, G. Barr, W. Dong, C.J. Gilmore, D. Jayatilaka, J.J. McKinnon, M.A. Spackman, C.C. Wilson, Cryst. Eng. Comm. 9 (2007) 648-652.
59 S.K. Wolff, D.J. Greenwood, J.J. McKinnon, D. Jayatilaka, M.A. Spackman, Crystal Explorer 2.0; University of Western Australia: Perth, Australia, (2007).
60 J.J. Koenderink, A.J.V. Doorn, Image Vision Comput.10 (1992) 557-564.
61 X. Shen, W. Saburi, Z. Gai, K. Kato, T.O. -Kato, J. Yu, K. Komoda, Y. Kido, H. Matsui, H. Mori and M. Yao, Acta Crystallogr. D BiolCrystallogr. 71 (2015) 1382-1391.
62 H.M. Berman, J. Westbrook, Z. Feng, G. Gilliland, T.N. Bhat, H. Weissig, I.N. Shindyalov, P.E. Bourne, Nucleic Acids Res. 28 (2000) 235–242.
63 C.P. MarvinSketch, M. View, In Proceedings of ECSOC-3, the third international electronic conference on synthetic organic chemistry, (1999) 367-369.
64 G.M. Morris, R. Huey, W. Lindstrom, M.F. Sanner, R.K. Belew, D.S. Goodsell, A.J. Olson, J. Comput. Chem. 16 (2009) 2785-2791.
65 R.K. Modukuri, D. Choudhary, S. Gupta, K.B. Rao, S. Adhikary, T. Sharma, M.I.

Siddiqi, R. Trivedi, K.V. Sashidhara, Bioorg. Med. Chem. 24 (2017) 6450-6466.

66 S. Maheshwari, S.R. Avula, A. Singh, L.R. Singh, G.R. Palnati, R.K. Arya, S.H. Cheruvu, S. Shahi, T. Sharma, S. Meena, A.K. Singh, R. Kant, M. Riyazuddin, H.K. Bora, M.I. Siddiqi, J.R. Gayen, K.V. Sashidhara, D. Datta, Mol. Cancer Ther. 9 (2017) 1791-1805.

67 P. Vishwakarma, N. Parmar, P. Chandrakar, T. Sharma, M. Kathuria, P.K. Agnihotri, M.I. Siddiqi, K. Mitra, S. Kar, Cell Mol. Life Sci. 3 (2018) 563-588.

68 I.P. Tripathi, A. Kamal, M.K. Mishra, A. Dwivedi, R. Tripathi, C. Mishra and L. Shastri, Ind. J. Appl. Res. 4 (2014) 66-69.

69 D. Gomathi, M. Kalaiselvi, C. Uma, Int. Res. J. Pharmacy. 3 (2012) 226-229.

70 E. Apostolidis, Y.I.I. Kwon, K. Shetty, Asia Pac. J. Clin. Nutr. 15 (2006) 433–441.

71 C. Polonyi, A. Alshiekh, L.A. Sarsam, M. Clausen, S.K.C. Elmroth, Dalton Trans. 43 (2013) 11941-11949.

72 G.J. Colpas, B.J. Hamstra, J.W. Kampf and V.L. Pecoraro, J. Am. Chem. Soc. 118 (1996) 3469-3478.

73 G.J. Colpas, B.J. Hamstra, J.W. Kampf, V.L. Pecoraro, J. Am. Chem. Soc. 116 (1994) 3627-3628.

74 K. Nakamoto, Infrared and Raman spectra of 5th Ed., John Wiley and Sons, Ins. New York, (1997)

75 C. Das, P. Adak, S. Mondal, R. Sekiya, R. Kuroda, S.I. Gorelsky, S.K. Chattopadhyay,Inorg. Chem. 53 (2014) 11426-11437.

76 K. Nakamoto, Inorganic and Coordination Compounds, second ed., Wiley Interscience, New York, (1970).

77 R.L. Beddoes, D. Collison, F.E. Mabbs, M.A. Passand, Polyhedron. 9 (1990) 2483-2489.

78 M.J. Clague, N.L. Keder, A. Butler,Inorg. Chem. 32 (1993) 4754-4761.

79 C.J. Carrano, M. Mohan, S.M. Holmes, R. Rosa, A. Butler, J.M. Charnock, C.D. Garner,Inorg. Chem. 33 (1994) 646-655.

80 K.M. Perry, J.J. Onuffer, M.S. Gittelman, L. Barmat, C.R. Matthews,Biochem. 28 (1989) 7961-7968.

81 A. Sarkar, S. Pal, Polyhedron 26 (2017) 1205-1210.

82 G. Asgedom, A. Sreedhara, J. Kivikoski, E. Kolehmainen, C.P. Rao, J. Chem. Soc.,Dalton Trans.(1996) 93-97.

83 G. Romanowski, M. Wera, Polyhedron 13 (2010) 2747-2754.

84 S. Samanta, D. Ghosh, S. Mukhopadhyay, A. Endo, T.J.R. Weakley, M. Chaudhury, Inorg. Chem. 42(2003) 1508–1517.

85 I. Syiemlieh, M. Asthana, S.D. Kurbah, R.A. Lal, Polyhedron 170 (2019) 202-216.

86 F. Fredoueil, M. Evain, D. Massiot, M.B. -Doeuff, P. Janvier, A. Clearfield, B. Bujoli, J. Chem. Soc., Dalton Trans. (2002) 1508-1512.

87 A.G. Orpen, L. Brammer, F.H. Allen, O. Kennard, D.G. Watson, R. Taylor, J. Chem. Soc., Dalton Trans. 91 (1989) S1-S83.

88 C. Wiedemann, W. Priebsch, D. Rehder, Chem. Ber, 122 (1989) 235.

89 M. Baldini, M.B. -Ferrari, F. Bisceglie, G. Pelosi, S. Pinelli, P. Tarasconi,Inorg. Chem. 42 (2003) 2049-2055.

90 M.X. Li, L.Z. Zhang, C.L. Chen, J.Y. Niu, B.S. Ji, J. Inorg. Biochem. 106 (2012) 117-125.

91 K. Saatchi, K.H. Thompson, B.O. Patrick, M. Pink, V.G. Yuen, J.H.M. Neill, C. Orvig,Inorg. Chem. 44 (2005) 2689-2697.

92 S.–X. Liu, S. Gao, Inorg. Chim. Acta. 282 (1998) 149-154.
93 C.R. Cornman, G.J. Colpas, J.D. Hoeschele, J. Kampf, V. L. Pecoraro, J. Am. Chem. Soc. 114 (1992) 9925-9933.
94 Y-M Jiang, J-H Cai, Z-M Liu, X-H Liu, Acta. Cryst. Soc. E61 (2005) 878-880.
95 W. Chen, S. Gao, S.-X. Lio Acta. Cryst. Soc. C55 (1999) 531-533.
96 J. Bernstein, R.E. Davis, L. Shimon, N.L. Chang, Angew. Chem. Int. Ed. Engl. 34 (1995) 155-1573.
97 M. C. Etter, ACC. Chem. Rev. 23 (1990) 120-126.
98 A.W. Addision, T.N. Rao, J. Reedijk, J.V. Rjin, G.C. Verschoor, J. Chem. Soc. Dalton. Trans. (1984) 1349-1356.
99 M.R. Maurya, Dalton. Trans. 39 (2010) 1345-1360.
100 S.Y. Ebrahimpour, Polyhedron 79 (2014) 138-150.
101 S.Y. Ebrahimpour, Polyhedron 93 (2015) 99-105.
102 S.Y. Ebrahimpour, J. Mol. Struct. 1028 (2012) 148-155.
103 C.-L. Zhang, X.-Y Qui, S.-J. Liu, Acta Chim. Slov. 66 (2019) 719-725.
104 S.E. Kochanek, T.M. Clymer, V.S. Pakkala, S.P. Hebert, K. Reeping, S.M. Firestine, J.D. Evanseck, J. Phys. Chem. B 119 (2015) 1184-1191.
105 F. Zhege, Inorg. Chem. 48 (2009) 10249-10256.
106 L. Imaz, Cryst. Growth. Des 7 (2007) 1753-1761.
107 L.M. Gecial, Cryst. Growth. Des 6 (2006) 969-973.
108 J. Bernstein, R. Davis, L. Shimoni, C.N. -Leh, Angew. Chem. Int. Ed. Engl. 34(1995) 1555-1573.
109 N.D. Chasteen, L.J. Berliner, J. Reuben (Eds.), Biological Magnetic Resonance, Plenum Press New York 3 (1981) 53-119.
110 T.S. Smith, R. Lobrutto, V.L. Pecoraro. Coord. Chem. Rev. 228 (2002) 1-18.
111 T.L. Riechel, L.J. De Hayes, D.T. Sawyer, Inorg. Chem. 15 (1976) 1900-1904.
112 A.A. Isse, A. Cennaro, E. Vianello, Electrochimica Acta, 42 (1997) 2065-2071.
113 K. Bhattachary, S.M.T. Abtab, M.C. Majee, A. Endo, M. Chaudhury, Inorg. Chem. 5315 (2014) 8287–8297.
114 N. Aristov, A. Habekost, World J. Chem. Educ. 3 (2015) 115-119**.**
115 S. Roy, M. Bohme, S.P. Dash, M. Mohanty, A. Buchholz, W. Plass, S. Majumder, S. Kulanthaivel, I. Banerjee, H. Reuter, W. Kaminsky, R. Dinda, Inorg. Chem. 57 (2008) 5767–5781.
116 E. Gungor, H. Kara, E. Colacio, A.J. Mota, Eur. J. Chem. 2014 (2014) 1552-1560.
117 C. Yuan, L. Lu, Y. Wu, Z. Liu, M. Guo,S. Xing, X. Fu, M. Zhu, J. Inorg. Biochem, 104 (2010) 978-986.
118 C. Crodily, D. Agustin, J.C. Daran, R. Poli, Inorg. Chim. Acta 364 (2010) 144-149.
119 P.K. Sasmal, A.K. Patra, M. Nethaji, A.R. Chakravarty, Inorg. Chem. 46 (2007) 11112-11121.
120 J.X. Mu, Z.W. Zhai, M.Y. Yang, Z.H. Sun, H.K. Wu, X.H. Liu, Crystals 6 (2016) 1-9.
121 M. Larif, A. Adad, R. Hmammouchi, A.I. Taghki, A. Soulaymani, A. Eimidaoui, M. Bouachrine, T. Lakhlifi, Arabian J. Chem.10 (2017) 946–955.
122 J. X. Mu, Y.X. Shi, M.Y. Yan, Z.H. Sun, X.H. Liu, B.J. Le, N.B. Sun, Molecules 21(2016) 1-11.
123 P. Govindasamy, S. Gunasekaran, S. Srinivasan, Spectrochim. Acta Part A 130 (2014) 329–336.
124 K.C. Zheng, J.P. Wang, W.L. Peng, Y. Shen, F.C. Yun, Inorg. Chim. Acta 328 (2002) 247–253.

125 P. Geerling, F.D. Proft, W. Langenuker, Chem. Rev. 103 (2003) 1793-1874.

126 R.G. Pearson, Chemical Hardness Applications from molecules to Solids, VCH-Wiley: Weinheim, (1997).

127 R.G. Pearson, W. Yang, Density functional Theory of Atoms and Molecules, Oxford University Press: Oxford, (1989).

128 R.G. Pearson, J. Chem. Soc. 117 (2005) 369-377.

129 R. Parthasarathi, J. Padmanabhan, U. Sarkar, B. Maiti, V. Subramanian, P.K. Chattraj, J. Mol. Des. 2 (2003) 798-813.

130 R. Jawaria, M. Hussain, M. Khalida, M.U. Khan, M.N. Tahir, M.M. Naseer, A.A.C. Braga, Z. Shafiq, Inorg. Chim. Acta 486 (2019) 162-171.

131 T. Koopmans, Physica. 1 (1934) 104-117.

132 S. Alturk, D. Avcı, A. Başoglu, O. Tamer, Y. Atalay, N. Dege, Spectrochim. Acta A 190 (2018) 220-230.

133 W. Yang, R.G. Parr, Proc. N. A. Sci. USA 82 (1985) 6723-6726.

134 M.K. Mishra, R. Tripathi, K.B. Pandeya, I.P. Tripathi, Asian. J. Pharm. Clin. Res. 11 (2018) 218–224.

135 Y. Yoshikawa, R. Hirata, H. Yasui, H. Sakurai, Biochimie 91 (2009) 1339–1341.

136 S. Misra, K.B. Pandeya, A.K. Tiwari, A.Z. Ali, T. Saradamani, S.B. Agawane, K. Madhusudana, Int. J. Nutr. Metab. 4 (2012) 11–18.

Paper Published from this chapter

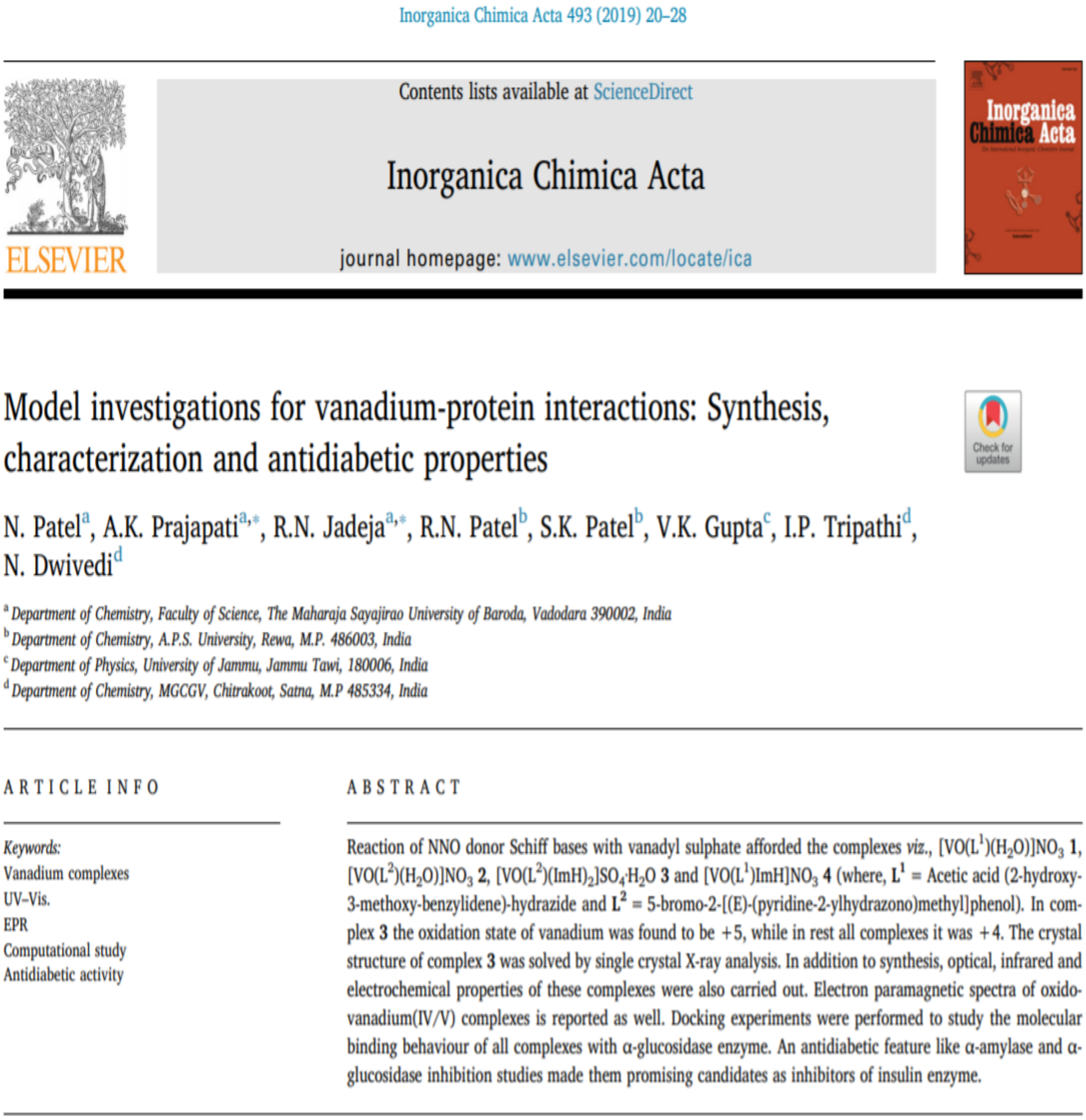

Inorganica Chimica Acta 493 (2019) 20–28

Contents lists available at ScienceDirect

Inorganica Chimica Acta

journal homepage: www.elsevier.com/locate/ica

Model investigations for vanadium-protein interactions: Synthesis, characterization and antidiabetic properties

N. Patel[a], A.K. Prajapati[a,*], R.N. Jadeja[a,*], R.N. Patel[b], S.K. Patel[b], V.K. Gupta[c], I.P. Tripathi[d], N. Dwivedi[d]

[a] Department of Chemistry, Faculty of Science, The Maharaja Sayajirao University of Baroda, Vadodara 390002, India
[b] Department of Chemistry, A.P.S. University, Rewa, M.P. 486003, India
[c] Department of Physics, University of Jammu, Jammu Tawi, 180006, India
[d] Department of Chemistry, MGCGV, Chitrakoot, Satna, M.P 485334, India

ARTICLE INFO

Keywords:
Vanadium complexes
UV–Vis.
EPR
Computational study
Antidiabetic activity

ABSTRACT

Reaction of NNO donor Schiff bases with vanadyl sulphate afforded the complexes *viz.*, $[VO(L^1)(H_2O)]NO_3$ **1**, $[VO(L^2)(H_2O)]NO_3$ **2**, $[VO(L^2)(ImH)_2]SO_4{\cdot}H_2O$ **3** and $[VO(L^1)ImH]NO_3$ **4** (where, $\mathbf{L^1}$ = Acetic acid (2-hydroxy-3-methoxy-benzylidene)-hydrazide and $\mathbf{L^2}$ = 5-bromo-2-[(E)-(pyridine-2-ylhydrazono)methyl]phenol). In complex **3** the oxidation state of vanadium was found to be +5, while in rest all complexes it was +4. The crystal structure of complex **3** was solved by single crystal X-ray analysis. In addition to synthesis, optical, infrared and electrochemical properties of these complexes were also carried out. Electron paramagnetic spectra of oxido-vanadium(IV/V) complexes is reported as well. Docking experiments were performed to study the molecular binding behaviour of all complexes with α-glucosidase enzyme. An antidiabetic feature like α-amylase and α-glucosidase inhibition studies made them promising candidates as inhibitors of insulin enzyme.